PIEZO-ELECTROCHEMICAL TRANSDUCER EFFECT (PECT) INTERCALATED GRAPHITE MICRO-ELECTROMECHANICAL ACTUATORS

DISSERTATION

Glen A. Kading, Major, USAF

AFIT/DEE/ENG/08-03

DEPARTMENT OF THE AIR FORCE
AIR UNIVERSITY

AIR FORCE INSTITUTE OF TECHNOLOGY

Wright-Patterson Air Force Base, Ohio

APPROVED FOR PUBLIC RELEASE; DISTRIBUTION UNLIMITED

The views expressed in this dissertation are those of the author and do not reflect the official policy or position of the United States Air Force, Department of Defense, or the United States Government.

AFIT/DEE/ENG/08-03

PIEZO-ELECTROCHEMICAL TRANSDUCER EFFECT (PECT)
INTERCALATED GRAPHITE MICRO-ELECTROMECHANICAL ACTUATORS

DISSERTATION

Presented to the Faculty

Graduate School of Engineering and Management

Air Force Institute of Technology

Air University

Air Education and Training Command

in Partial Fulfillment of the Requirements for the

Degree of Doctor of Philosophy

Glen A. Kading, B.S.E.E., M.S.E.E.

Major, USAF

November 2007

APPROVED FOR PUBLIC RELEASE; DISTRIBUTION UNLIMITED

iii

AFIT/DEE/ENG/08-03

PIEZO-ELECTROCHEMICAL TRANSDUCER EFFECT (PECT)
INTERCALATED GRAPHITE MICRO-ELECTROMECHANICAL ACTUATORS

DISSERTATION

Glen A. Kading, B.S.E.E., M.S.E.E.
Major, USAF

Approved:

<u>Date</u>
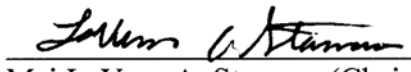
_____   _____
Maj LaVern A. Starman (Chairman)   1 Nov 07
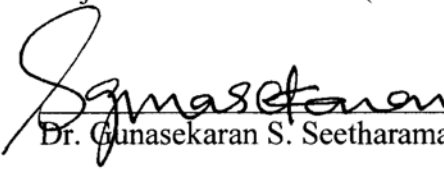
_____   _____
Dr. Gunasekaran S. Seetharaman (Member)   1 Nov 07

_____   _____
Lt Col James A. Fellows (Member)   1 Nov 07
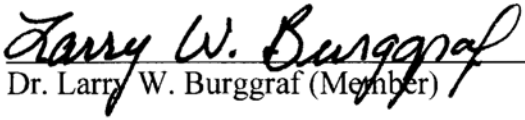
_____   _____
Dr. Larry W. Burggraf (Member)   1 Nov 07
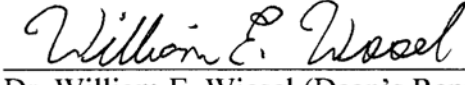
_____   _____
Dr. William E. Wiesel (Dean's Representative)   1 Nov 07

Accepted:

_____   _____
M. U. Thomas   7 Nov 07
Dean, Graduate School of Engineering and Management   Date

iv

Abstract

The purpose of this research is to investigate the Piezo-Electrochemical Transducer (PECT) effect in intercalated graphite as a possible mechanism of actuation for micro-electromechanical systems (MEMS). Specifically, this dissertation will answer three research questions addressing the essential elements of a MEMS actuator: actuation material effectiveness, suitability of use with conventional processing methods, and the feasibility of integrating this actuator into a conventional MEMS system. The research questions will be answered through a literature review of similar actuation materials and operational theory of the PECT effect, analytical analyses, modeling, and through thorough analysis of experimental results.

This dissertation presents the results of research into the PECT effect in H_2SO_4-intercalated graphitized carbon fibers, including both electrical and mechanical characteristics of this effect. This research measures and analyzes data of the first in-plane hybrid PECT actuator consisting of a patterned thin-film highly oriented pyrolytic graphite integrated onto a commercially micromachined physical structure. Strain for PECT devices is later compared to strain generated by current MEMS actuation mechanisms.

PECT fibers achieve up to 1.7% strain in unloaded conditions with 1.4 V of applied potential. In contrast, at this same potential, the piezoelectric material polyvinylidene difluoride (PVDF) generates only 0.01% strain and polysilicon thermal expansion between 0.02 and 0.06% strain depending on the thermal conductivity of the particular polysilicon that the actuators are fabricated in. This work concludes that PECT

carbon fiber actuators achieve two orders of magnitude better strain than PVDF piezoelectric actuators and polysilicon thermal expansion in the same voltage range of operation. In addition to this highly improved strain, the devices, after an initial peak power consumption of 227 µW, a PECT P-100 carbon fiber can hold at an actuation potential while consuming only 260 nW of power continuously. Compare PECT power dissipation to a typical polysilicon thermal actuator, with a maximum of 0.2% strain at 11.5 V of bias, consuming 54.4 mW of power when continuously actuated. PECT actuators at this time are only characterized with H_2SO_4 as an intercalant and can operate only at a maximum theoretical frequency of 80 Hz. This work recommends the encapsulation of a graphite actuator within a conductive polymer for use as a commercial actuator, which will make PECT actuators viable in mainstream MEMS applications. Although slow operation and unpractical intercalants are serious drawbacks to PECT actuators, the characteristics of strain and power consumption presented in this dissertation prove that PECT actuators, given some minor modifications, prove to be a competitive alternative to current MEMS actuators.

Acknowledgements

First and foremost, I would like to express my undying love for my family for standing by me and supporting me during the course of my research. They have been there through the long hours and cranky nights during coursework, and more recently during the writing of this document. To my parents, thank you for believing in me. I want my family to know they mean more to me than anything else in this world.

I would also like to express my sincere appreciation to Major Paul Kladitis, my friend and colleague, for without his help I would have never stumbled into this amazing research field. To my advisor, Major LaVern Starman, you have been a tremendous help and motivator, and I have truly enjoyed the many hours we have spent discussing my research, and the guidance you have given me.

I am indebted to the cleanroom staff, Mr. Rick Patton and Mr. William Trop for all their help during my fabrication foibles, and the AFRL/SN staff for being there when I couldn't get things in the cleanroom to work. To Dr. Benji Maruyama, the insight into this project you gave me has been invaluable, as are all the suggestions and edits on my papers. To Scott Apt, thank you for the FIB, it was a lifesaver, and to Dan Denninghoff, I'm grateful to have you as my friend, thanks for the help, and good luck on your PhD.

Finally, but not least by far, I would like to publicly thank my Father in Heaven for without His support and the talents He has given me I would be nothing.

Glen A. Kading

Table of Contents

List of Figures

xiii

List of Tables

List of Abbreviations

AFRL	Air Force Research Laboratory
BSAC	Berkley Sensors and Actuators Center
CVD	Chemical Vapor Deposition
GIC	Graphite Intercalation Compound
GPIB	General Purpose Interface Bus
H^+	Hydrogen Ion
H_2SO_4	Sulfuric Acid
HCl	Hydrochloric Acid
HOMO	Highest Occupied Molecular Orbital
HOPG	Highly Oriented Pyrolytic Graphite
HSO_4^-	Bisulfate Ion
ITO	Indium-tin Oxide
LED	Light-emitting Diode
LUMO	Lowest Unoccupied Molecular Orbital
MEMS	Micro-electromechanical Systems
ML	Materials and Manufacturing Directorate
PAN	Polyacrilonitrile
PECT	Piezo-Electrochemical Transducer
PolyMUMPs	Polysilicon Mulit-user MEMS Process
PSG	Phosphosilicate Glass
PVC	poly(vinylchloride)
PVD	Physical Vapor Deposition
SN	Sensors Directorate
SWNT	Single-wall Nanotube

PIEZO-ELECTROCHEMICAL TRANSDUCER EFFECT (PECT)

INTERCALATED GRAPHITE MICRO-ELECTROMECHANICAL ACTUATORS

1. Introduction to Actuators

I magine a micro-satellite hurtling through space at the speed of several meters per second. Its mission is to provide critical surveillance information in real-time, while on the "dark side" of the earth. Due to fuel constraints it must maneuver minimally, yet provide the surveillance for as long as possible over the target site, without being in a geosynchronous orbit. Due to size restrictions, micro-electromechanical systems (MEMS) actuators are needed to move the relatively heavy optics, compensating for the angular velocity between the satellite and the target. Since the micro-satellite is on the "dark side" of the earth, its current-limited battery is its only source of power. Although MEMS devices are required for this operation due to size constraints, currently used piezoelectric materials do not provide enough movement for this application, while the alternative polysilicon thermal actuators consume too much power and electrostatic actuators lack the required force. Thus, the project engineers must find an emerging technology to achieve low-power, high strain micro-actuators, and integrate them into the control system for these extreme conditions. Piezo-electrochemical transducer (PECT) devices using intercalated graphite as an actuation mechanism could be that technology.

MEMS devices come in two general categories, thermal or electro-thermal actuators and electrostatic actuators. Each mechanism has its advantages and disadvantages. Electro-thermal actuators are able to achieve up to tens of microns of deflection with 0.2% of generated strain, both parallel to and normal to the substrate

material they are manufactured upon. Unfortunately, the current required to heat these resistive materials is relatively high, 4-5 mA at 7-11.5 V of bias for a typical electro-thermal polysilicon actuator. They provide enough force, tens of μN, to move devices that are hundreds of μm on a side and can be driven to a 10 kHz actuation frequency [1]. Electrostatic actuators are based upon the principle of parallel plate capacitance and electrostatic attraction. If both plates are charged with opposite polarities, they will attract one another. Typically, these devices use large parallel plates to provide a large enough surface area for electrostatic attraction. Electrostatic devices require higher voltages, up to 300 V, than thermal actuators. They also provide lower force given the same amount of area; however, they have nearly zero current drain. In general, electrostatic devices are designed so that the total distance between parallel plates is three times the required travel since the electrodes will "snap" together at 1/3 of the gap.

Knowing these limitations, one can think back to 1974, when one man was the childhood hero of thousands of American youth. He wasn't superman, he was the six-million dollar man. To take a quote from that program "We have the technology. We have the capability to build the world's first bionic man. Steve Austin will be that man. Better than he was before. Better, stronger, faster". Better, stronger, faster: although current semiconductor technology is continuously shrinking the gate size of transistors and is increasing processing speed and power, relatively little has been done since the initial days of MEMS to make these devices "better" as well as faster and stronger. The opportunity now exists to introduce a new MEMS material that will, like the six-million dollar man, make MEMS better, stronger and produce more work per cycle, in effect making MEMS actuators faster.

1.1 An Argument for Graphite MEMS

The United States Air Force has long had an interest in miniaturizing methods of surveillance, reconnaissance, precision navigation, and weaponry. The field of MEMS has furthered that goal, providing a wide range of miniature devices from accelerometers to high-frequency micro-scale switches and arming devices. As the demand placed on MEMS devices increases, the limit of traditional materials begins to limit designs due to required forces and stresses applied to these materials. Traditional polysilicon and nickel-based micro-structures can achieve tens of μN of force and tens of μm of deflection to actuate MEMS devices, but use tens of μW to joule heat electro-thermal actuators. Low-power electrostatic structures can also be used to move MEMS devices, at the expense of low actuation force, high actuation voltages (up to 300 V), and larger design area.

The PECT effect in intercalated graphitic carbon can produce higher forces (hundreds of μN) and strains (up to 2%) than polysilicon electro-thermal actuators while using lower voltage (under 1.4 V) and design area at relatively the same low power of electrostatic actuators. The PECT effect takes advantage of a well established principle of intercalation in graphitic carbon, that is, the induction of strain along one plane within graphitic carbon structures. This research presents the PECT effect as a next-generation mechanism for actuation of MEMS devices.

1.2 The PECT effect

The PECT effect was first discovered by Dr. F. Lincoln Vogel during his tenure at the University of Pennsylvania [2]. In order to understand the PECT effect, and its role in creating a next generation actuator, one must first understand some basic principles

behind the operation. The first of these is the general electrochemical principle which is utilized to produce these high forces and strains in the PECT effect. Second, one must also understand the nature of carbon, and the specific aspects of graphitic carbon, in both highly oriented and carbon fiber form, that allow the PECT effect to be induced and sustained in graphitic carbon. Finally, once the basic concepts of mechanism and material are explained, they will be merged to discuss the specific interactions that occur during the PECT effect in graphitic carbon using a chosen electrolyte.

1.2.1   Intercalation

The PECT leverages the movement of a substance (intercalant) into a host material, a process called intercalation. In this research, the host is graphitic carbon, or graphite for simplicity's sake. Intercalation in graphite can occur spontaneously, or can be driven by a chemical oxidant or by electrolysis of the intercalant, normally leading to a redox process. Redox is shorthand for reduction/oxidation reaction; oxidation is the loss of an electron by a molecule, atom or ion, and reduction is the gain of an electron by a molecule, atom or ion. The intercalant used during intercalation determines whether the effect occurs spontaneously, with a strong oxidizing agent, or through electrolysis.

Although electrolysis and oxidation can both be used to generate intercalation on non-spontaneous systems, the electrochemical approach is most attractive for practical applications and fundamental studies. The electrochemical approach to intercalation provides more information, requires no external oxidants, and offers the possibility to fine-tune the synthesis conditions within the intercalation reaction. As such, it is most advantageous to use an intercalant that can be intercalated electrochemically into the host graphite [3], such as H_2SO_4, to create easily controllable actuators. Redox occurs, and

can be controlled, during the electrochemical formation of H_2SO_4-graphite intercalation compounds.

1.2.2 Carbon

To understand intercalation, one must first understand carbon, and specifically the host material for this research: graphite. Carbon is the sixth most abundant material on earth, over three times more abundant than silicon [4], and is the basis of life as we know it. It can commonly be found in a solid state in coal deposits but must be processed into a form suitable for commercial use. Five of the different allotropes, or descriptions, of carbon are amorphous, diamond, fullerene, nanotube, and graphitic.

Amorphous carbon is formed when an organic material is burned without enough oxygen for the material to burn completely [4]. Other variations of the carbon structure are fullerines, derivatives of the Buckminster Fullerine or C_{60} molecule and single and multi-wall nanotubes—rolled sheets of graphene, the hexagonal form of carbon. Diamond, another of the carbon allotropes, is one of the hardest substances known. Although diamond and graphite possess very different physical properties, graphite and diamond only differ in their crystalline structure [5]. The final allotrope of carbon, graphite or graphitic carbon, is one of the softest as well as stiffest materials known due to anisotropy within the crystal lattice, and is primarily used as a lubricant.

1.2.3 Graphite

Graphite is the host material in the investigation of the PECT effect. The hexagonal form of graphite is the equilibrium state of carbon over a large range of pressures and temperatures, including at standard temperature and pressure. Most

graphite is polycrystalline in nature and has many flaws at the grain boundaries. The

crystallite size, in most cases is very small, up to a maximum of 10 μm. These highly

ordered graphites, typically formed through chemical vapor deposition, are of the most

interest in this research as a host for intercalation, as they will reduce distortions due to

polycrystallinity in the final structure.

The nature of the graphite structure facilitates the PECT effect during

intercalation. The crystalline structure of graphite has four atoms per unit cell. In the "c"

crystalline direction, the substance is extremely soft, while in the basal plane containing

the a1 and a2 directions, the structure of graphite is stiffer than diamond, with a Young's

modulus of 1060 GPa. Figure 1-1 shows a graphical representation of a single plane of

graphite and the corresponding axes.
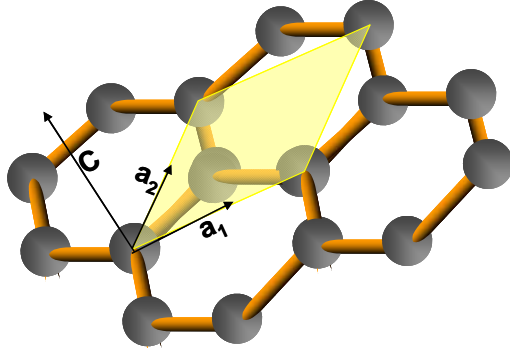
Figure 1-1: Graphical representation of a single plane of graphite and its associated axes.

The differences in the stiffness of graphite with changing crystal orientation are

caused by the anisotropy of bonding in the crystalline structure. This in turn is caused by

the way in which the orbitals of the individual carbon atoms bond to each other. The s

orbital mixes with two p orbitals, and each of the new three sp^2 orbitals point to one of

the three directions in the basal plane, 120° apart. Three electrons occupy these sp^2

orbitals and one electron occupies the *p* orbital which is directed perpendicular to the basal or a-plane. A graphical representation of this bonding process is presented in Figure 1-2.

In graphite, carbon atoms are bonded by three σ bonds, in which electron density lies between two atoms, and one π-bond, in which the charge density is concentrated above and under the basal plane perpendicular to the atomic bond. In the ideal graphite plane, there is no preference as to which atom the *p*-electron bonds with. The π-bond is formed with all three neighbors. This π-bond is delocalized and is thus weaker than the σ bonds in the basal plane. The *p*-electron can move more freely and contributes to conduction, and is a major contributing factor to the changes in the basal plane of graphite that cause the PECT effect to occur. Furthermore, this delocalized π-bond stabilizes the structure forming the familiar hexagonal planar structure of graphite [6].
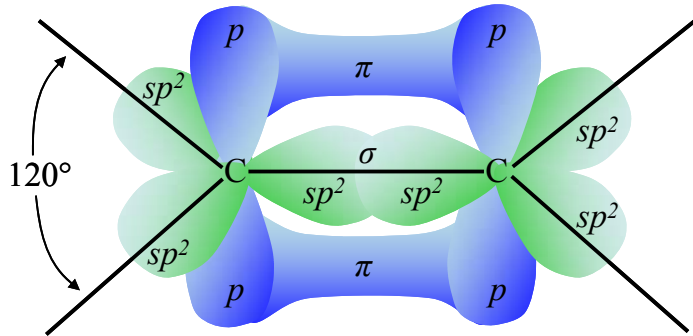
Figure 1-2: Graphical representation of C-C bonds in graphite. Adapted from [6,7].

The graphite crystal is composed of sheets of hexagonal graphite, or graphene, held together by van der Waals forces. Since van der Waals forces are 50 times weaker than π or σ bonds, this causes the graphene planes, separated by an equilibrium distance of 3.34 Å in the ideal graphite crystal, to be inherently weak mechanically in the c-direction [8]. Separating graphene planes slightly strengthens the π-bonds, while bending

or distorting of the graphene plane weakens the π-bonds tending to promote bonding perpendicular to the basal plane. The effect of these two interactions makes commercial highly-oriented pyrolytic graphite (HOPG) samples easy to cleave with common household tape. The cleavings can be used to expose a fresh surface of graphene for use in experiments and make intercalation experiments with thin samples possible.

1.2.4   Graphitized Carbon Fibers

Graphitized carbon fibers have similar characteristics as HOPG. Carbon fibers are well characterized, and can be used as a basis of this research due to the lack of processing steps required to integrate a carbon fiber into a MEMS actuator. They are a unique form of carbon where filaments are drawn, carbonized, and then graphitized. A precursor material, such as a polyacrylontrile (PAN) compound or tar pitch is extruded through a spinneret, heated to leave nearly pure carbon, and then heated again to form graphite planes, while tension is applied to the fiber to orient the graphite planes along the length of the fiber

Graphitized carbon fibers are created with a high degree of order along the length of the fiber, yielding single axis ribbons of polycrystalline graphene which are oriented along the lengh of the fiber. This axis is much like that of HOPG, but predominantly in a single direction instead of oriented in a planar fashion as seen in HOPG. Carbon fibers have been made by chemical vapor deposition (CVD), physical vapor deposition (PVD), carbonization of precursor fibers that cannot be fused (infusible), and carbonization of fusible precursor fibers.

Bacon's discovery of highly graphitic, nearly perfectly oriented graphite "whiskers" formed by PVD in a carbon arc [9], promoted the evolution of carbon fiber

8

technology to produce a very stiff fiber with a high Young's modulus. PAN and liquid crystal intermediate phase (the mesophase) pitch tar graphitized fibers are the two general types of graphitized carbon fibersavailable today. Although initially PAN fibers were stronger due to a defect which formed a radially expanding trench in pitch fibers, this defect no longer exists today and both provide very strong fibers. Pitch-based fibers, however, are more attractive to this research due to their more highly oriented nature. Current high-modulus pitch fibers are composed of a very fine zig-zag structure, where each plane in the structure is normal to a surface of the fiber, but generally radially contiguous along the length of the fiber as presented in Figure 1-3. These fibers are capable of achieving ultra-high Young's modulus (227 GPa), and high electrical (1000 S/cm) and thermal (100-600 W/m-K) conductivities [9].

Figure 1-3: Cross-sectional scanning electron microscope image of pitch-based P-100 carbon fiber showing zigzag structure [10].

1.2.5 Intercalation in Graphite and Graphitized Carbon Fibers

In graphite, molecules such as water will spontaneously intercalate into graphite. Other molecules require electrical potential or an oxidant as stimulus to promote intercalation of the intercalant species into the host. The anisotropy previously discussed makes graphite an excellent host, causing the stiff planes of graphene to be moved apart by the intercalant during intercalation. The stage of intercalation defines the number of graphene sheets between galleries (areas between graphene sheets) that are filled with intercalant. Stage 1 systems are referred to as fully intercalated. A graphical representation of intercalation stages is presented in Figure 1-4.
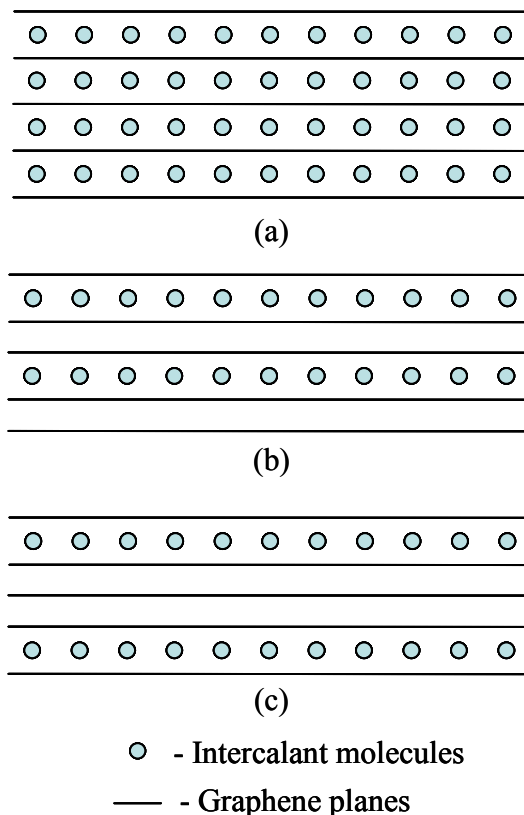
Figure 1-4: Stages of intercalation (a) stage 1 (b) stage 2 and (c) stage 3 intercalation.

10

During the course of intercalation in graphite, the intercalant will stage into the gallery spacing between graphite planes. This staging begins at high stage, where there are many graphene planes between each filled gallery. As the intercalation reaction in the graphite progresses, the compound will transition to stage 3, stage 2, and finally stage 1 intercalation once the highest potential is reached. Thus, in an electrically stimulated intercalation reaction, stage 3 intercalation will require less applied voltage potential than stage 1 intercalation.

This research is primarily designed to create an actuator using the PECT effect in intercalated carbon, and as such the logical choice is to use a compound where intercalation can be controlled through an applied voltage potential. There are a few choices, including NaCl and H_2SO_4. Vogel hypothesized that stronger acids lead to enhanced conductivity in the graphite due to greater fractional charge transfer, as discussed in Section 1.2.6 in this document [11], and strong Brönsted acids should lead to lower time constants and greater strain. One such Brönsted acid, H_2SO_4, is well characterized in the literature [3,11-19], was used in Vogel's initial experiments [2], and will be used as the basis of this research.

To intercalate graphite in this electrochemical H_2SO_4-graphite system, an electrolysis voltage must be applied between the graphite (anode) and another electrode, normally made of a metal inert to the intercalant such as platinum (cathode). As voltages increase, intercalation progresses through different stages, ending in stage 1 intercalation, where each graphene sheet has intercalant between itself and the next sheet [21]. Previous research in electrically stimulated graphite-H_2SO_4 systems with a saturated calomel electrode (SCE) as reference showed high stage intercalation below 500 mV of

11

potential, stage 3 between 0.5 and 0.55 V, stage 2 between 0.55 and 0.83 V, and stage 1

above 0.83 V when intercalated under a constant current using cyclic voltammetry

[15,17,18]. This corresponds to a potential against a platinum electrode of 0.94 to 0.99 V

for stage 3, 0.99 to 1.27 V for stage 2 and above 1.27 V for stage 1 H_2SO_4 intercalated

graphite [18].

Staging is an important part of the PECT process, and can be seen in results of

Cyclic voltammetry performed by Shioyama *et al.* among others [15]. Shioyama's team

researched the stage transition of low stage graphite-H_2SO_4 electrochemical intercalation

[15]. Figure 1-5 presents a typical cyclic voltammogram on HOPG in 18 mol/L of

sulfuric acid at a sweep rate of 10 mV/sec, using an SCE as a reference electrode.
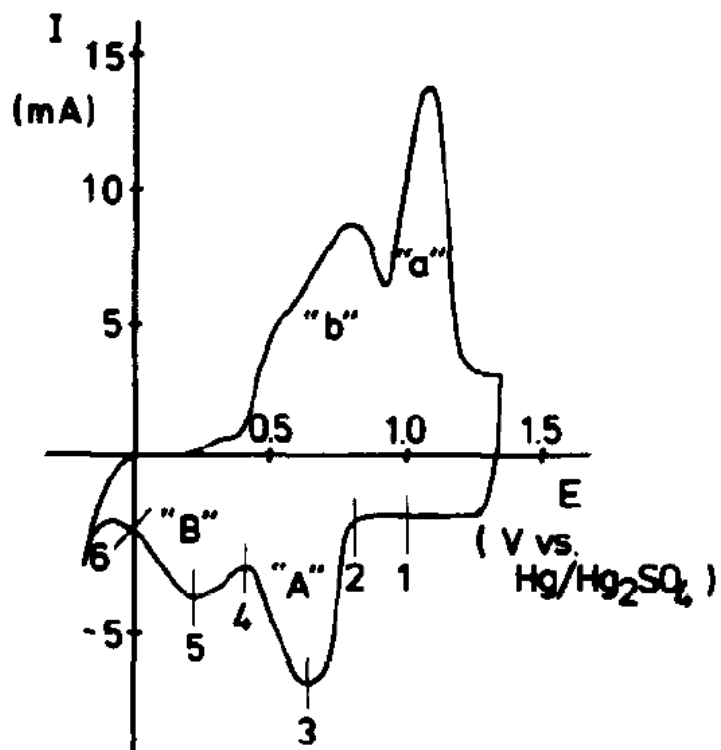
Figure 1-5: A typical cyclic voltammogram for HOPG dipped in 18 mol/L sulfuric acid electrolyte at a sweep rate of 10 mV/sec [15].

In this diagram, peak "a" on the upper portion of the curve, or the forward potential sweep condition, corresponds to a stage 1 graphite-H_2SO_4 compound. Since this is the lowest carbon fraction, it takes the most work to electrochemically stimulate the graphite-H_2SO_4 compound to stage 1 and thus occurs at the highest potential voltage. Peak "b" is comprised of peaks due to conversion from stage n to stage m, where $n \geq m \geq 2$. On the reverse potential sweep, peak "A" corresponds to the decomposition of the stage 1 compound toward stage 2 while peak "B" is the degradation of stage m to stage n intercalation [15]. There is a difference in the voltage locations in this research for staging and destaging, corresponds to the adsorption rate for the intercalant in the graphite-H_2SO_4 compound.

Staging and the corresponding strain and conductivity effects in a graphite-H_2SO_4 compound are completely reversible, as evidenced by x-ray diffraction and raman spectroscopy performed on samples before, during and after intercalation as will be discussed later in this Chapter.

In conjunction with staging, intercalation involves transport of the intercalant species to the host, adsorption and insertion of the intercalant at the basal plane edges of the host surface and transport within the host. Macroscopic effects such as gross elastic distortions of the host polycrystallinity also complicate the behavior [21]. For sulfuric acid (H_2SO_4) acting as the intercalant, the interplanar distance of the polycrystalline graphene planes in HOPG can stretch from the 3.34 Å equilibrium c-axis spacing to as much as 7.98 Å, relaxing to approximately 7.88 Å in stage 1 intercalated graphite [20]. Expansion perpendicular to the strong basal plane (a-plane) bonds has been discussed as

13

an actuation mechanism previously [22,23], and is thus not investigated in this research. Distortions caused *within* the basal plane are the focus of this dissertation.

1.2.6 The Redox Process in the PECT Effect

Consider galvanostatic oxidation in the graphite-H_2SO_4 reaction. The electrically stimulated graphite anode oxidizes when potential is applied, losing electrons. In equilibrium, sulfuric acid contains H_2SO_4, HSO_4^- ions and H^+ ions. The bisulfate ion then is oxidized and donates an electron to the graphite, leaving an oxidized bisulfate radical (HSO_4). The reaction in stage 1 intercalation occurs [15,16]:

$$24C + 3.5\ H_2SO_4 \rightarrow C_{24} \cdot HSO_4 \cdot 2.5H_2SO_4 + H+ + e^- \qquad (1\text{-}1)$$
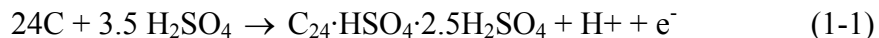
where, at this highest energy state, there are 24 carbon atoms per oxidized bisulfate ion. During the oxidaiton of the bisulfate ion to a bisulfate radical, localized strain is generated in the lattice while effectively prying the gallery spacing apart, and progressing until equilibrium is reached at the center of the sample. Oxidation with overpotential could reduce the number of carbon atoms in Equation 1-1 to as little as 18, while "overoxidation" is occurring [20], however each stage is generally characterized by bisulfate-carbon bonding in multiples of the 24 atoms per bisulfate radical [16, 18]. In a stage 2 graphite-H_2SO_4 compound, there are 48 carbon atoms per oxidized bisulfate radical, and a reduction in the required potential for this stage. In a stage 3 graphite-H_2SO_4 compound, the number increases to 72 with the required potential to complete this work lower again than stage 1 or stage 2 compounds.

Further anodic oxidation of the stage one compound ($C_{24} \cdot HSO_4 \cdot 2.5H_2SO_4$) results in the "ionization reaction of carbon atoms in the graphite basal plane" with bisulfate radicals in the solution [15]. Reversible bonding of one oxygen atom within a further

oxidized bisulfate radical occurs at small potentials over that required to reach stage 1 intercalation. This oxygen atom disassociates from the bisulfate radical and forms carbon-oxygen bonds at higher potentials causing irreversible damage to the carbon lattice.

1.3 Electrical Conductivity in H_2SO_4 Intercalated Graphite

Graphite has very high mobilities, with electron mobility of 2×10^4 cm^2/V-s and, even more impressive, a hole mobility of 1.5×10^4 cm^2/V-s in the planar direction of the structure, but only 100 cm^2/V-s electron and 90 cm^2/V-s hole mobilities between the planes of the structure [24]. In comparison to traditional semiconductors, silicon has an electron mobility of 1350 cm^2/V-s, and a hole mobility of 480 cm^2/V-s while gallium arsenide has an electron mobility of 8500 cm^2/V-s and hole mobility of 400 cm^2/V-s for intrinsic material [25]. The high mobilities caused researchers to investigate ways of taking advantage of the π-bonded electron to decrease the resistivity of the graphite structure.

Electrical conductivity in graphite changes during H_2SO_4-graphite electrochemical intercalation. As discussed previously, the π-bonded p-electron in the graphite structure can move freely and contributes to conductivity in the material. The bisulfate ions in an H_2SO_4 solution gravitate toward the graphite anode while the hydrogen ions move to the non-reactive cathode. The graphite's π-bonded electrons are being stripped causing a lack of electrons in this layer during the electrolysis process. This causes bonds to form between the bisulfate and the carbon. The bonding contributes to the in-plane conductivity, with the high mobility of graphite causing it to act like a very highly doped p-type semiconductor. The conductivity of the graphite drastically

15

increases as more ions are formed and more π-bonded electrons are donated to balance the ionic charge of the bisulfate. At higher intercalation voltages, however, overcharging becomes an issue and oxygen atoms bond to the surface of the graphite on those same π-bond sites, which begins to reduce the conductivity of the graphite and eventually leads to overoxidation, where the conductivity of the material drastically decreases. Figure 1-6 presents experimental results that illustrate this effect on a 2 cm long single strand of Thornell P-100 graphite fiber.
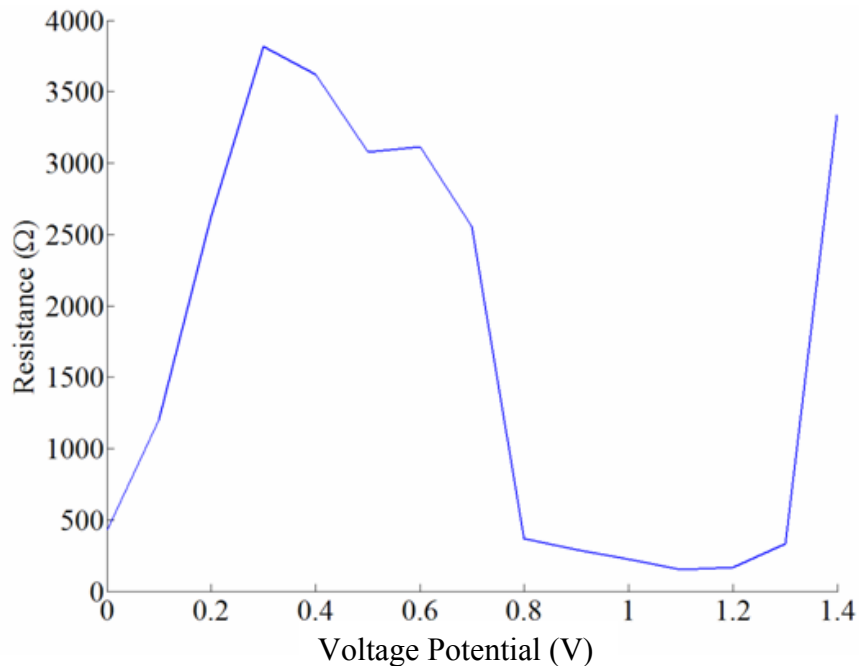
Figure 1-6: AFIT 50 Hz resistance data for intercalation of graphite fiber in sulfuric acid for 10 μm diameter, 1 cm long P-100 carbon fiber with 50% of the length intercalated.

As presented in Figure 1-6, the resistance decreases as intercalation voltages increase, to a point where, at approximately 1.2 volts of electrolysis voltage, the oxidation begins to reduce the mobility of the carriers in the compound by making more and more π bonds unavailable for use in balancing the charge of the bisulfate ions. The

effect becomes more pronounced as voltages increase, and eventually overcome all of the benefits to conductivity of intercalating the graphite fiber with sulfuric acid. This initial data shows a large increase in resistance upon the application of voltage potential. This increase due to an unknown factor, but could be contributed to from any number of factors including the length of fiber intercalated, strain induced etc. The interesting response comes from noting the reduction between 0 V applied potential and between 0.8 and 1.2 V of applied potential, where the resistance decreases. Also, as expected, at 1.3 V of applied potential and above, the resistance begins to drastically increase, illustrating that oxidation of the carbon surface is beginning, and confirming the general theory of graphite-H_2SO_4 conductivity changes.

1.4 The Piezo-electrochemical Transducer Effect in Intercalated Carbon

The PECT effect in intercalated carbon uses the same mechanisms that cause a change in the conductance of intercalated graphite. This effect leverages the change in length of the strong σ-bonds in the graphite lattice during this process that produce strain. Although interplanar expansion in intercalated graphite does occur, this research does not measure these changes and is instead focused on net σ-bond length changes. In n-type graphite intercalation compounds such as potassium and lithium, reduction intercalation occurs. In potassium, this causes basal plane expansion based on the stage of intercalation causing the C-C bond length changes: (stage n) = $(1.4203 + 0.0113/n)$ Å [26]. In p-type graphite intercalation compounds including NaCl and H_2SO_4, the reverse is true, and the C-C bond distance shrinks instead of lengthening, and they only work electrochemically, vice the spontaneous intercalation of lithium.

If bond length shortening due to the single oxidation of bisulfate ions is the only source of change, the C-C bond distance would give a maximum of approximately 0.2% strain. This maximum value was calculated by applying a geometric analysis in the a1 (or a2) direction in graphite and determining the resultant total length due to the contributions of the bond length components in that direction. Initial experimentation by Dr. Vogel indicate that a strain of up to 2% is possible, while limited initial experimental setup in this research only discovered a 0.2% strain. Shortening caused by bonding to the bisulfate radical cannot thus be the only contributing factor. Further oxidation of this radical causes oxygen bonds to form on the π bond sites in the graphite lattice. These bonds effectively "tent" the graphite lattice, shortening the bond lengths in the basal plane from 1.4203 Å to that of graphite oxide, approximately 1.13 Å [27]. Thus the change in length of the sulfuric acid intercalated carbon fiber appears to be a combination of reversible shortening of carbon bonds in the graphite lattice due to both mechanisms.

The further oxidation of the bisulfate radical and subsequent bonding and tenting the carbon lattice is reversible, confirmed by Maeda's work [28]. His team tested H_2SO_4 intercalated carbon fibers at 0.0 to 1.4 V, by using Raman spectroscopy. A sharp Raman band at 1580 cm^{-1} and a weak band at 1360 cm^{-1} were observed and this corresponded to the same sample before intercalation. However, when intercalated from 0.0 to 2.3 V, fibers increased the relative intensity of the 1360 cm^{-1} band, indicating that the C-O bonds caused irreversible defects in the graphite layer planes at a voltage greater than 1.4 V, and is confirmed at 2.3 V [28] where the bisulfate radical dissociates and the free oxygen atom bonds permanently to the graphite lattice. The PECT effect exhibits this same characteristic, and allows a graphite fiber to be intercalated to induce strain, and

deintercalated to relax the fiber to its original length if kept under the critical voltage that causes irreversible damage to the graphite lattice. In this research, irreversible damage occurs when over 2.0 V of potential is applied between the fiber and cathode in H_2SO_4.

1.4.1 Carbon-Carbon Bond Theory

A groundbreaking study using x-ray diffraction by Nixon and Parry in 1969 [26] proved changes in the carbon-carbon bond length change during intercalation in graphite. This study involved potassium-intercalated graphite and was based on the study of the staging of potassium intercalant fully investigated by the duo the previous year. Initial experiments of stage 1 potassium intercalated graphite in their study confirmed that the transfer of electrons to antibonding states does in fact increase the carbon-carbon bond length, and also indicated that the increase was surprisingly large, on the order of 0.01 Å. Further studies explored methods to accurately measure the change in carbon-carbon bond length for higher staging numbers [26]. Other intercalants such as the compounds NaCl, HCl, H_2SO_4, and Li, whether acceptor or donor compounds, can be used to increase or decrease the carbon-carbon bond length in intercalated graphite.

Potassium graphites intercalate naturally, as opposed to electrochemically as in sulfuric acid intercalants. However, the staging of potassium requires precisely controlled heating over a period of time to ensure the level of staging. To that end, researchers used a proportional temperature controller system to stabilize their furnace to within 0.25 °C. This improvement allowed the investigators to study stage 5, and stage 6 which had been previously impossible due to the strict temperature range required for this stage. Overall, 40 samples were prepared and sorted by quality of diffraction photographs, and the two best samples for each stage were selected for further study [26].

19

Data from these experiments led Nixon and Parry to hypothesize that electrons transferred from the potassium enter the upper π band (or conduction band) of the graphite, and since these are antibonding states, the interaction between carbon atoms was weakened, leading to the observed increase in bond lengths. Furthermore, they suggest that "each intercalant layer in stage n must transfer an amount of charge $q(n)$ to the graphite and the consequent change in the carbon-carbon bond length must depend in some way on the total charge transfer" [26]. Finding that the relation is linear, they also suggest that once the Fermi level has passed the region of band overlap, there must be a simple relation between the Fermi level and the carbon-carbon bond length that leads to a nearly linear relation between the bond length and the total charge transfer [26].

Based upon data from Nixon and Parry's work, Pietronero and Strässler [29] began to explain the mechanism behind the antibonding states causing expansion or contraction. They followed the tight binding method to write the total energy per bond between nearest neighboring atoms. Since Nixon and Parry's research determined that the lattices were hexagonally symmetric, no special indices were needed to denote a nearest neighbor, since all nearest neighbors are equidistant. They noted also, that systems with the same charge on the p orbitals but different geometries had different values for the bond order. Compiling data from Nixon and Parry and four other studies, they found measured differences between the carbon-carbon bond lengths in lithium, potassium, cesium, nickel chloride, iron chloride, and arsenic fluoride, a range of intercalates that are strong donors to acceptors. This data, presented in Figure 1-7, they shows that graphite expands if donors are added and shrinks if acceptors are added, counter to what happens in small molecules such as benzene and ethylene [29]. The main difference between

20

graphite and these small molecules is that a net charge appears on the carbon atoms in graphite, while the carbon atoms in the small molecules are neutral and only the bond order is changed [29]. The equation these researchers derived became a length change equation, which depends on the total energy per bond, including both π and σ electrons between nearest-neighboring atoms. This analysis, neglected the minor contributor of the interlayer bonding, which should cause a small carbon-carbon bond length shortening when successive layers of graphene are pushed apart during intercalation. They also computed the total force constant and can from the elastic constants of graphite or the analysis of small molecules extrapolated to the bond length of graphite. Both methods yielded a force constant of 45 eV/Å^2 [29].
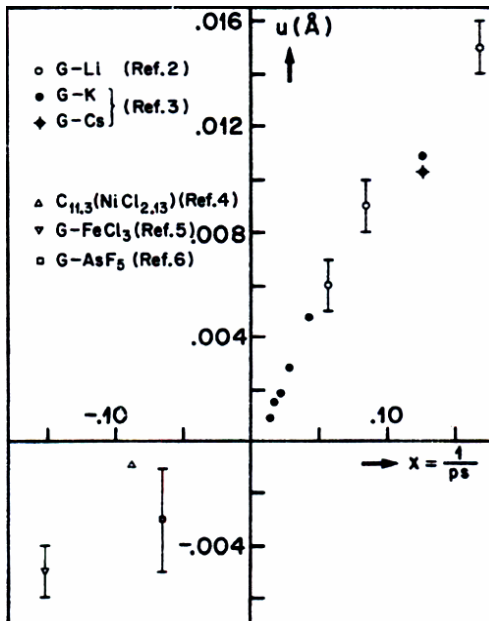
Figure 1-7: Experimental values for the bond-length change u for various intercalation compounds plotted as a function of the ratio of the number of intercalant molecules to the number of carbon atoms in a given compound [29].

Pietronero and Strässler used Slater orbitals to evaluate the atomic potential and change therein with an exponent optimized for the carbon atom which resulted in a final formula for stage 1 potassium intercalated graphite.

$$u(1) = 0.157 f_c + 0.146 |f_c|^{3/2} + 0.236 f_c^2 \text{ in Å} \tag{1.1}$$

where $u(1)$ is the bond length in a stage 1 compound, and f_c is electronic charge. Since f_c $\leq 1/6$ in this case, the leading term is the linear one that is due to effects beyond the *rigid-bond model* [29] and this is the contribution that results in the physical effect of bond expanding for donor intercalates and bond shrinking for acceptor intercalates.

Further research in the area was performed by Chan, Kamitakahara, Ho, and Eklund in 1987 [30], using new neutron-diffraction data and reexamining older data, supporting Pietronero and Strässler's work but achieving different quantitative results. They also claimed to be able to extend their calculations to obtain detailed information on the effects of charge transfer on phonon frequencies, elastic constants, and electronic wave functions [30]. The basic unit used in this investigation is two consecutive graphite layers in an AA stacking sequence such that the unit cell has two carbon atoms and one intercalant ion with charge Z. "For negative Z, stimulating acceptors, Z/2 valence electrons are depleted from each C atom. For positive Z, stimulating donors, the extra Z electrons per unit cell will be almost entirely donated to the C atoms because the intercalant potential (~ Z/r) is too weak to compete with the much stronger C potential" [30]. Calculations for these functions were expanded using linear combinations of atomic orbitals fully self-consistently with 32 momentum points in the irreducible portion of the Brillouin zone [30]. This model works very good for stages 1 and 2 where each layer of graphite has a layer of intercalant adjacent to it, but in stages 3 and beyond, the

assumption that interior and bounding layers have the same in-plane lattice parameter, or that the in-plane charge-induced lattice strain is shared equally throughout the entire material must be used [30]. Differences between the results of the two theories are presented in Figure 1-8.
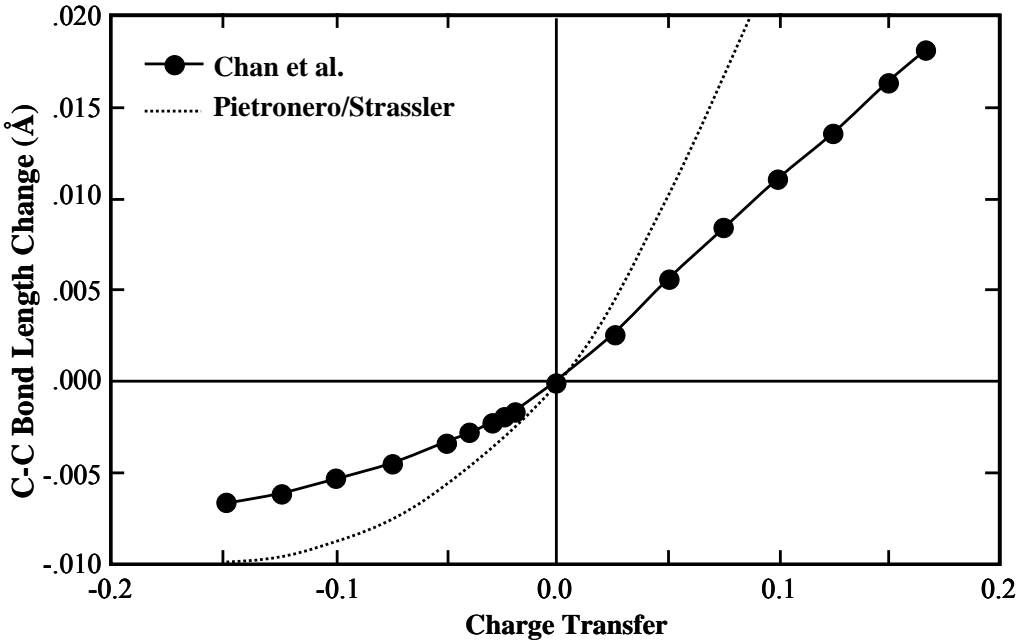
Figure 1-8: Dependence of bond-length change on charge transfer, as calculated in Chan et al. (solid line) and by Pietronaro and Strässler (dotted line) [30].

With sulfuric acid graphite intercalation compounds, the electrochemical method allowed Chan *et al.* to place the intercalation compounds directly on the charge-transfer scale. When one electron flowed through the external circuit of the sulfuric acid intercalation compound, one is transferred from the graphene layers to the intercalated molecules, leading to the oxidation of the bisulfate ions formed during this process [30]. Since neutron diffraction was affected by the low absorption of the neutrons in their test cell and intercalant liquid, the results were relatively low-resolution and limited the accuracy of Chan's experiment.

Using alkali-metal graphite intercalation compounds as donors, for stage 2 and higher compounds, their experimental points fell directly on the line calculated from their theory. This is "strong evidence that the theory applies to donor as well as acceptor (graphite intercalation compounds), and that the alkali-metal atoms almost completely donate their valence electrons to the graphite host" [30]. However, for stage 1, the data implies that the alkali-metal intercalates are not completely charge balanced by the graphite lattice. Experimental data for metal halide graphite intercalation compounds comes close to the theoretical model developed by Chan *et al.* as presented in Figure 1-9 [31]
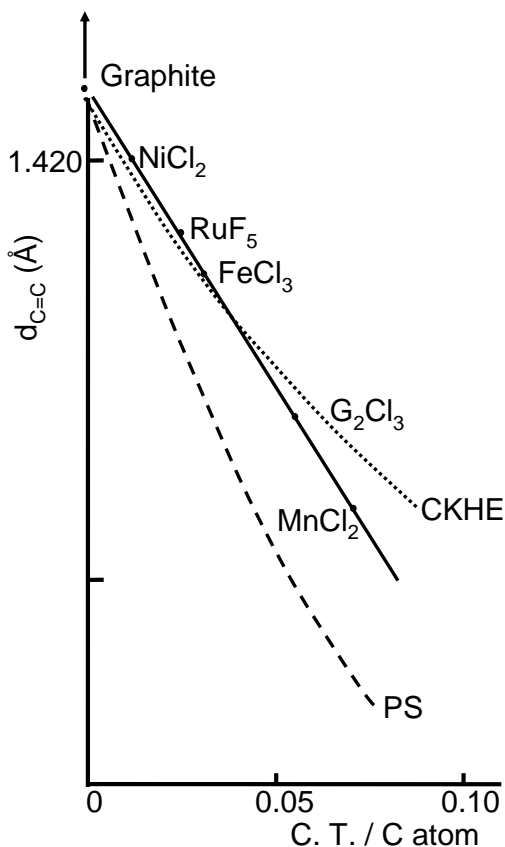
Figure 1-9: Charge transfer per carbon atom as a function of carbon-carbon bond length. Solid line: Empirical relationship based on data from several metal halide graphite intercalation compounds, dashed lines: theoretical calculations from Pietronaro and Strässler (PS) and Chan et al. (CKHE) [31].

1.4.2   C-O Bond Theory

Under anodic oxidation of graphite in H_2SO_4, sulfuric acid and bisulfate ions are drawn into the gallery spacings between graphene planes. Experiments have shown that other reactions also occur at various points in the charging cycle [32]. These phenomena were measured using a combination of methods, including conductivity along the basal plane of the graphite, coulometry, x-ray diffraction, and Raman spectroscopy. These results suggest that at lower voltage potentials, three distinct phenomena occur. The first phenomenon is "overcharging" where the bisulfate ions and hydrogen ions polarize, causing an effective acceptor dopant in the graphite. The second is peroxidation of the bisulfate ion to the persulfate ion $(S_2O_8^{2-})$. Finally, the third phenomenon is "overoxidation" involving the direct oxidation of the graphite, forming covalent (π) carbon-oxygen bonds which form scattering centers and degrade conductivity [20].

Strong oxidizers, such as sulfuric acid, or fluorinating agents can produce these covalent solids in which the transferred charge is localized in either carbon-oxygen bonds or carbon-fluorine bonds, also causing the puckering or tenting of the planar nature of the graphite lattice. This effect happens once more than one electron per 24 carbon atoms is transferred to the graphite lattice during electrolytic intercalation [12]. This is evidenced by the reduction in conductivity in the overoxidation mentioned previously, from the introduction of scattering centers at those carbon-oxygen bond sites. This oxidation, or forming of the covalent bonds in the hexagonal structure actually decreases the planar dimensions of the lattice, reducing the 1.53 Å carbon-carbon bonds to ~1.45 Å, and causing the puckering or tenting of the carbon structure [27]. This bonding causes the

shortening of the carbon-carbon bonds and results in a strain in the basal plane of the graphite.

Raman spectroscopy on carbon materials shows two bands at 1580 and 1360 cm^{-1}. The peak at 1580 cm^{-1} corresponds to the in-plane motion of carbon atoms in the hexagonal graphite layers, and the 1360 cm^{-1} band corresponds to the presence of structural defects in the graphite layer planes. When fibers are intercalated from 0.0 to 1.4 V, the spectrum when compared to the original spectrum of test graphite, does not change, however at higher electrolysis voltages, a marked increase of the relative intensity of the 1360 cm^{-1} band is observed [28]. The formation of graphite oxide can become severe at potentials over 2 V, but at lower potentials, any appearance of carbon-oxygen bonds in the graphite lattice is completely reversible as discussed in Chapter 1.

The tenting of the basal plane in graphite due to reversible C-O bonds forming on the further oxidized bisulfate radical, which contributes strain for each bonding site in the graphite lattice. This oxidation becomes irreversible at potentials over 2 V when π-bonds form between a dissociated oxygen atom from the bisulfate radical. Prior to dissociation, the mechanism is a valid contributor to the total strain induced in the graphite lattice during intercalation.

1.4.3   Combined Bond-Length Change in Graphite-H$_2$SO$_4$ Compounds

While C-C and C-O bonding are two distinct theories of strain generation in the basal plane of graphite, both occur simultaneously, and thus must be evaluated together. Taking into account the stage 1 graphite-H$_2$SO$_4$ compound, the carbon-carbon bond distance will change from 1.53 to 1.52 Å [26]. Since there are 24 carbon atoms per HSO$_4$

molecule in the stage 1 compound, the total length along the a_1 or a_2 axis due to the charge transfer from this empirical data is governed by the simple geometric relation:

$$L = 1.52 \cdot \cos(\theta) + 2 \cdot 1.53 \cdot \cos(\theta) \ (\text{Å}), \qquad (2\text{-}1)$$

where L is the length along either axis in the basal plane and θ is the angle from the bond to the axis, which projects the length contribution of each bond onto the specific a-axis. Compare this number to the same relation without the bond-length change:

$$L = 3 \cdot 1.53 \cdot \cos(\theta) \ (\text{Å}). \qquad (2\text{-}2)$$
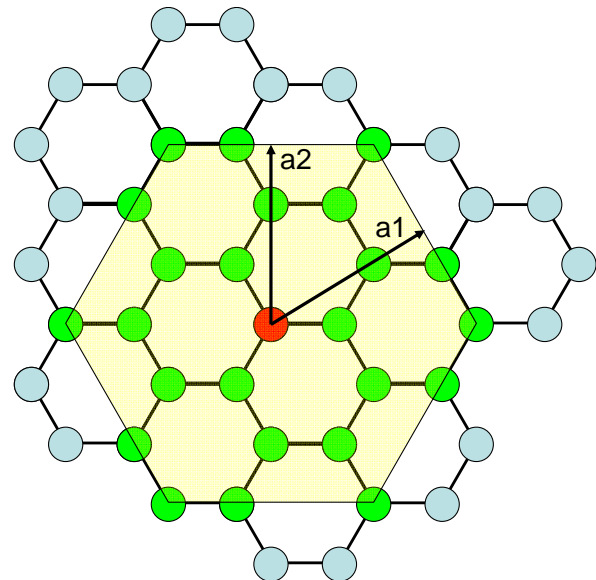
Figure 1-10: 24-atom "unit cell" which graphically represents the atom interacting with HSO_4 in stage 1 graphite-H_2SO_4 compounds.

The total strain (ε) produced in the stage 1 graphite-H_2SO_4 compound is determined by the change in the length (L) over the original length (L_0). This formula can be expressed, in a simplified form as:

$$\varepsilon = \frac{L - L_0}{L_0} = \frac{(1.53 - 1.52) \cdot \cos(\theta)}{3 \cdot 1.53 \cdot \cos(\theta)} \ (\text{unitless}). \qquad (2\text{-}3)$$

For the stage 1 compound, this corresponds to a strain of 0.00217. For stage 2 compounds, it is similar but the there is now only one bond-length change per 48 carbon atoms, yielding a strain of 0.00109, since there are two net cells of 24 carbon atoms between two planes only bonded to one HSO_4. This can be extrapolated through stage 3 and higher compounds easily.

The strain produced by the carbon-oxygen bond "tenting" is given as 0.08 Å [27]. As such, the strain can be calculated similarly to Formula 2-1, but since the exact number of carbon atoms per bond site is not know, it is necessary to calculate based on a varying number of carbon atoms. Figure 1-10 shows the 24-atom unit cell, which is 3 atom rings away from the interacting carbon atom. Using this ring analysis, where n is the number of rings from the center; it is possible to calculate the strain produced from oxygen bonds for atoms grouped in this manner. The results of these strain calculations are presented in Table 1-1.

Table 1-1: Strain produced by C-O bonding by ring number from centrally tented carbon atom.

Ring Number (n)	Number of C atoms	Strain (ε) (unitless)
1	3	0.05228
2	12	0.02614
3	24	0.01742
4	38	0.01307
5	59	0.01045
6	83	0.00871

In stage 1 graphite-H_2SO_4 compounds, Vogel proposed a maximum of 2% strain [2]. To achieve this amount of strain, neither method alone accounts for this number, but when used in conjunction with one another, in a C_{24} bonding scheme, with both charge-induced carbon-carbon bond length shortening, and carbon-oxygen bond tenting, the

composite strain becomes 0.01959, which is in close agreement with the maximum strain predicted by Vogel. Since the oxygen bonding only occurs after excess charge is injected into the system, the expectation is a wave through 1.4 V with a nearly linear region between 0.6 and 1.3 V of potential, where excess charge is formed and oxygen bonds begin occurring. At this point, an exponential curve will occur as oxygen atoms bond to sites in the graphite lattice.

1.5 Summary

The PECT effect uses the structurally strong and highly temperature resistant characteristics of graphite to produce a low-power, high-force actuation material based upon changing lengths of bonds in the basal plane of graphite. An electrochemical redox process can be used to control the strain produced in PECT graphite actuators. PECT based devices could revolutionize the field of MEMS due to their superior qualities in almost all aspects of actuation.

Chapter 2 of this dissertation details a comprehensive literature review of traditional MEMS devices and a review of actuation methods to include intercalated carbon nanotubes, graphite actuators acting in the "c" crystallite direction, and conducting polymers. Chapter 3 of this dissertation describes initial electrical and mechanical experimental results on an intercalated graphite fiber. Chapter 4 encompasses micro-scale experimentation results of the mechanical nature of the PECT effect in graphite fibers while Chapter 5 details the electrical results of the same fiber. Chapter 6 presents a unique method of creating thin-film graphite structures from highly oriented pyrolytic graphite and Chapter 7 concludes this dissertation and gives recommendations for future work.

PIEZO-ELECTROCHEMICAL TRANSDUCER EFFECT (PECT)

INTERCALATED GRAPHITE MICRO-ELECTROMECHANICAL

ACTUATORS

2. Graphite Actuators

Graphite has been investigated as an actuation material due to its superior tensile strength in the basal plane as well as the characteristics that make graphite a good lubricant, namely the softness in the c-axis. Relatively few studies however have used this material as an actuator. Graphite is a proven actuation material with expansion along the c-axis as a method of actuation [33,34], whereas this research is focused on creating actuators using the strong interactions that occur in the basal plane of graphite.

This chapter will first describe MEMS actuators that are current competitors to PECT-based MEMS actuators. It will describe traditional polysilicon MEMS actuators and discuss the commercial polysilicon micromachining process used in conjunction with this research. It will then discuss actuators which use similar mechanisms as the PECT effect, namely electrochemically actuated polymer actuators, carbon nanotube actuators, and intercalated graphite which produces strain normal to the basal plane. It will finally discuss the two theories which contribute to the dimension changes in the basal plane of intercalated graphite, as it applies to the creation of PECT actuators.

2.1 Micro-Actuators

In his address to the American Physical Society on December 26, 1959, Nobel Laureate Richard Feynman predicted the rise of small scale machinery and "a hundred tiny hands" as the method to reduce the size of machinery to as much as 1/4000 scale. He put a $1000 prize for the first person to both build a tiny motor and to write the

information from a book on 1/25,000 scale. The first was met quickly by a craftsman using conventional tools, but did not advance the art. The second was not claimed until 1985 when a Stanford University graduate student, Tom Newman, successfully reduced a paragraph of "A Tale of Two Cities" by 1/25,000 [35]. Feynman envisioned a world where the human hand is too large to fabricate the structures, stimulated discussion and invention, and set the stage for development of modern micro-electromechanical systems (MEMS) [36]. Later, Kurt Peterson predicted that silicon would be used as a material that would revolutionize miniature mechanical devices [37] and a year later, in 1983, Dr. Feynman predicted the genesis of MEMS saying "I believe that with today's technology we can easily – I say *easily* – construct motors one fortieth of this size in each dimension" (10 μm on a side) [38]. He also laid out the process for conventional polysilicon MEMS structures, epitaxial and sacrificial layers [38], which are still used today, using polysilicon, and similarly structured layers, and using electroplating techniques with materials such as nickel. These material layers are grown epitaxially onto the surface of some substrate or formed through an electroplating process which is essentially using a photoresist mold to grow a very tall structure, usually of nickel, onto a substrate.

The two predominant mechanisms for actuation of MEMS devices that have been developed from Dr. Feynman's original challenge are thermal expansion and electrostatic attraction. MEMS actuators powered by thermal expansion can be controlled using one of two main methods. The first, using photonic absorption causes heating due to energy attained from light impinging on the structure. This method is constrained by the external heat source (laser) and the size of the spot available to focus that source.

Thermal expansion utilizing joule heating, or heating via photonic absorption is the most applicable use for these devices and both have been used in chevron actuators [39] as presented in Figure 2-1 and as the locomotive force behind micro-wings [40] designed by Denninghoff, as presented in Figure 2-2.   The most common form of thermally expanding actuators, however, is electro-thermal.   These actuators use either heating elements or joule heating within the device itself to induce strain (or change in length defined as $\Delta L/L$). Of these, the more useful designs utilize a "cold" arm and a "hot" arm to provide differential actuation, and motion either parallel or perpendicular to the substrate of the device.
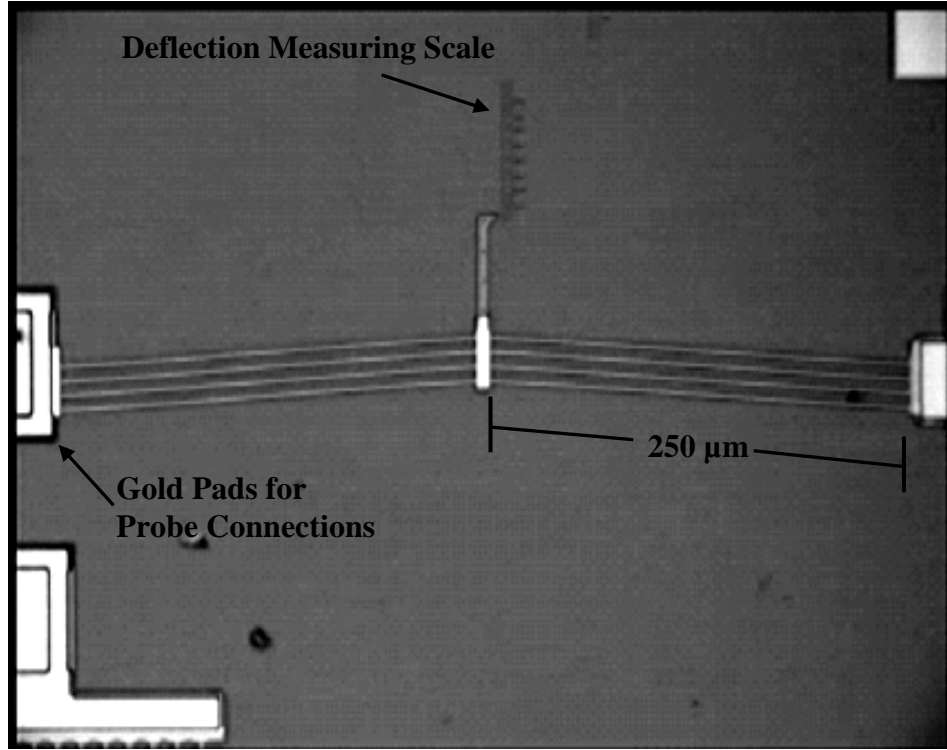
Figure 2-1: Four 250 μm long beam polysilicon chevron test actuators[39]
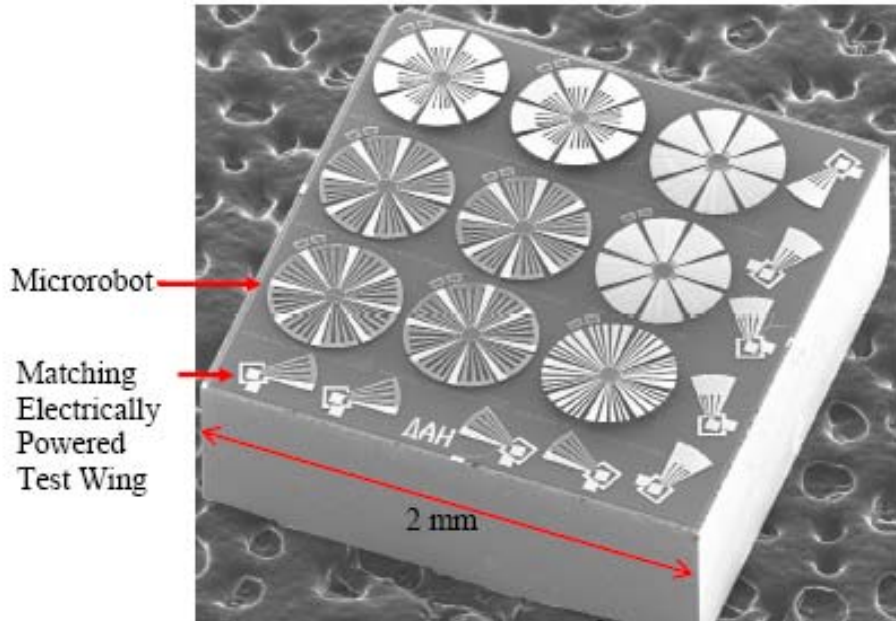
Figure 2-2: Scanning electron micrograph of a 2 x 2-mm^2 microrobot chip containing nine 500-μm robots and matching electrically powered test wings [40].

Figure 2-3 presents a typical electro-thermal actuator which performs work parallel to the substrate while Figure 2-4 presents a design for an electro-thermal actuator that performs work normal to the substrate.
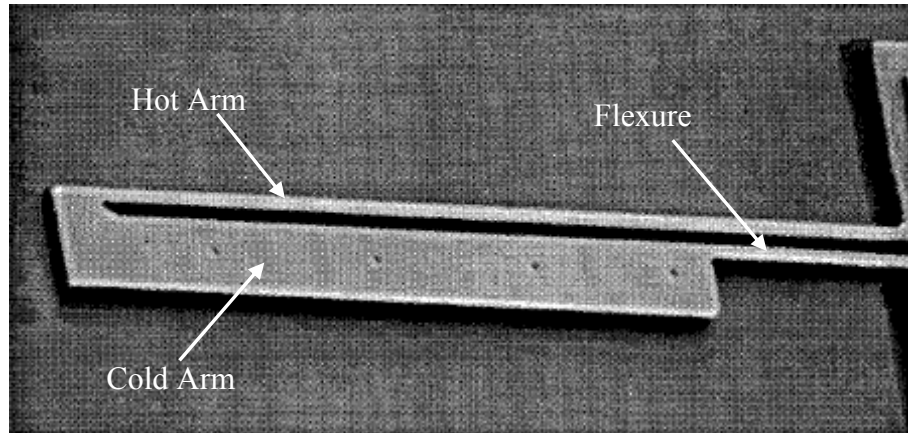
Figure 2-3: Electro-thermal polysilicon single hot arm actuator fabricated in PolyMUMPs run 17. Motion of actuator is parallel to the substrate [41].
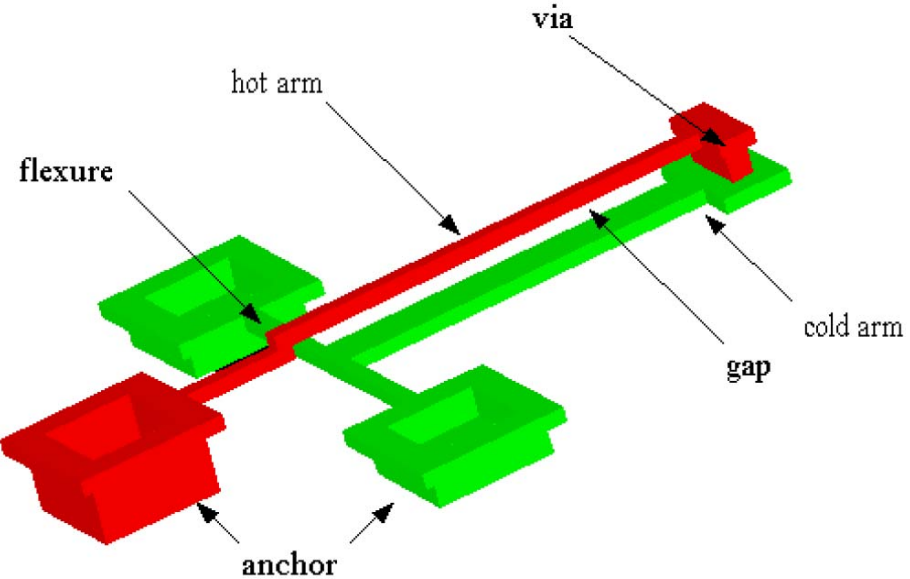
Figure 2-4: MEMS bidirectional vertical thermal actuator [42].

In an electrothermal actuator with a single hot and single cold arm, current travels through the entire circuit, causing joule heating to occur. This heating is inversely proportional to the cross-sectional area of the device. Since current flow is constant, current density in the cold arm is lower and thus it stays cooler than the hot arm, which has a much higher current density. This higher current density causes significant joule-heating and results in an expansion of the hot arm, and thus pushes the tip of the actuator away from the expanding hot arm, usually due to torsional forces. Figure 2-5 presents an example of how a single hot arm polysilicon electrothermal actuator operates. These characteristics apply equally well, albeit with different material parameters, to nickel electroplated/electroformed versions of these devices. Table 2-1presents a summary of typical strain, force and power results from one and two hot-arm electro-thermal polysilicon actuators with a 200-221 μm hot-arm length.
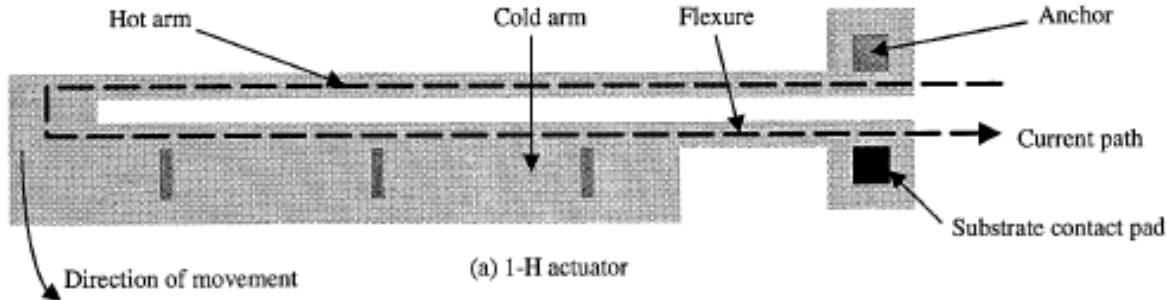
Figure 2-5: Single hot arm electrothermal polysilicon actuator designed for PolyMUMPs® run 17 [41].

Table 2-1: Performance characteristics of typical one and two hot-arm electrothermal polysilicon actuators designed in PolyMUMPs® run 17 [41].

	One hot-arm actuator	Two hot-arm actuator
Maximum Strain	0.00125	0.00201
Maximum Force	11.4 μN	20.5 μN
Power at Maximum Strain	7.64 mW	11.46 mW
Maximum Frequency (air)	12 kHz	17 kHz

2.1.1 PolyMUMPs® Overview

The polysilicon mechanical structures fabricated in this research utilize a commercial micromachining fabrication process as a starting point for integration of polysilicon devices with carbon fibers and HOPG. The Multi-User MEMS Processes, or MUMPs®, is a commercial program that provides cost-effective, proof-of concept MEMS fabrication to industry, universities, and government worldwide. The following is a general process description and user guide for PolyMUMPs, which is designed for general purpose micromachining of epitaxial MEMS devices. The PolyMUMPs process is a three-layer polysilicon surface micromachining process derived from work performed at the Berkeley Sensors and Actuators Center (BSAC) at the University of California in the late 1980s and early 1990s with modifications and enhancements to increase the flexibility and versatility of the process for the multi-user environment [43].

35

PolyMUMPs® is built on a 150 mm n-type (100) silicon wafer of a 1-2 Ω-cm resistivity. A thin layer of silicon nitride is grown on the top side of the wafer to electrically isolate devices from the substrate. Three layers of polysilicon are used for structural layers, with deposited phosphosilicate glass (PSG) as the sacrificial layer. A metal layer of gold is deposited on top of the final polysilicon layers. The deposited oxides can be etched with hydrofluoric acid to free the polysilicon structures and allow mechanical movement. Table 2-1 outlines the nominal thicknesses of each layer (and some etches) with a graphical representation of the entire process presented in Figure 2-6 [43].

Table 2-2: Nominal thicknesses of PolyMUMPs® layers [43].

Layer	Nominal Thickness (μm)
Nitride	0.6
Poly 0	0.5
First Oxide	2.0
Dimple (etch)	0.75
Poly 1	2.0
Second Oxide	0.75
Poly 2	1.5
Metal	0.5
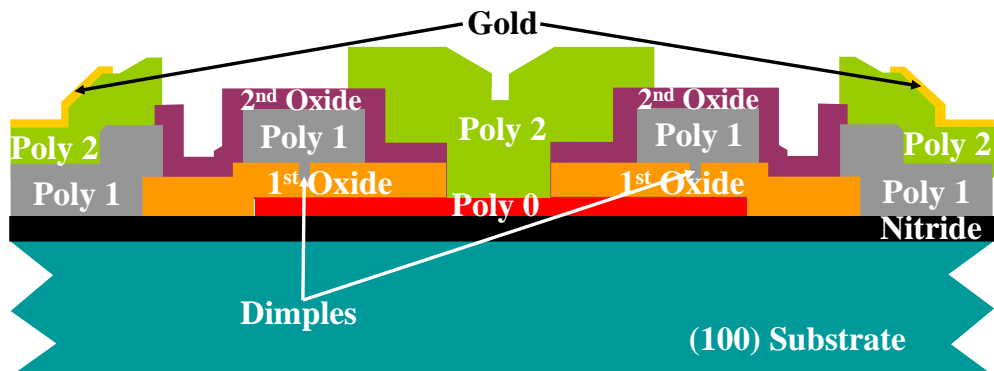
Figure 2-6: PolyMUMPs® graphical layer representation [43].

2.1.2 Conducting Polymers

Similar to devices created in the PolyMUMPs® process, conducting polymers can be formed into actuators. However, polymers are normally considered to be insulators and thus not attractive as a material actuated by principles such as thermal expansion used in traditional polysilicon MEMS devices. The attractiveness of conducting polymers is that they combine the ease of processing, low weight, good mechanical properties and low cost of polymers with many of the electrical properties found in electrical and electronic conductors such as silicon, carbon black and copper [44]. Polymers with desirable barrier properties, such as corrosion resistance, have been available for years, but other properties such as thermal and mechanical stability and near perfect optical transparency have been only seen in a limited fashion in recent years. The fact that the oxidation state of a conducting polymer is accompanied by modifications in electrical conductivity, color, volume, stiffness, etc. has been used in many applications.

One such application, electromechanical actuators, utilizes volume changes during the oxidation/reduction process due to exchange of counter-ions between the polymer and electrolyte used as a dopant [45]. These volume changes (and strain) can be used for electromechanical actuation. This of conducting polymers is of most interest to this research, as conducting polymer actuators utilize an ion transport mechanism, which similar to PECT actuators is an electrochemical process.

2.1.3 Conducting Polymer Theory

The theory behind conducting polymers is not that different from that of a typical doped semiconductor. The polymer chain that is created has to have a partially filled outer shell that shares electrons in π and $\pi*$ bonds alternately. These bonds allow the

doping of the device similar to doping of semiconductors. This doping method is also very similar to experiments in graphite fibers, in that the doping process can cause contractive strain when oxidized, and both produce expansive strain when reduced.

It is necessary clarify a difference between the chemists' terminology of conducting polymers and the electrical engineers' terminology. A chemist, when talking about the conducting polymer will explain that, in the case of polyacetylene, there is a partially filled sp^3 band, with alternating bonds that share electrons to form the highest occupied molecular orbital or HOMO. This is the top of the valence band of the conducting polymer and can be used synonymously with the valence band that electrical engineers use to term this state. Additionally, the lowest unoccupied molecular orbital or LUMO is synonymous with the bottom of the conduction band of the device. For simplicity, these phenomena will be referenced using the electrical engineering terms.

Polymers that have delocalized π and $\pi*$ bonds are called conjugated polymers. They can be divided into two groups: those with degenerate ground states such as *trans*-polyacetylene and poly(phenylene methane), and those without degenerate ground states, including most other conducting polymers [46]. The reduction or oxidation process of doping the conducting polymer adds one electron to the polymer chain which causes the injection of states from the top of the valence band or the bottom of the conduction band into the bandgap.

2.1.4   Conducting Polymers as Actuators

In addition to large changes in electrical conductivities when doped, conducting polymers also experience as much as a 10% increase in length and 220% increase in volume upon doping [44]. Similar to the PECT effect in graphitic carbon, strain can be

generated using a voltage potential to either reduce or oxidize the conducting polymer. Although the external input to PECT and conducting polymer actuators are similar, the internal electrochemical mechanisms are different. The changes which occur during the redox process in conducting polymers are suitable for converting electrical energy into mechanical energy, similar to piezoelectrics and polysilicon MEMS devices. Similar to polysilicon devices, the conducting polymers give an increased work capacity at lower voltages than piezoelectrics [44]. Several different micro-scale devices had been fabricated prior to 1991, including micro-tweezers presented in Figure 2-7.
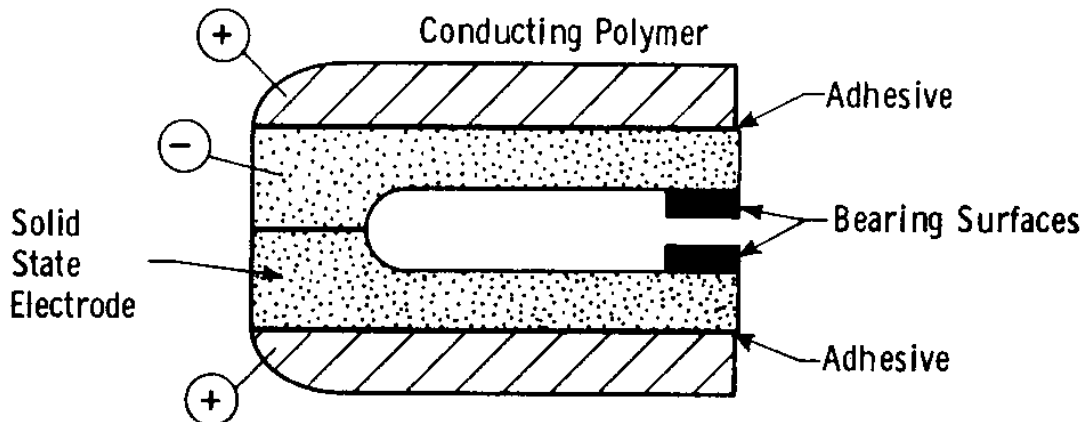
Figure 2-7: Micro-tweezers based on the mechanical expansion occurring during oxidation and reduction doping of a conducting polymer [44].

In this device, two layers of the same conducting polymer are separated by an adhered layer of solid state electrolyte. When a small voltage is applied, the conducting polymer becomes "doped" causing the innermost layer to expand and causing the tweezer to open. Reversing the current direction causes the tweezers to close [44].

A similar device can be fabricated using a bi- or tri-layer structure. A bilayer device can be constructed using a no volume-change film such as polyvinyl chloride

(PVC) adhered to a conducting polymer. In the presence of an electrolytic solution, oxidation causes the conducting polymer to expand and bends the device away from the conducting polymer side. Under reduction, the conducting polymer contracts to provide actuation in the opposite direction. Figure 2-8 illustrates the bi-layer structure produced by Otero and Sansinena in 1998 [45].
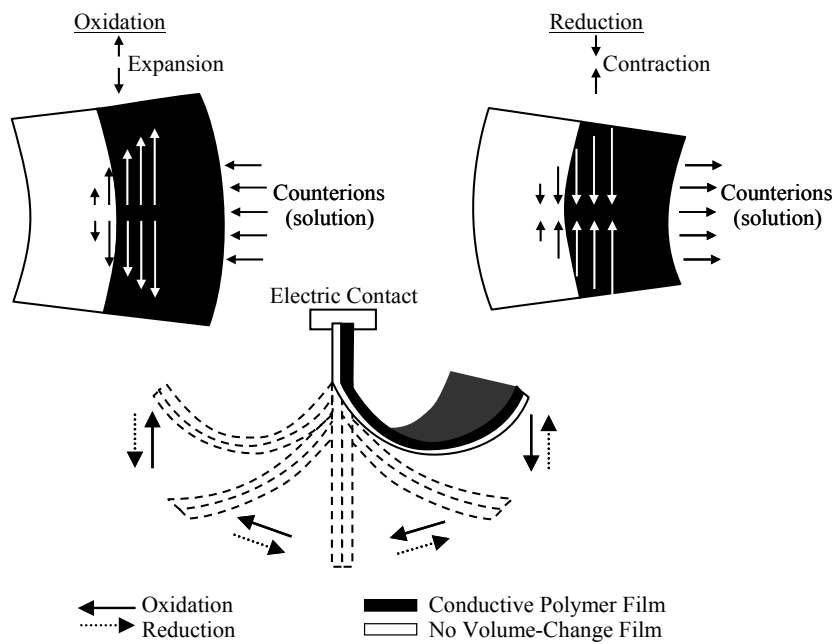
Figure 2-8: Bi-layer conducting polymer actuator capable of bending in both directions [45].

A similar device can be created by adding a second layer of conducting polymer as the auxiliary electrode, allowing for more actuation force of the material. The one drawback of these particular devices is the need to be immersed in an electrolytic solution, which can be solved by making the no volume-change film composed of an electrolytic layer. Such a device has been created by replacing the no volume-change film with a paper film soaked in HCl by the Kyushu Institute of Technology and the

University of Pennsylvania [45]. This allowed the actuator to work for short periods of time in ambient atmosphere as presented in Figure 2-9.
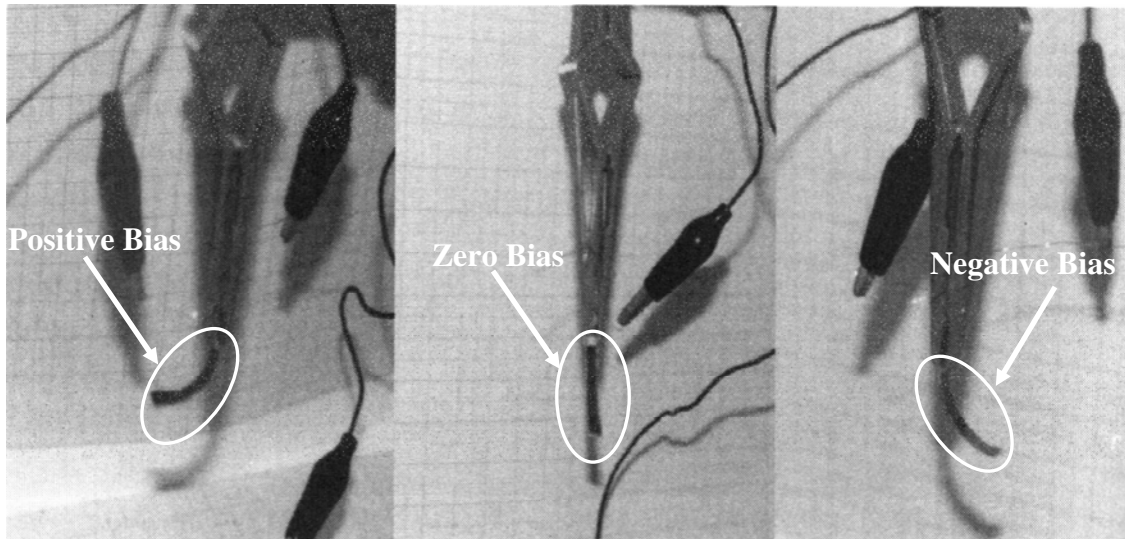
Figure 2-9: Polyaniline conducting polymer actuator with HCl soaked paper in air [45]. (observe tip deflection)

A more robust version of this actuator involves the use of a solid polymer electrolyte as the no volume-change layer in a tri-layer structure which allows more continuous actuation in air. The largest problem of using conducting polymers is the ability to produce linear motion from the device. The devices illustrated all use differential actuation and produce movement normal to the axis of the device, which is not suitable for many applications, including the most promising application of artificial muscles.

Conducting polymer actuators have several advantages and disadvantages. Conducting polymers are both ionic and electronically conductive materials that allow construction of actuators with a mechanism similar to natural muscles. In both cases an electric pulse triggers an electrochemical response and an ionic exchange is responsible

for the maintenance of the electrical neutrality [45]. Theoretically calculated force densities of these devices can achieve up to 450 MPa [45], which is enormous when compared to a human muscle of ~0.5 MPa. Experimentally, conducting polymer actuators have achieved 3 MPa, still an order of magnitude higher than natural muscles [45].

The actuation mechanism of these devices uses ion exchange and as such either requires an electrolytic solution or a polymer electrolyte. The device must encapsulate the conducting polymer material and this limits the uses for the device. If a solid polymer electrolyte is used, the device may not need to be encapsulated, but the material will probably impede performance due to low ionic conductivity [45]. Additionally, a delamination may occur during the actuator's lifetime and has been reported in cases where a conducting polymer film was deposited onto a flexible plastic film sputtered with a thin layer of metal. This is due to the weak contact between the metal and the conducting polymer [45]. Lack of stability due to the ambient atmosphere, which can chemically overoxidize the conducting polymer, causes concern about the degradation of the material over time. Additionally, faradaic processes for conducting polymer actuators involve solid-state dopant diffusion and structural changes that limit rate, cycle life and energy conversion efficiencies [47].

2.1.5   Carbon Nanotube Actuators

Buckytubes, or single-walled nanotubes (SWNT) can be formed into actuators using a similar method of actuation as for PECT graphite. It is possible to create sheets of SWNT which like long-fiber nanotubes are comprised of bundles of SWNTs. Each

bundle containing from 30 to 100 SWNTs with various chirial vectors, or internal geometries, (n,m), from zigzag (n,0) to armchair (n,n) tubes [48].

Physically, SWNT sheet actuators consist of a macroscopic sheet made of billions of SWNTs, often called "Buckypaper". This can be obtained by suspending SWNTs in a solution and vacuum filtering the solution onto a filter such as poly(tetraflourethylene) which has a pore size ≈ 0.45 μm [49]. Following filtration, the new material can be rinsed and dried and the resulting nanotube bundle mat can be peeled from the filter. These nanotube papers can be tens of micrometers in thickness. Nanotube bundles are joined by mechanical entanglement and van der Waals forces along incidental points and lines of contact [47]. Figure 2-10 presents an electron micrograph of the Buckypaper surface and shows that it is composed of randomly entangled structures.
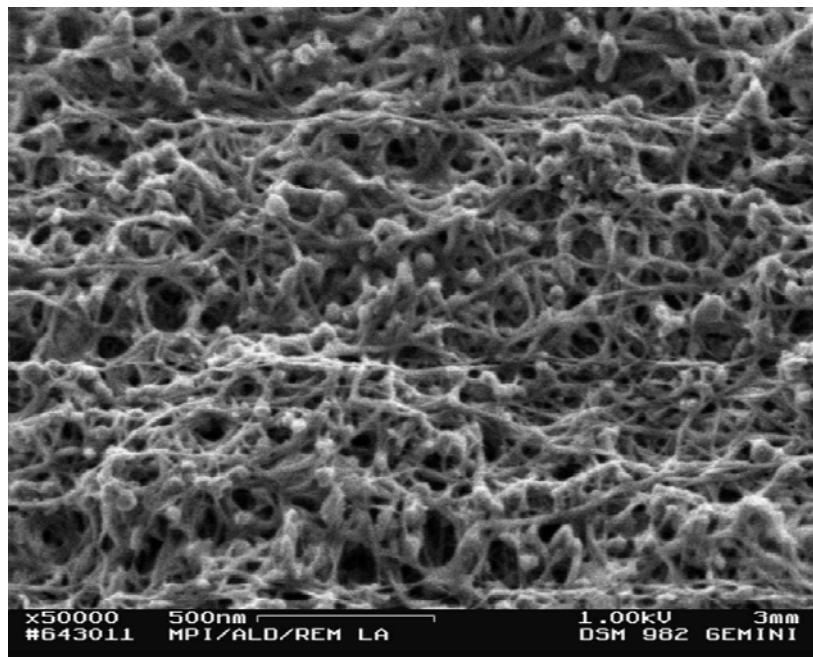
Figure 2-10: Scanning electron micrograph of Buckypaper surface showing entangled ropes forming the SWNT paper [49].

Each rope-like structure is composed of several hundred nanotubes bundled together into ropes. The ball-like grains, which do not hinder activation, are formed by encapsulated catalyst impurities coming from the synthesis process of SWNTs [49]. The mechanical properties of the paper result from the previously mentioned van der Waals forces and mechanical entanglement. The elastic modulus of Buckypaper of 1 to 2 GPa is much less than that for a single SWNT, graphitized carbon fiber or HOPG. At room temperature, this paper made of random amounts of metallic and semi-conducting SWNTs has a conductivity of 500 – 1000 S/cm [49].

Similar to the PECT effect, SWNT electrodes can be injected with electronic charge, compensated at the nanotube-electrolyte interface by electrolyte ions, but without a dopant intercalation interaction [47]. SWNT actuators use dimensional changes in the covalent bond directions caused by the low-level charge injection. These changes originate from the quantum chemical and double-layer electrostatic effects [47] and changes in band structure [49]. Like PECT graphite, this results in expansion when electrons are injected and contraction when holes are injected. In the case of high-density charge injection of either sign, however, expansion results from both quantum mechanical effects and electrostatic double layer charging [49].

These papers can be bonded together using sheets of Buckypaper on either side of a piece of double-sided adhesive tape and immersed in a solution of 1 M NaCl [47,49]. When a DC potential of a few volts or less was applied, a deflection of up to a centimeter can be observed at the tip of the cantilever, which can be reversed on reversal of the potential [47,49].

Figure 2-11 presents the operation of a buckypaper bimorph cantilever. The actuator is labeled bimorph because the response of the actuator depends on the difference in the electrically induced expansion of opposite actuator electrodes. In order to more accurately measure the movement of the bimorph cantilever, Baughman *et al.* adhered two pieces of Buckypaper to a piece of poly(vinylchloride) or PVC film that was 215 μm thick using double-sided adhesive tape [47]. The lower end of the Buckypaper was immersed in the NaCl solution and anchored at the bottom of the test fixture with contacts leading to both sides of the paper. The PVC strip had a sputtered gold mirror at the other end, and the displacement of this mirror was measured with an optical sensor [47].

Longitudinal strain produced by a NaCl Buckypaper actuator can be determined by a test setup similar to that presented in Figure 2-12. Response of this actuator was linear at lower voltages, between -0.4 and 0.1 V, but at higher voltages increased hysteresis and non-linearity prevailed. Resonance of this actuator peaked at $\approx$ 25 Hz when driven with a 2 V peak to peak alternating current voltage [47]. Figure 2-13 presents the measured values for cantilever displacement with the test setup presented in Figure 2-12. These measurements place the potential range as symmetric about 0 V, referenced to a saturated calomel electrode (SCE)—an electrode of mercury topped by mercury chloride paste, a standard electrode used as reference in cyclic voltammetry—at a scan rate of 50 mV/s.
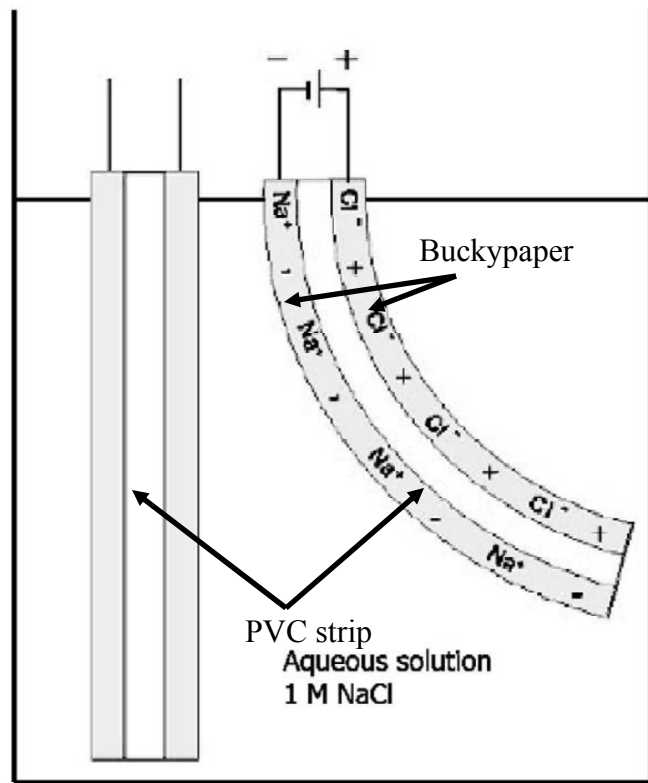
Figure 2-11: Schematic edge-view of a bimorph SWNT actuator operating in 1 M aqueous NaCl [47,49].
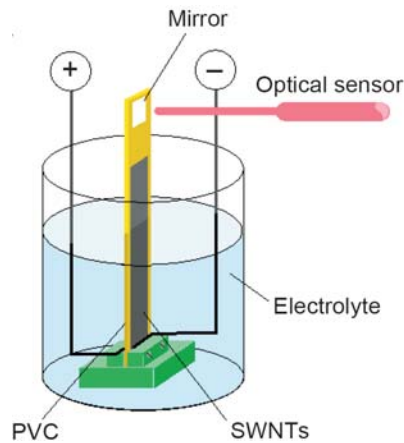
Figure 2-12: Apparatus used to characterize electrochemical bimorph actuator consisting of Buckypaper on either side of a PVC film [47].
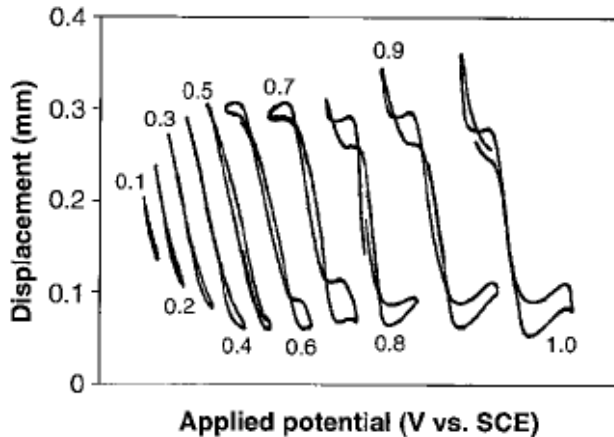
Figure 2-13: Measured cantilever displacement versus electrode potential in 1 M NaCl [47]

Since the response of a bimorph cantilever depends on the difference in the electrically-induced expansion of opposite Buckypaper electrodes, a second test setup was developed to directly measure the strain of the actuators. Figure 2-14 presents the test fixture used to directly test the strain induced on the Buckypaper sheet in 1 M NaCl. The results were compiled showing as much as 0.04% strain at a voltage of 0.9 V. These measurements are presented in Figure 2-15. It is important to note that the strain on these devices at very low frequencies is significantly degraded as frequency is increased, because the device depends on a transport limited reaction to actuate. In order to achieve $\approx$ 0.065% strain, the frequency needs to be less than 0.063 Hz, and strain degrades quickly to 0.015% at 4 Hz. A conventional joule-heated polysilicon actuator can achieve 0.04% at this voltage, and is just beginning to acutate, capable of performing this operation at several kHz. The low strain of this combination of solution and actuation material at 4 Hz limits usefulness to very low frequency applications, possibly in such devices as artifical muscles.

47
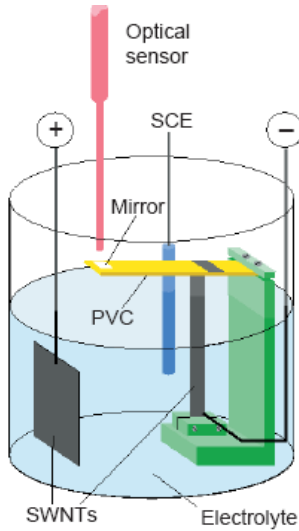
Figure 2-14: Test fixture to directly test change in length of a Buckypaper actuator in 1 M NaCl [47].
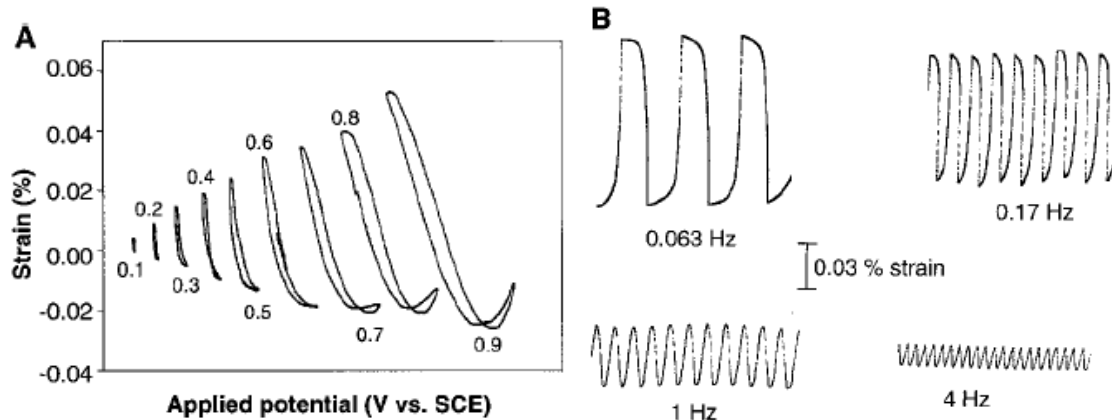
Figure 2-15: (A) Strain measured for Buckypaper sheet versus applied potential. (B) Time dependence of strain in a nanotube sheet for an applied square wave at ±0.5 V at the indicated frequencies [47]

Further work has shown that the chiral vector of the SWNTs impact the amount of strain possible in a bundle. Improved synthetic methods are expected to eventually make it possible to make bundles of SWNTs of selected types for use in actuators [48]. As such, researchers investigating nearest neighbor hopping and energy injected per carbon

atom, in the linear mode derived equations to characterize the longitudinal and radial strain induced on a bundle of SWNTs.

Longitudinal and radial strain induced in a bundle of SWNTs oscillates based upon the SWNT chirality as a function n – m [48]. This derived oscillatory dependence of actuator strain is consistent with the picture of the bandgap modulation described for deformed nanotubes [48]. The oscillatory nature of changes in length and diameter depending on chirality is shown for a constant electron doping level and is presented in Figure 2-16. In graphite, charge injection leads to isotropic expansion/contraction of the lattice [48]. For a bundle of nanotubes of various geometries, experiments show some average, with larger strains from semiconducting SWNTs compensating each other as seen in Figure 2-15. Separation of semiconducting nanotubes of the optimal type is therefore required to make the predicted enhancement practically useful [48].
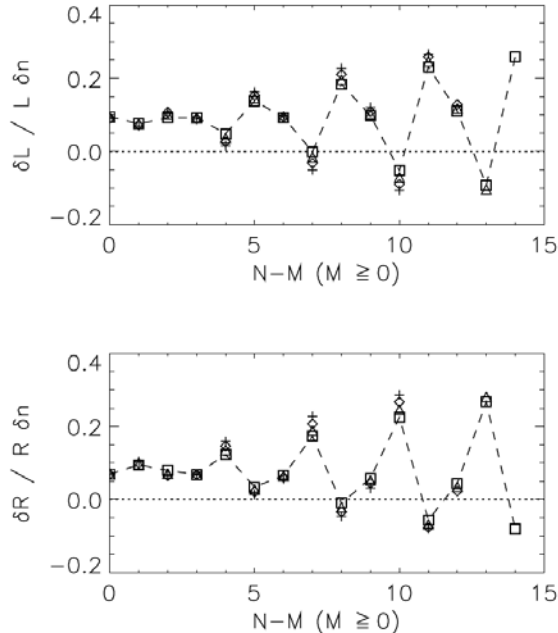
Figure 2-16: Reduced dimensional distortions for families of carbon nanotubes with n = 11 (crosses), 12 (diamonds), 13 (triangles), and 14 (squares). Upper panel shows changes in nanotube length, and the lower changes in nanotube radius [48].

2.1.6 Graphite Actuators Orthogonal to the basal plane

Chung and Wong investigated the interesting phenomenon of the reversible expansion of bromine intercalated graphite. This particular graphite intercalation compound, when heated expands in a direction parallel to the c-axis up to 4500%, generating an equivalent stress of up to 3 MPa [33,34]. This phenomenon is attributed to the heating of the sample which causes extreme expansion of the intercalant molecules at 100 ºC in the case of graphite intercalated with bromine [50]. A sample of bromine-residue intercalated HOPG, $4.2 \times 3.3 \times 1.0$ mm, containing 1.9% Br_2 was used in experiments on reversible exfoliation. The sample was mounted using a Michelson interferometer in which a moveable lightweight mirror was mounted on the HOPG sample and the second mirror remained stationary [51].

Results from this experiment suggest that only the surface layers of graphite were heated enough to expand the bromine intercalant and cause the expansion of the HOPG sample in the c-axis due to the increased stress on the interplanar van der Waals forces. Only the limited depth of the sample near the irradiated surface expanded, since the expansion was less than 5 μm. Expansion varied between each ~ 8 minute cycle ranging from 4.5 μm to just under 2 μm of expansion [51]. Chung et al. also concluded that this heating did not affect the basal plane dimensions of the sample during expansion along the c-axis, and that the optomechanical actuation effect is different from the related electromechanical effect utilizing joule heating in the same material [33,34,51].

As intercalant molecules are intercalated into the graphite structure, they push adjacent planes of graphite apart, increasing the interplanar distance until all galleries are filled with intercalant in stage 1 intercalation. The size of the molecules determine the

amount of change in c-axis spacing, and thus the total strain produced in the c-axis direction. Figure 2-17 illustrates the expansion of the gallery spacings of a piece of graphite at stage 4 intercalation. It emphasizes the oxidation reaction, which presents oxidized bisulfate only rather than the entire redox system which was presented in Equation 1-1 previously, containing H_2SO_4 molecules as well as oxidized bisulfate.
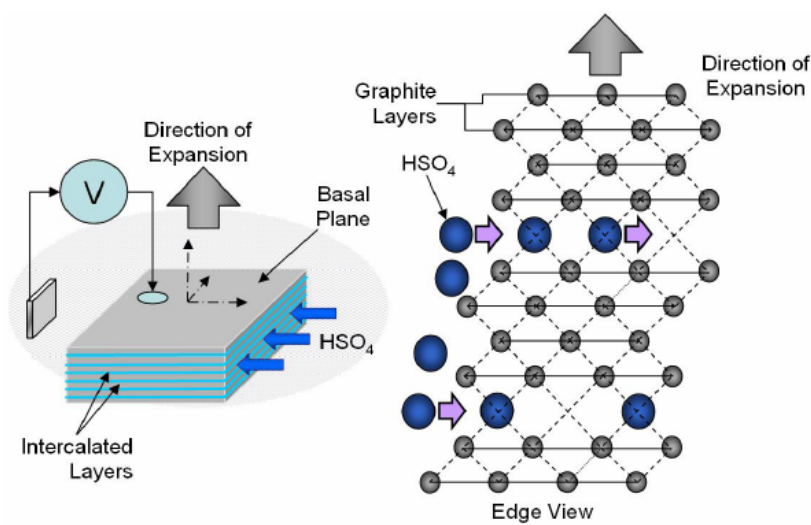
Figure 2-17: Expansion illustration during sulfuric acid intercalation (stage 4) in graphite [22].

Further experiments characterizing orthogonal expansion were performed by scientists at HRL Laboratories, LLC, determining the c-axis actuation potential of HOPG samples intercalated with 18M sulfuric acid. The experiments consisted of a 1 mm thick sample of HOPG [22] and a 1.2 mm stack of Toray graphite paper [23] captured between a platinum foil anode and a ceramic anvil. The anvil and sample were aligned and held in a ceramic beaker according to the test fixture presented in Figure 2-18.

In these experiments, loads were applied to the sample to determine the energy density of the electrochemical effect at specified loads, from 0 to 8 MPa for the HOPG sample and 0 to 1.5 MPa for the Toray graphite paper. Results of these experiments

showed several inflection points characteristic of staging and a maximum measured volumetric expansion of 140% for sulfuric acid intercalation. In HOPG intercalation testing, only loads of 0 and 2 MPa reached full intercalation (more than one bisulfate ion for every 24 carbon atoms, or $>C_{24}HSO_4$) without fracture, with significantly less strain at higher loads [22,23]. Results from these tests are presented in Figure 2-19 and Figure 2-20.

Testing the Toray graphite paper at elevated temperatures ranging from 22 to 55 ºC, with potentials from 0.4 to 1.3 V shows that strain rate is extremely sensitive to changes in temperature, with the rate increasing as temperature rises. Massey suggests that for high temperature c-axis actuation, graphite intercalation compounds will have optimal strain rates. The temperature capability of graphite intercalation compounds will be limited by the thermodynamic stability of the intercalant, which will allow for much higher temperatures in non-aqueous or alkali-metal based systems [23].
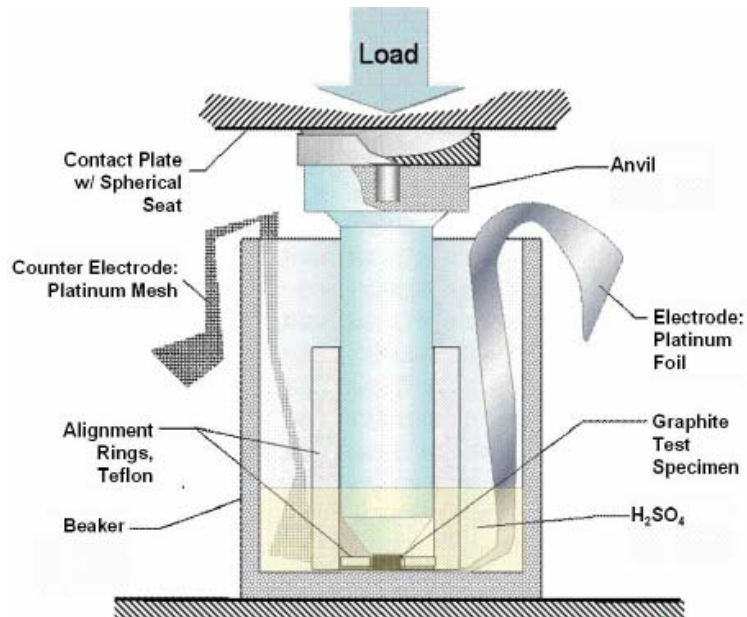
Figure 2-18: Test Fixture used to test Toray graphite paper and HOPG sample for c-axis expansion [22,23].

52
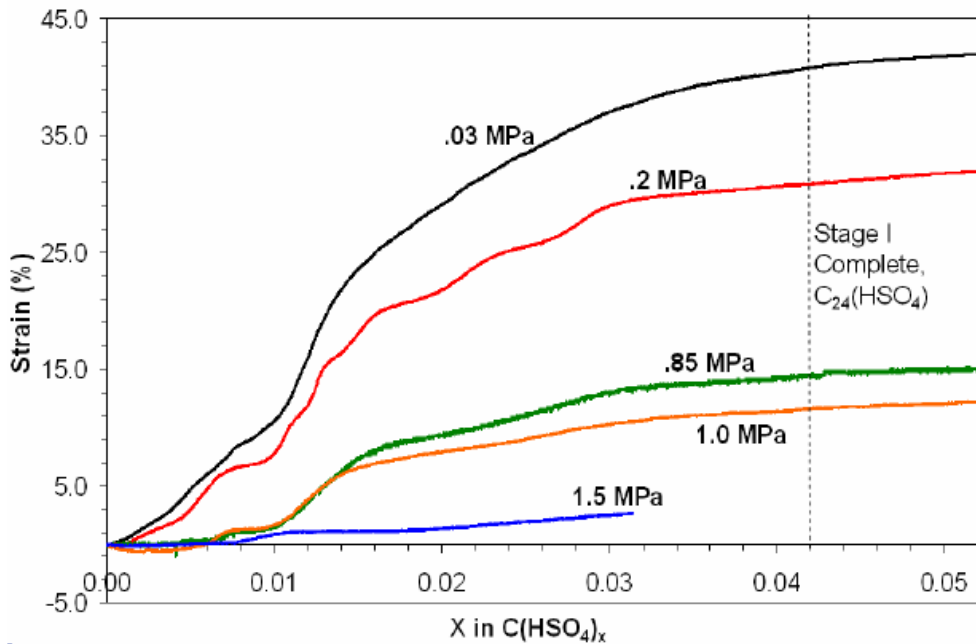
Figure 2-19: Intercalation of sulfuric acid into Toray carbon paper at 1.5 mA constant current with constant orthogonal compressive loads from 0 to 1.5 MPa. The dotted line represents a pure graphite system that is fully intercalated [23].
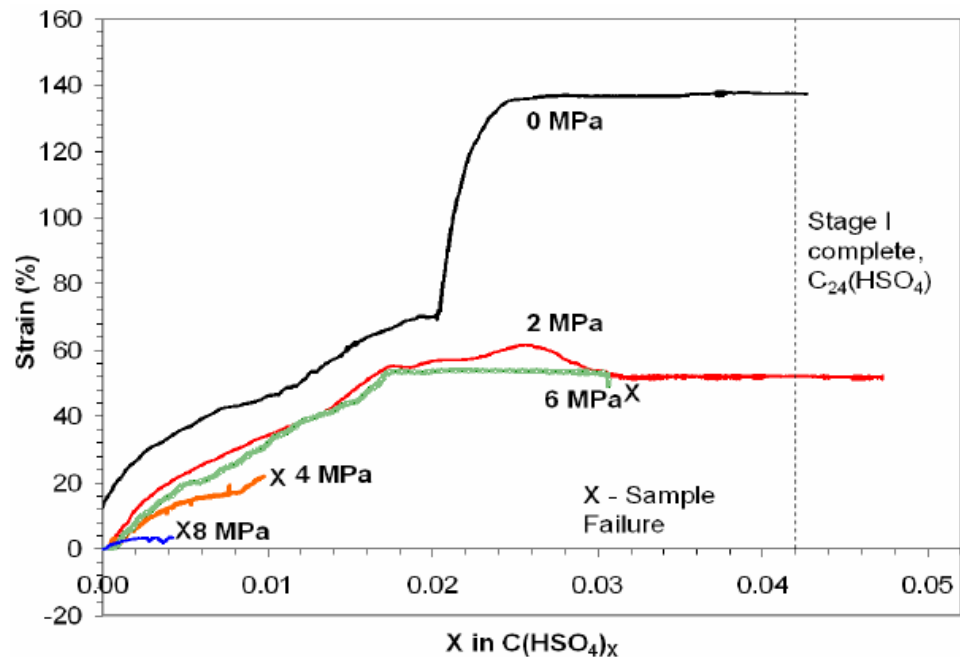
Figure 2-20: Intercalation of sulfuric acid into HOPG at 0.78 mA constant current with constant orthogonal compressive loads from 0 to 8 MPa. The dotted line represents a pure graphite system that is fully intercalated [23].

53

2.2 Summary

This Chapter discussed mechanisms and materials that are similar to the PECT effect in an H_2SO_4-graphite intercalation compound. It began with a description of MEMS structures in general and the specific PolyMUMPs® process that is used to create the mechanical structures for the research in this dissertation.

Conducting polymer actuators, achieving up to 10% strain depending on doping were presented. Carbon nanotube actuators, in an aqueous NaCl electrolytic solution were addressed, producing up to 0.065% strain at 0.9 V of potential voltage were also discussed. Finally, carbon nanotube paper and HOPG actuators that act orthogonal to the basal plane were presented which, upon exfoliation under heating conditions, could achieve up to 4500% strain, with typical results between 45 and 130 % for HOPG loaded at up to 6 MPa of compression.

Chapter 3 of this dissertation will detail initial experimental results obtained from testing Thornell P-100 carbon fibers in sulfuric acid to determine longitudinal strain along the basal plane within the graphite fibers. It will also detail initial electrical measurements taken for a 1 cm length of Thornell P-100 carbon fiber.

PIEZO-ELECTROCHEMICAL TRANSDUCER EFFECT (PECT)

MICRO-ELECTROMECHANICAL ACTUATORS

3. Macro-scale Experimentation

Theory, as expected from the Air Force Research Laboratory (AFRL) proposal on graphite actuators, suggests a maximum strain possible of ~2% in the basal plane of graphite. To verify that test samples were representative of the population, and to gain some insight on the electrical characteristics of intercalated graphite, electrical experiments were prepared that would accomplish these tasks. AFRL Materials Directorate (ML) designed a test setup to perform initial testing on the strain relationship of intercalated graphite. The author then used the test setup to conduct initial strain and conductivity measurements on an intercalated graphite-H_2SO_4 fiber system. Based upon these initial tests, additional tests were designed and accomplished during the course of this dissertation to create micro-actuators using the phenomena described in Chapters 1 and 2 of this document.

3.1 Electrical Experiments

Macro-scale electrical experiments measured inductance, capacitance, and resistance. Testing was accomplished using intercalation voltages from 0 to 1.4 V in 0.1 V increments, at frequencies from 40 Hz to 1 MHz to determine the conductivity of H_2SO_4 intercalated P-100 test fibers used in these experiments.

3.1.1 Experimental test setup

The test setup consisted of an Agilent 4284A precision LCR meter for measurements and an Agilent 6624 DC power supply to provide the voltage potential to

the system. 2 cm of Thornel P-100 carbon fiber (acting as an anode in the redox reaction) and a platinum cathode were suspended between LCR meter electrodes on the test fixture and were submerged in a droplet of 98%, covering approximately one half of the length of the fiber. The entire fixture, presented in Figure 3-1, was then surrounded in a nitrogen atmosphere to prevent water uptake due to the hygroscopic nature of H_2SO_4. Both the power supply and LCR meter were connected to and controlled by a computer hosting VEE control software via IEE-488 general purpose interface bus (GPIB).

To observe the physical connections to the fiber and acid, a photograph of the test fixture was taken during the course of the experiments and is presented in Figure 3-2. A scanning electron micrograph of the thornell P-100 fiber prior to intercalation is presented in Figure 3-3. No reference electrode was implemented in this test for three reasons. The first is that characterization of these actuators needed to be performed with the intent to create viable commercial actuators, which would generally not use a reference electrode. The second is that a reference electrode, such as an SCE was not used to make the actuator a representative engineering model. Finally, the experiments used a constant voltage source vice a voltage rate, as is used in cyclic voltammetry. Therefore, to ensure the greatest homogeneity of data between the macro- and micro-scale experiments, it was necessary to omit the use of a reference electrode.

Agilent 4284A Precision LCR Meter

1.234m LS
1.234k RS

−
+

Agilent 6624A DC Power Supply

+

0.10V DC

98% H$_2$SO$_4$ droplet

N$_2$

GPIB Controller to VEE Software
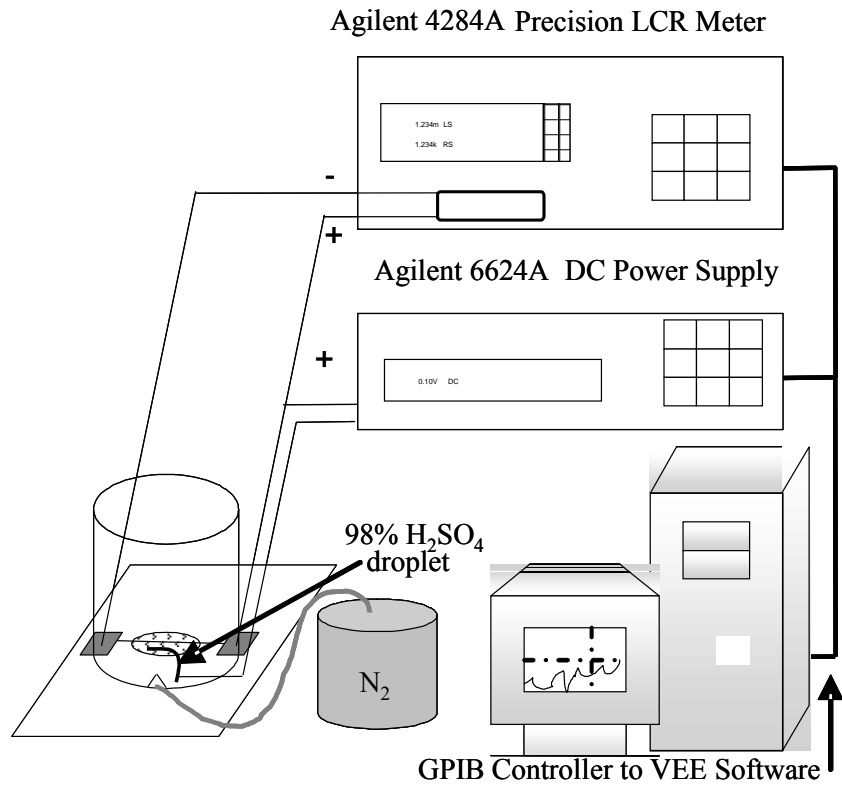
Figure 3-1: Experimental setup to measure conductivity on Thornell P-100 Carbon Fiber.

Pt Cathode

Contacts

P-100 Graphite Fiber

Sulfuric Acid/ H$^+$ Bubbles
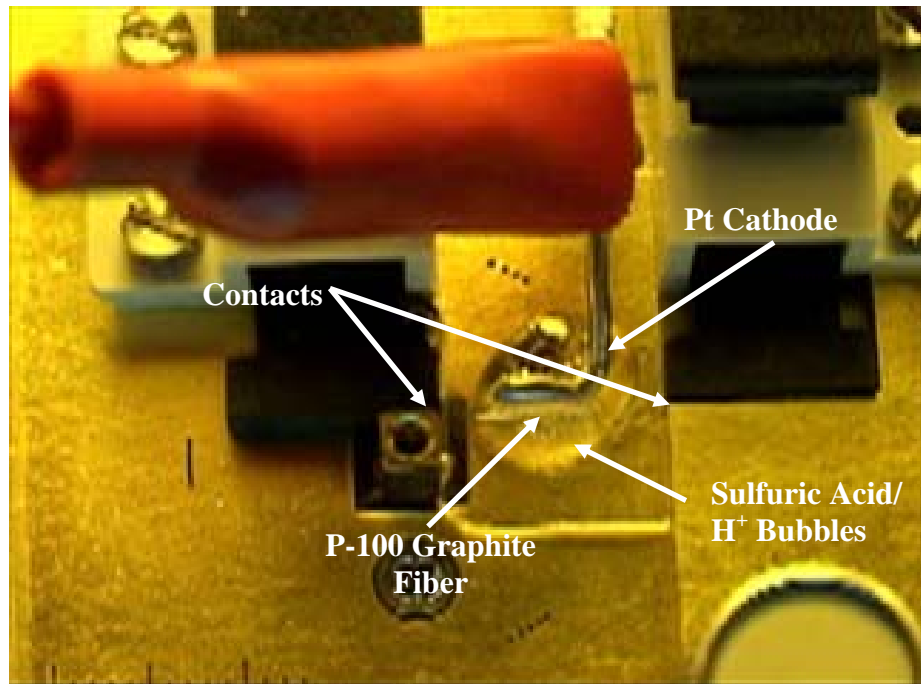
Figure 3-2: Electrical test setup during electrolysis of a P-100 graphite fiber in H$_2$SO$_4$.
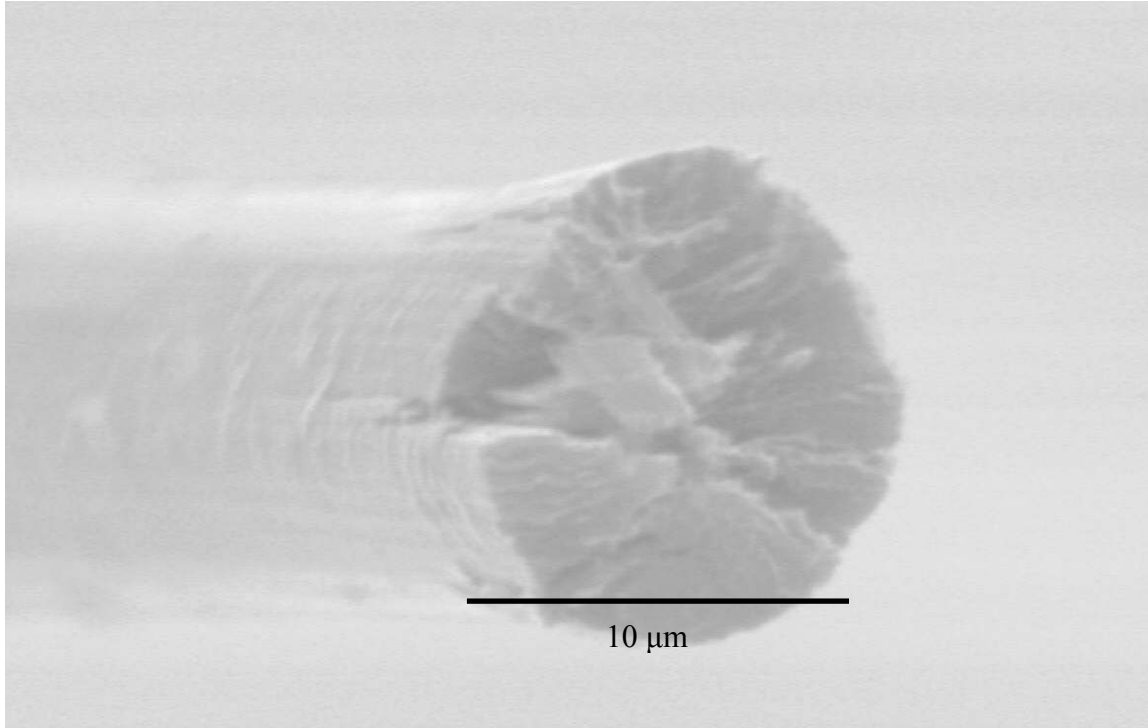
Figure 3-3: Scanning Electron Micrograph of Thornell P-100 graphite test fiber used in all initial experiments.

3.1.2   Experimental results

Testing was accomplished in 0.05 V increments, noting applied bias and measured resistances.   Results from initial electrical experiments confirm that at approximately 0.4 V of applied bias, the resistance of the carbon fiber suspended in H_2SO_4 begins to decrease as intercalation voltages increase, and continue decreasing to 1.2 V of electrolysis voltage.   Resistances are stable from 40 Hz to approximately 10 KHz, where the resistances begin to increase proportional to the input frequency.   A sample of the data obtained from initial electrical characterization measurements is presented in Figure 3-4.   These results confirm that intercalation causes a change in resistance in intercalated P-100 carbon.

58
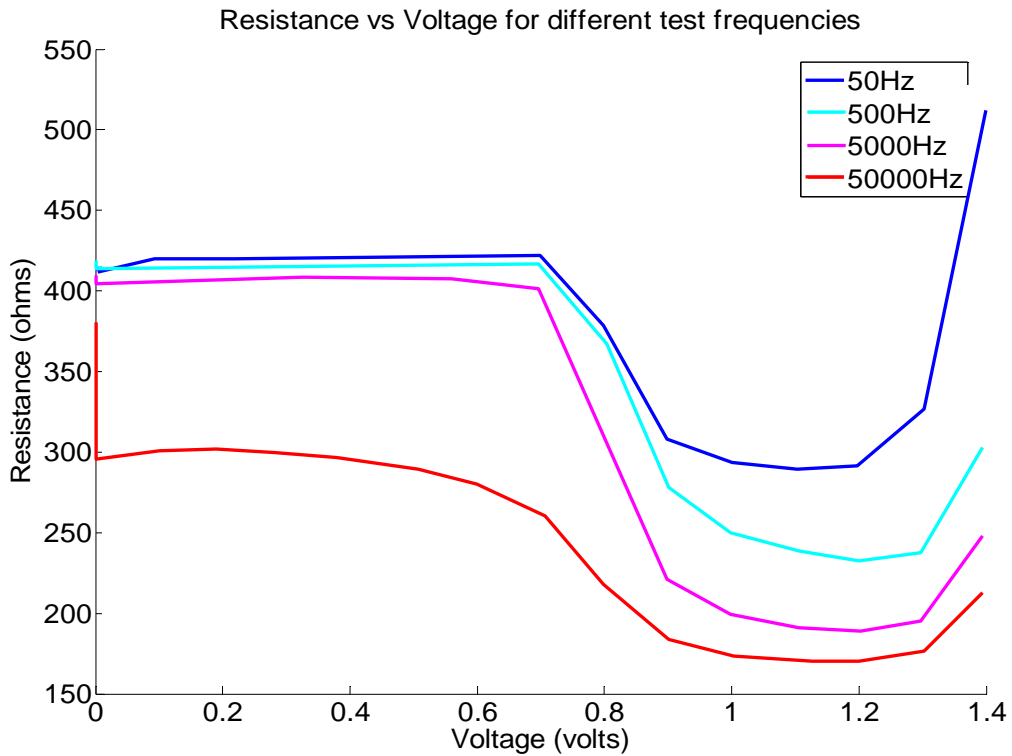
Figure 3-4: Sample electrical characterization data for 50 Hz to 50 kHz signals.

It is notable that these experiments only contain a portion of the P-100 fiber inside and intercalated with the sulfuric acid. Since some of the fiber is exposed, the resistivity of the fiber, approximately 1.6×10^{-4} Ω-cm, is relatively unchanged for the portion of the fiber that is not immersed in the acid. This assumes that intercalation perfectly continues in the bulk staging value for the entire length that is submerged and that none of the non-submerged fiber is intercalated. Realistically, there is probably higher staging near the edges of the acid both inside and outside of the droplet. If 75% of the fiber was intercalated, the remaining portion would account for over 100 Ω of the resistance at higher intercalation voltages. Since the staging at the edges is unknown, a better way to determine resistance must be accomplished to obtain the highest precision for these experiments.

3.2 Mechanical experiments

Initial mechanical experiments were performed to verify that intercalated graphite fibers indeed produced strain during electrolytic oxidation in H_2SO_4. The goal of these experiments was to measure the strain induced on the graphite fiber at different electrolysis voltages.

3.2.1   Experimental test setup

Mechanical experiments consisted of a 62.5 mm Thornell P-100 carbon fiber attached to a load cell and a 793.6 nm resolution stepper motor, with 32.5 mm of fiber suspended in 98% H_2SO_4 contained in a Teflon bath, as presented in Figure 3-5. In order to contact the fiber to the test equipment leads, platinum wires were connected via colloidal silver mixture to contact to each end of the carbon fiber. Once the silver was dried, and it was determined that the silver had provided electrical contacts, the exposed silver was covered with a Teflon™ epoxy to protect the contact and mechanically bond the carbon fiber to the test structure. A platinum electrode was placed into the bath of H_2SO_4 and connected a voltage source between the carbon fiber anode and a platinum cathode to provide electrolysis voltage. A source meter was also placed across the carbon fiber to monitor changes in resistance.
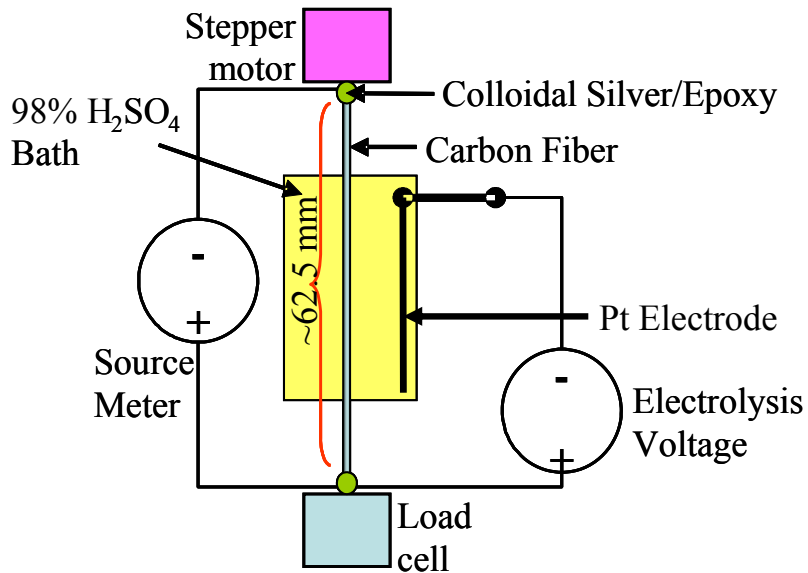
Figure 3-5: Mechanical test fixture used to monitor strain induced in sulfuric acid electrochemically intercalated Thornell P-100 graphite fiber.

Once the mechanical and conductive connections were dry, the load cell was calibrated and the fiber pre-tensioned to be in the linear region of the stress-strain curve for the carbon fiber, at a tension of 1.23 g. Once pre-tensioning was complete, the Teflon bath was filled with 5 ml of 98% H_2SO_4 solution, enough to cover the carbon fiber and platinum cathode (with an electrode potential of ~0 V), and allowed the test setup to stabilize. After the test setup was given time to equilibrate, the load cell and stepper motor location were set to zero and electrolysis voltages were applied. Tests used a 0.05 V step with a 2 minute dwell per step. Once the threshold for intercalation was met, at approximately 0.4 V, the load cell started registering positive strain. At 0.6 V, it was apparent that the drift of the load cell, most likely due to changes in laboratory temperature and airflow fluctuations as people entered and left the room, was becoming problematic. Thus, at the end of each increment, it was necessary to find the zero stress point of the fiber and re-tension in order to remove any bias from the data. The zero

61

points were used to determine total strain at each voltage. Beyond the 1.1 V point, testing changed to perform several iterations of ± 1.4 V potential to quickly intercalate and deintercalate the fiber and monitor the strain relationship.

3.2.2   Experimental results

The strain measured from the differences between zero-point calibration for each test condition from 0.6 V to 1.1 V is presented in Table 3-1. It is evident that, at 1.1 V, it is possible for the PECT effect to produce a strain of roughly 0.5% (calculated from the length change of the immersed 32.5 mm only). The average current throughout the experiment was 6.5 µA. At 1.1 volts, the average current was 8.25 µA yielding an instantaneous power dissipation of 9.09 µW at the highest experimental electrolysis voltage applied. Maximum load measured during experiments was 3 grams.

Table 3-1: Bias-removed strain data for PECT intercalated graphite fiber from 0.6 to 1.1 volts electrolysis voltage.

Actuation Voltage (V)	% Strain
0.6	0.0469
0.65	0.0746
0.7	0.0974
0.75	0.1447
0.8	0.1797
0.85	0.2387
0.9	0.3077
0.95	0.348
1	0.4102
1.05	0.4641
1.1	0.5506

Several limitations are apparent in this experiment, most notably, the lack of complete immersion in the sulfuric acid intercalant. Thus, it is uncertain how much of the fiber actually reached stage 1 intercalation, or if the portion that was intercalated was

completely contained in the length of the sulfuric acid bath. Further experiments will require completely submersed fibers to more accurately test the planar distortions in graphite leading to positive strain in the graphite fibers.

3.3 Macro-scale limitations

Testing PECT devices at the macro scale has one, very large, inherent problem associated with the required test setupd. The problem arises from a physical limitation on the percentage of fiber which can be immersed in the intercalant. This limits the active portion of the fiber and causes uncertainty to creep into the results since it is impossible to determine the partial intercalation effects in the fiber at the intercalant-air boundary.

To remove this uncertainty, it is necessary to devise a testing solution that can evaluate the PECT effect in a completely enclosed environment, where that intercalant-air interface no longer exists. Removing this interface can be easily demonstrated by creating a micro-actuator system combining a PolyMUMPs die with thin layers of HOPG or graphite fibers.

3.4 Summary

This Chapter discussed the macro-scale experiments performed on single strands of P-100 fiber, with only a portion of the fiber in the intercalant solution of H_2SO_4. Preliminary data was collected on the electrical and mechanical characteristics to determine if the PECT effect was worth investigating. This macro-scale research confirmed that the PECT effect induces significant strain in a graphite fiber. It also verifies that the resistance of a PECT fiber decreases, and that both effects occur upon application of increased electrolysis voltages. This chapter concluded that micro-scale experiments are necessary to ensure 100 percent confidence that the entire fiber is

contributing to the data for mechanical and electrical characterization. Chapter 4 presents further research into the PECT effect with carbon fibers and characterizes the strain that these fibers induce at a micrometer scale. Data will be presented detailing the behavior of PECT fibers under loading conditions.

PIEZO-ELECTROCHEMICAL TRANSDUCER EFFECT (PECT)

INTERCALATED GRAPHITE MICRO-ELECTROMECHANICAL

ACTUATORS

4. PECT Micro-Actuator Research on Carbon Fibers

Research into the PECT effect, as evidenced in the literature, is limited to the study of some very special cases of intercalated graphite. The purpose of PECT micro-actuator research is to quantify the beneficial characteristics of PECT based a-plane graphitic contraction, and to demonstrate merit as an actuation material. micro-actuator systems using Cytec Thornell® P-100 graphite fibers that were detreated and attached to PolyMUMPs® mechanical structures.   These structures allow for the direct measurement of strain produced by PECT actuators at the micrometer scale and the calculation of both stress and reaction force based on the resistance of the polysilicon portion of the actuator system.

4.1 Mechanical

Macro-scale experimental results have shown a strain in intercalated graphite fibers approximately one order of magnitude worse than theoretical maximum strain of 2% [2]. These results are nonetheless better than piezoelectric PZT and polysilicon thermal actuation mechanisms at similar voltages and power. The amount of error may be attributed to the amount of the fiber that is intercalated in the process. To ensure the best accuracy and remove this variable from inducing error into test results, it was necessary to completely immerse the graphite fiber, and thus the entire actuator system, in the intercalant. This method of test ensures that the fiber is intercalated along its entire

length and reduces total uncertainty in the test results. Testing with an integrated PolyMUMPs® mechanical structure also allows the strain to be measured and the resultant forces to be calculated for the PECT effect in intercalated carbon fibers. Mechanical testing can also be used to determine the response time of the mechanical effect to further characterize this phenomenon for use in MEMS structures as an actuation mechanism. Additionally, these structures can be tested with more benign electrolytic solutions that are more likely to be accepted as aqueous intercalant species than the corrosive sulfuric acid.

In order to develop mechanical structures that may be integrated with carbon fibers in a micro-actuator system, some basic research was completed. Chapter 2 detailed the current state of graphite intercalation compounds used as actuators, and other similar materials used to the same end. This research is intended to lay the foundation for success in the evaluation of PECT graphite as an actuation material. The polysilicon mechanical structures designed to test these characteristics are analyzed in detail in the following sections of this dissertation.

4.1.1   First Generation Mechanical Structures

First generation mechanical structures were fabricated using the PolyMUMPs® fabrication process. This device is intended to allow a fully immersed test structure to measure the force and displacement of a series of carbon fibers in sulfuric acid solution. To determine the usefulness of this structure, the structure was analyzed to determine the restoring force it could provide, analyzed the breaking point of the device (to ensure adequacy as a test structure), and determined the strain from deflection of the device.

Figure 4-1 presents the device that was fabricated in PolyMUMPs® run 66, with different total flexure lengths of 350, 400 and 450 μm.
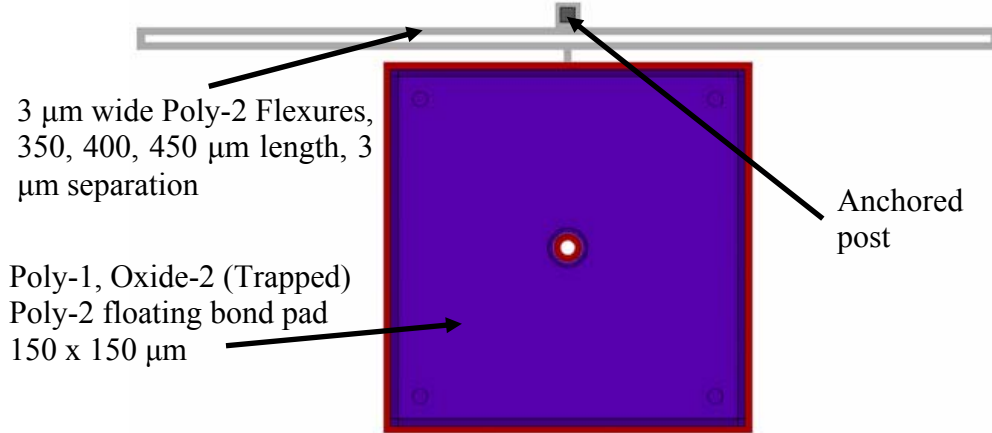
Figure 4-1: 150 μm square floating bond pad used to optically measure deflection and calculate strain induced in a PECT graphite fiber.

4.1.1.1   *Back of the Envelope Calculations*

Rather than analyzing the whole structure, it is only necessary to create a model for the flexures themselves. The trapped oxide bond pad only serves as an anchor point for the carbon fiber in this experimental setup. Neglecting the floating bond pad, one can reduce the model to flexures with a rigid boundary condition as presented in Figure 4-2.
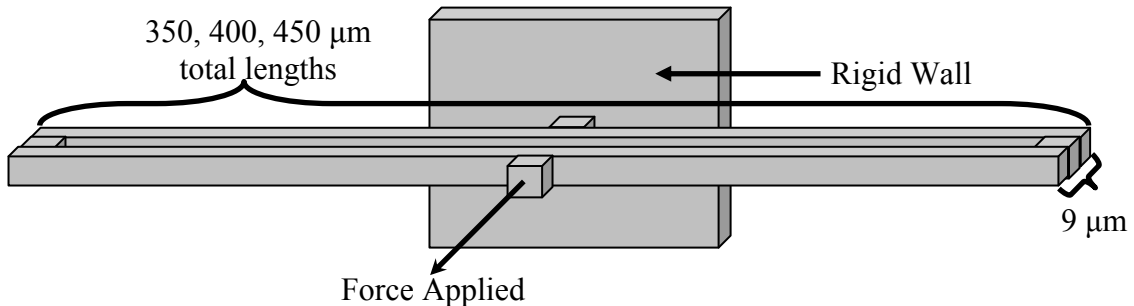
Figure 4-2: Modeled elements of double flexure test structure.

Separating elements to model this structure as a fixed-fixed beam, one can assume that the connections at the end of the flexures are in effect rigid. This is a minor oversimplification since the ends will compress toward one another somewhat and bend a little, but the assumption is good enough to achieve a rough calculation of the forces on the structure. Another assumption is that force is applied evenly to both beams, such that there is only half of that force acting on each beam. The reduced beam structure is 9 μm shorter when you take out the flexure applying force and the two fixed pieces at the end of the flexure. This simple analysis calculates values for a 350 μm long structure with an equivalent length l of 341 μm. This allows us to model the structure as a fixed-fixed beam, with a center load applied as presented in Figure 4-3.

The maximum deflection of this fixed-fixed beam can be given in metric units by:

$$y_{max} = -\frac{Fl^3}{192EI} \ (m),$$ (3.1)

which can be found in any number of mechanical engineering textbooks *e.g.* Engineering Mechanics" by Wirsching, Murdock and Washburn. The maximum displacement (y_{max}) in meters is dependent upon the force (F) in Newtons applied to the center of the beam, which in the case of an assembled actuator is induced by the contraction of the intercalated carbon fiber in the y-direction. Maximum displacement also depends upon the physical characteristics of the beam and is defined by the length (l) of the beam, the moment of inertia (I) and Young's Modulus (E).

The moment of inertia can be defined in terms of the cross-sectional dimension of the base (b) and height (h) of the polysilicon beam:

$$I = \frac{bh^3}{12}.$$ (3.2)
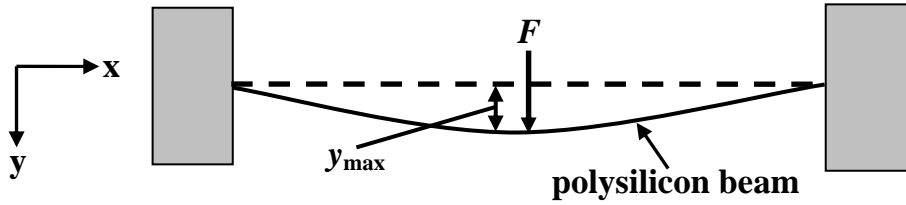
Figure 4-3: Fixed-fixed polysilicon beam with center loading.

Combining Equations (3.1) and (3.2) forms an equation for maximum deflection:

$$y_{max} = \frac{Fl^3}{16Ebh^3} \ \text{(m)} \,. \tag{3.3}$$

For this specific example, b is 1.5 μm and h is 3 μm. Assuming a 341 μm beam length as previously noted, Equation (3.3) reduces to:

$$y_{max} = 0.362F \ \text{(m)} \,. \tag{3.4}$$

The deflection of the beam in the y direction causes a curvature which is proportional to the radius of curvature (ρ) in meters, and is related to the bending angle (θ) as $\rho = 1/\Delta\theta$. It is possible to relate the radius of curvature to the mechanical parameters of the beam as:

$$\rho = \frac{EI}{M} \,, \tag{3.5}$$

where M is the moment acting upon the beam. The stress in the y-direction will be at minimum or zero stress at the center of the material and a maximum stress at the boundaries. The side of the beam with the pulling force, or convex curvature will experience tensile stress while the opposite side, inside of the curve, will experience compressive stress. Failure normally occurs at the point of maximum tensile stress.

Maximum tensile stress is located at the convex surface of the beam. Since the stress is zero at the center of the beam, half of the beam height can be substituted into this equation to derive maximum tensile stress. As such, it is possible to substitute $h/2$ into the equation for maximum tensile stress, $(\sigma(y)_{max})$. Making this substitution results in:

$$\sigma(y)_{max} = -\frac{Eh}{2\rho}.$$ (3.6)

Combining Equations (3.5) and (3.6) yields the maximum stress equation:

$$\sigma(y)_{max} = -\frac{Mh}{2I}.$$ (3.7)

Since the device is mid load and there are two beams, the moment can be defined as:

$$M = \frac{FL}{4} \ \text{(N-m)}.$$ (3.8)

Combining Equations (3.7) and (3.8), an equation for maximum tensile stress in terms of forces and distances can be derived:

$$\sigma(y)_{max} = -\frac{1.5Fl}{bh^2} \ \text{(N/m}^2)$$ (3.9)

which reduces to:

$$\sigma(y)_{max} = -18.9 \times 10^{12} F \ \text{(N/m}^2)$$ (3.10)

when the appropriate physical values are inserted into Equation (3.10).

The tensile stress point of failure has been measured at 1.2-3.0 GPa as presented in Johns Hopkins University research entitled "Tensile Testing at the Micrometer Scale"[52], depending on the manufacturer and quality of polysilicon. For the rough estimate in this derivation, it is reasonable to assume the average, or 2.1 GPa as the failure point for this polysilicon structure. Using Equation (3.10) to resolve for the force

70

applied to the structure at the point of failure due to tensile stress, the equation for the maximum force (F_{max}) that needs to be applied to the mechanical structure before it fails becomes:

$$F_{max} = \frac{2.1 \times 10^9}{18.9 \times 10^{12}} = 1.108 \times 10^{-4} \text{ (N)}. \tag{3.11}$$

Substituting this value into Equation (3.4), the maximum single beam deflection is derived as:

$$y_{max} = 4.01 \times 10^{-5} \quad \text{(m)}. \tag{3.12}$$

Recall that this calculation was for half of the total structure, thus for the entire structure, multiplying this number by 2 yields the total distance before failure of 80 μm.

With an approximation for the maximum deflection that a 350 μm structure will be able to sustain, one can determine the strain that can be applied to this device before failure occurs. Assuming the longest fiber length attached to this structure is 1000 μm, the strain required to break the test structure can be calculated as: $\frac{80 \, \mu m}{1000 \, \mu m} = 8\%$. Thus the longest structure will be able to accommodate an 8% strain of the test fiber. Since that is an order of magnitude higher than the previously measured strain, and more than the highest predicted strain of the PECT effect in a graphitic fiber, this structure is suitable for testing the PECT effect in graphitic carbon fibers.

4.1.1.2 *Modeling and Simulation*

The next step of this project was to model the devices using CoventorWare finite element MEMs modeling software. 350, 400 and 450 μm structures were designed in the design tool and meshed using a 3x3x1.5 μm manhattan brick mesh. Figure 4-4 presents the meshed beam used for finite element analysis tool.
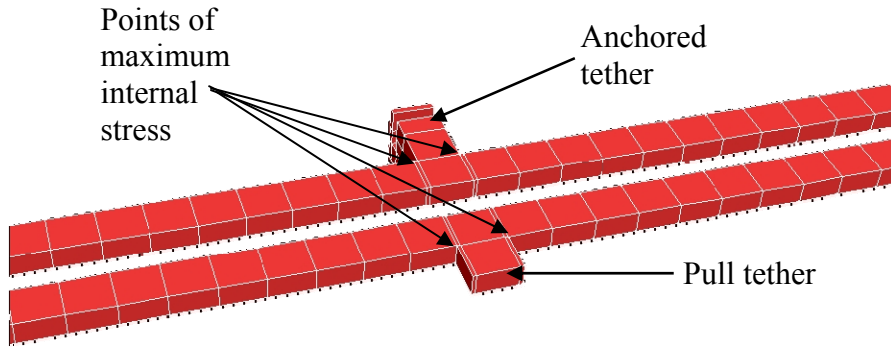
Figure 4-4: Meshed double fixed-fixed flexure in CoventorWare.

This device was modeled as the before mentioned 350, 400, and 450 μm lengths with the PolyMUMPs® run 66 data for thickness of the structures. In creating this simulation, a force on the pull tether was simulated with the anchored tether set as fixed. A displacement on the pull tether in the y direction was used for the rest of the simulation runs. The finest run was from 0 to 50 μm in 1 μm increments. Other runs were performed in 5 μm increments to speed up computation time. The total time for the 51 step run was approximately 15 minutes, a fairly low time intensity compared to some simulations with larger meshes and structures. As noted in the back of the envelope work previously presented, the force-displacement relationship is linear. This relationship for a 400 μm beam is presented in Figure 4-5.
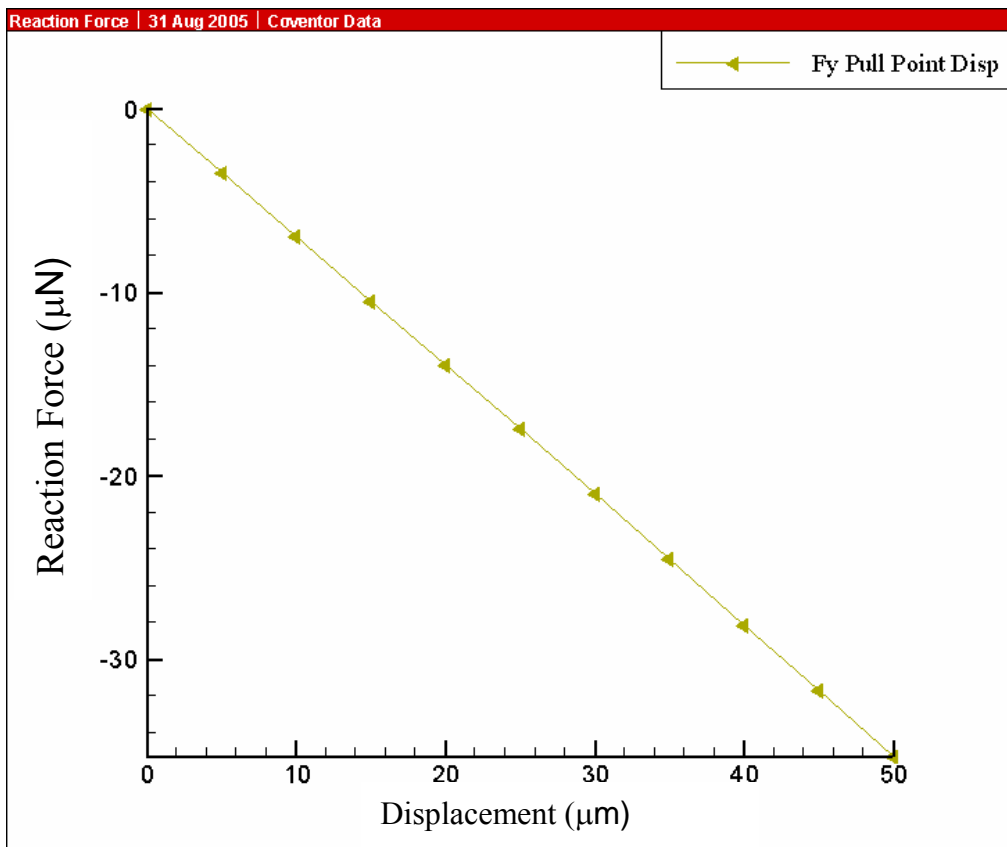
Figure 4-5: Reaction force vs Displacement for a 400 μm long modeled flexure.

Translated to this 500 μm long structure, Equation (3.4) becomes:

$$y = 0.539F \quad \text{(m)} \tag{3.13}$$

with simulation data yielding:

$$y = 1.397F \quad \text{(m)} . \tag{3.14}$$

The simulated data is 3 times higher, indicating that either some of the underlying assumptions were false in the hand calculations, or that some material parameters need to be changed in the simulation software. Data is presented in Figure 4-6 for a 450 μm flexure length, also displaced by 50 μm.

73
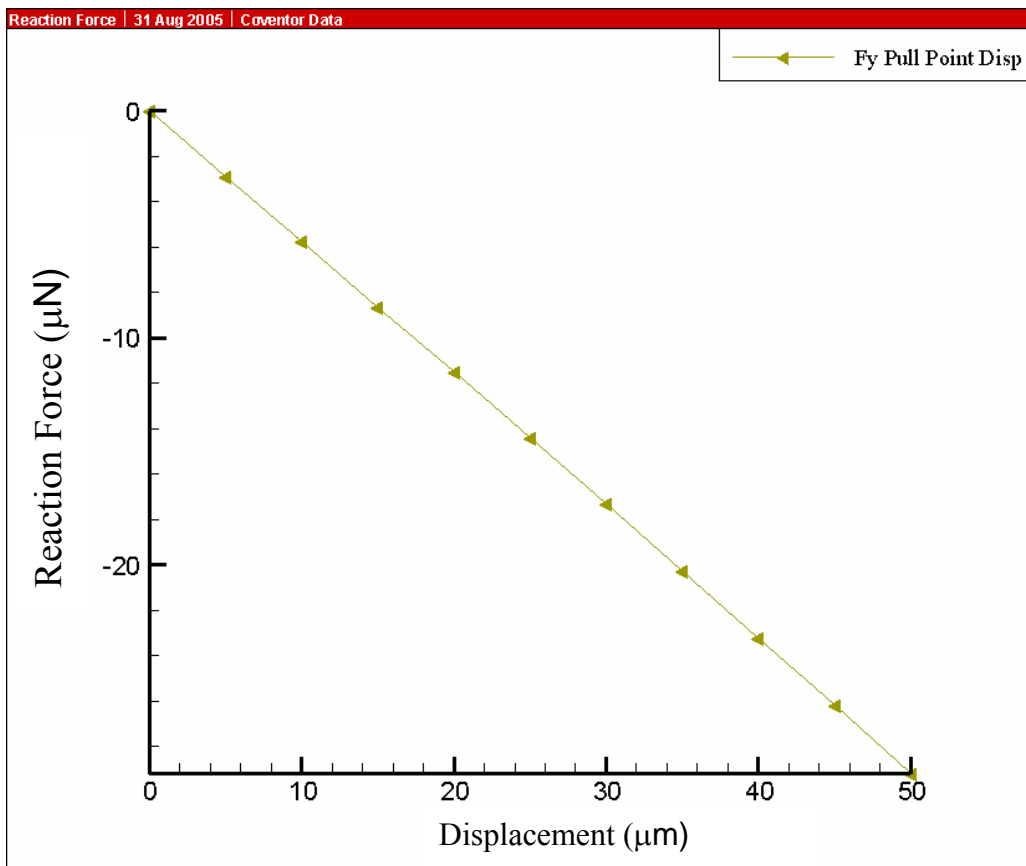
Figure 4-6: Reaction force vs Displacement for a 450 μm long modeled flexure

The data for this flexure length equates to a force given by:

$$y = 1.67F \quad \text{(m)}. \tag{3.15}$$

The hand calculation would be half that value at $0.769F$.

As predicted, the maximum stress is at the tether points. A representation of this stress for a 50 μm displacement is presented in Figure 4-7. This figure shows the Von Mises stress (or more simply Mises stress) that is simply the magnitude of stress in this material. Mises stress is one of the simplest forms of representing the stress tensor in absolute units.

Mises Stress: 3.6E-01   2.4E+02   4.7E+02   7.1E+02   9.5E+02

COVENTOR
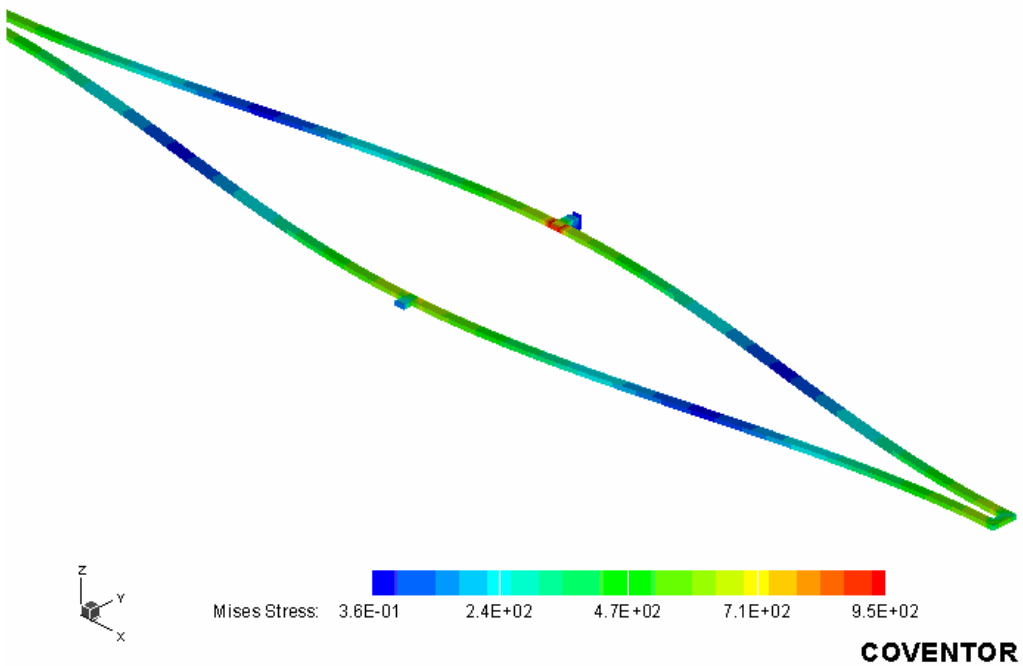
Figure 4-7: 400 μm cantilever stresses at 50 μm displacement.

The maximum stress is 950 MPa for a 50 μm displacement. This is approaching the failure point for polysilicon. Figure 4-8 presents a closer view of the principal stresses at the anchor point of this device, on a single pull analysis at the predicted breaking point to determine the stresses in the y-direction at the tether. Principal stresses take into account direction and thus can give us insight into the pieces of the device under tension and those portions under compression. The maximum stress is at the interface where the flexures attach to the piece that is only receiving longitudinal stress. This is mirrored, in a slightly lower magnitude due to the boundary conditions, at the pull tether.

75

With the compressive (negative) and tensile (positive) stresses equal, the failure point will be at the point of highest tensile stress.
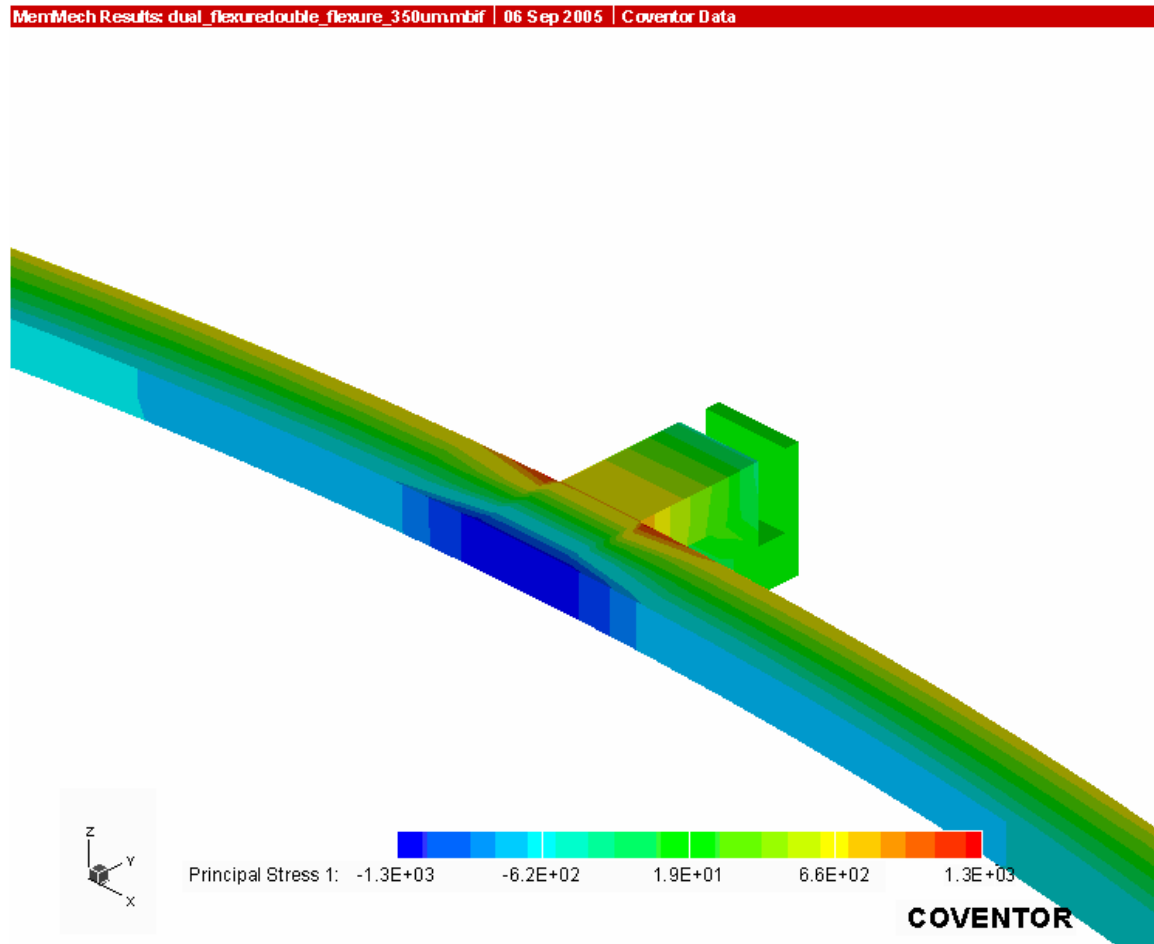
Figure 4-8: Principal stress of 350 μm double flexure at 80 μm deflection.

The resultant stress at the joint, where fracture is most likely to occur is 1.3 GPa in tension. This is actually only 8.3% different than the back of the envelope calculations for this structure, and is definitely a step in the right direction. Figure 4-8 also shows the proper gradient of stresses where the stress in the center of the beam is relatively close to zero as it should be in the interface between tensile and compressive stress.

4.1.1.3 Experimental Results

In addition to hand calculation and analysis in CoventorWare, released devices were tested. The flexure lengths ranged from 350 to 450 μm. Video of each tested structure was captured during the course of testing. The images in this section are captured still images from the recorded video. Figure 4-9 presents the deflection range as determined from the failure testing of a 450 μm double fixed-fixed center loaded flexure. This failure is determined by using a probe tip on a Micromanipulator probe station to apply lateral strain (deflection) to the device, simulating the application of strain in an assembled device. This test was accomplished to determine the critical point at which these devices would fail such that this factor could be applied to future calculations.

| (a) | (b) |
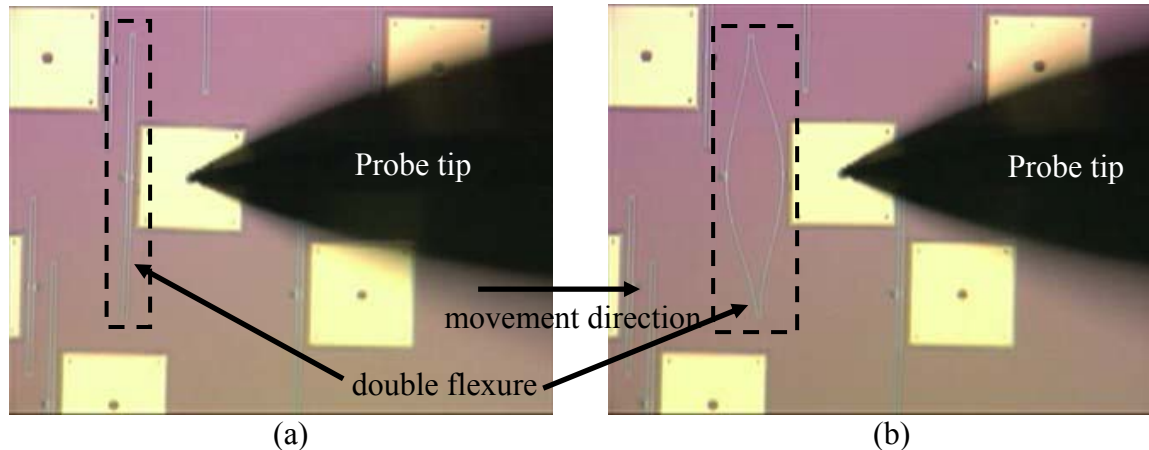
Figure 4-9: 450 μm flexure (a) at rest and (b) pulled to maximum deflection

This sequence describes a 22 second time frame where the test structure is carefully pulled perpendicular to the orientation of the flexure (to the right of the page) at an approximate rate of 4.4 μm/s. The dashed box illustrates the area containing the double flexure in each frame. Figure 4-9 (b) presents the structure at the point just before

fracture and Figure 4-10 just after the point of fracture, where the double flexure is completely detached from the bond pad.
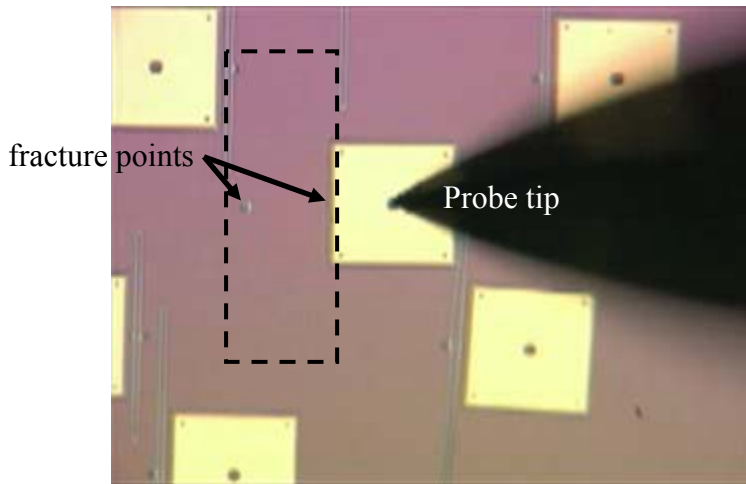
Figure 4-10: 450 μm flexure immediately after fracture.

As predicted, the flexure (while viewing with the camera real-time) broke at both tether points, one at the anchor, and one at the bondpad which is another virtual anchor for this device. According to measurements for the 450 μm device, fracture occurs after 98.5 μm of travel. Similarly, for the 350 μm device, the fracture was measured to be 57.5 μm of travel. The experimental value for the 350 μm structure is 28.2% lower than the predicted value of 80 μm. Some of this error is due to measurement scales, calibrating the optics. This places the tensile strength of the polysilicon material used in the PolyMUMPs® process, 1.51 GPa for run 66, within the nominal range of 1.2 to 3.0 GPa cited by Johns Hopkins. Three other structures were mechanically tested, confirming the tensile strength at 1.51 GPa, thus further calculations for devices created using the PolyMUMPs® process use this value rather than the median value of 2.1 GPa from the Johns Hopkins study.

4.1.2 Second Generation Test Structures

In PolyMUMPs® runs 71 and 72, test structures were designed to more accurately measure the strain produced by a PECT graphite fiber, and to measure the actuation force applied during the process. These structures are variants, based upon different amounts of force and strain possible for these devices. Previous experiments indicate that a single PECT fiber can generate over 3 grams of load, equating to 29.42 mN of force.

4.1.2.1 Rigid Flexures

The best way to measure force on a PolyMUMPs® mechanical structure is to use a fixed beam to provide a reaction force on the PECT fiber portion of the actuator. An example of the structures designed in the PolyMUMPs® process on runs 71 and 72 is presented in Figure 4-11. An expanded view of the structure is presented in Figure 4-12. Force is calculated by measuring the displacement of the device and using the specific dimensions of the beam in the measured structure in Equation (3.3).
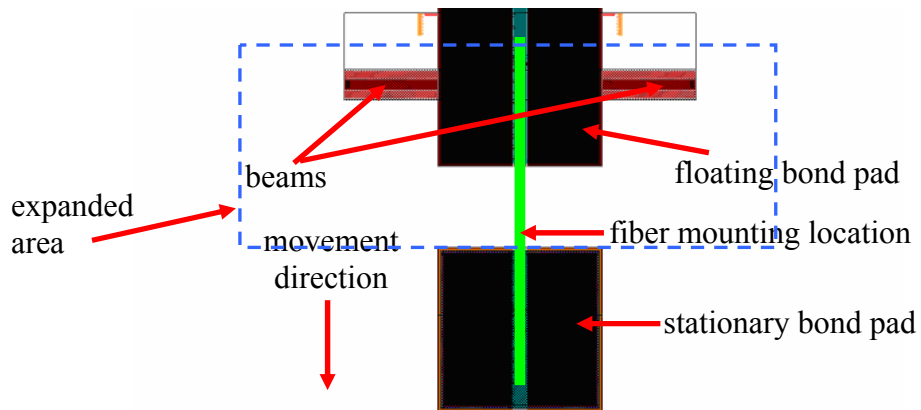
Figure 4-11: PolyMUMPs® 71 and 72 example force evaluation structure.
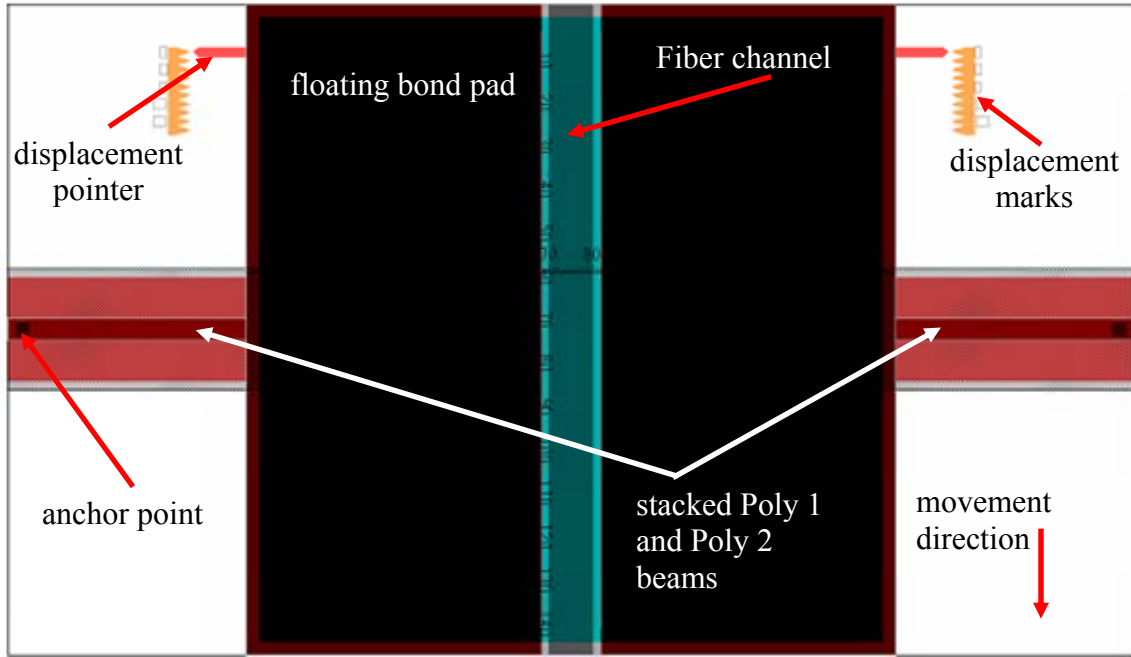
Figure 4-12: PolyMUMPs® 71 and 72 example force evaluation structure (expanded view)

Once again, PolyMUMPs® 71 and 72 devices are modeled as fixed-fixed structures, with a single fixed-fixed beam instead of two. Equation (3.9) then becomes:

$$\sigma(y)_{\text{max}} = -\frac{0.75Fl}{bh^2}.$$
(3.16)

All structures are composed of stacked Poly 1 and Poly 2 layers for a total thickness of 3.5 μm, with lengths and widths presented in Table 4-1. From this data the maximum tensile stress on the flexures can be calculated and the predicted force required to meet the tensile stress failure point determined to be 1.51 GPa. Forces required to break the flexures are presented in Table 4-2. For low electrolysis voltages, the optical measurement of deflection of these structures will allow the researcher to relate the amount of force available at each voltage setting.

Table 4-1: Force evaluation structure dimensions.

	Flexure $l/2$ length (μm)	Flexure width (μm)
Flexure 1	50	5
Flexure 2	50	10
Flexure 3	50	15
Flexure 4	50	20
Flexure 5	80	10

Table 4-2: Calculated maximum tensile strain and maximum measurable force per flexure at fracture point.

	$\sigma(y)_{max}$ (GPa)	Maximum Measurable Force (mN) at 1.51 GPa Failure
Flexure 1	$1.22 \times 10^{12} \times F$	1.23
Flexure 2	$1.22 \times 10^{11} \times F$	2.47
Flexure 3	$4.08 \times 10^{11} \times F$	3.70
Flexure 4	$3.06 \times 10^{11} \times F$	4.93
Flexure 5	$9.80 \times 10^{11} \times F$	15.40

Devices created in subsequent PolyMUMPs® runs 74 and 77, were created with 200 μm long flexures with thicknesses of 2 μm through 12 μm in 2 μm increments. The mechanical structures vary with pad size and shape; however, the pad dimensions do not affect the flexure analysis. These structures result in maximum measurable force and deflection as presented in Table 4-3 below. Deflection numbers assume a 1.51 GPa failure point as measured in PolyMUMPs® run 66. Actual values for maximum measurable deflection and force, assuming the maximum theoretical failure parameters of 3 GPa would double the amounts stated in Table 4-3. Floating bond pad sizes were reduced from 150 μm × 150 μm to 50 μm × 150 μm and 50 μm × 50 μm to increase ease of oxide removal. Since the bond pad size does not affect the reaction force, the two differing sizes are equivalent for testing purposes.

Table 4-3: Calculated maximum tensile strain, maximum measurable force and maximum deflection per flexure at fracture point for 2-12 μm flexures.

Flexure Width	$\sigma(y)_{max}$ (GPa)	Maximum Measurable Force (mN) at 1.51 GPa Failure	Maximum Measurable Deflection (μm)
2 μm	$2.14\times10^{13}\times F$	0.0705	7.15
4 μm	$5.36\times10^{12}\times F$	0.282	3.57
6 μm	$2.38\times10^{12}\times F$	0.634	2.38
8 μm	$1.34\times10^{12}\times F$	1.13	1.79
10 μm	$8.57\times10^{12}\times F$	1.76	1.43
12 μm	$5.95\times10^{11}\times F$	2.54	1.19

4.1.3   Trenching Mechanical Structures

Initial experiments in integrating the planar PolyMUMPs® mechanical structures with carbon fibers met with limited success. Adhesion of the carbon fibers to polysilicon structures proved problematic due to the cylindrical shape of the fiber and the planar nature of the mechanical structure. Without a significant mass of adhesion material, it became virtually impossible to reliably bond the two together.

The solution to this bonding problem was solved in PolyMUMPs® run 71 and later. This solution entailed simply using the available layers in the micromachining process to create a trench in the middle of the structure. The trench was designed to be as close in depth to the radius of the carbon fiber as possible, and just as wide as the diameter of the carbon fiber. Figure 4-13 presents a cross-sectional view of the trench designed in the PolyMUMPs® process to hold the carbon fiber portion of the actuator system. This trench and the recession of the fiber present many benefits in both attaching the fiber and in testing the structure. First, this configuration allows for more area of the fiber to contact the polysilicon mechanical structure to create a better mechanical contact. Second, it lowers the centerline of the fiber in comparison to the mechanical structure, greatly reducing the torsional moment that the fiber exerts on the polysilicon mechanical

structure. Finally, due to the conformal nature of the underlying material, more surface area of the fiber contacts the surface of the underlying structure, generating a more reliable electrical contact.
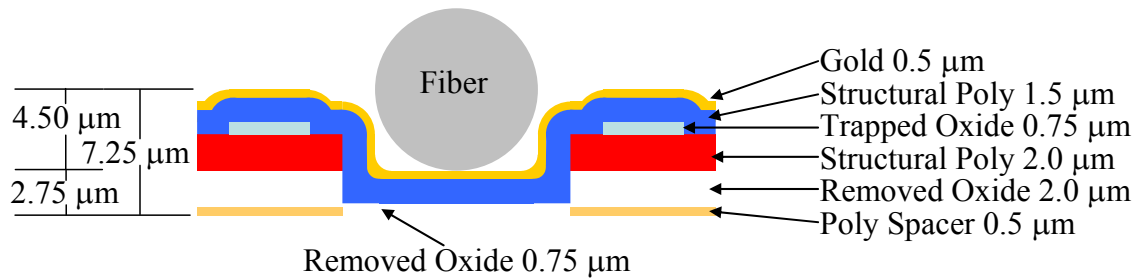
Figure 4-13: Cross-sectional view of trench designed in PolyMUMPs® micromachining process

4.1.4   Attaching Carbon Fibers to PolyMUMPs® Structures

Testing the mechanical nature of PECT-based carbon fibers in an aqueous electrolyte solution required that, at a minimum, one side of the test fiber must be attached to the underlying polysilicon mechanical structure. For measurement purposes, the design for polysilicon beams was previously discussed to provide varying degrees of reaction force to the carbon fibers. Attaching the two disparate surfaces together, however, proved to be a time-consuming process that met with several failures prior to finally discovering the most reliable methods of attachment. The methods that were researched along with their modes of failure are presented in Appendix A. One of the successful methods, lift-off metallization, yielded some positive results, which prompted the continuation of this research, resulting in the deposition of metal directly on the fiber and underlying structure. This method used a Nova Nanolab 600 multiple column scanning electron microscope, with a focused ion beam column that is able to deposit platinum metal on the surfaces by patterning through a heated platinum gaseous

83

compound. Figure 4-14 presents a cross-sectional view of final metallized end of a mounted carbon fiber and Figure 4-15 presents a similar fiber mounted using the focused ion beam method.
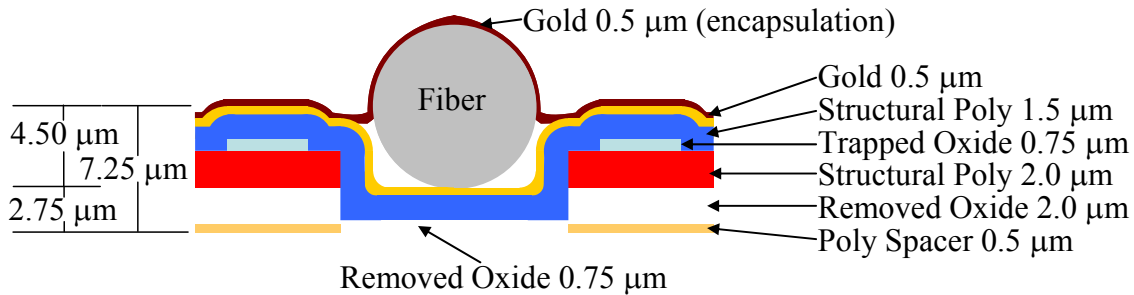
Figure 4-14: Cross-sectional view of a carbon fiber mounted in a PolyMUMPs® mechanical structure and encapsulated with a 0.5 μm layer of gold.
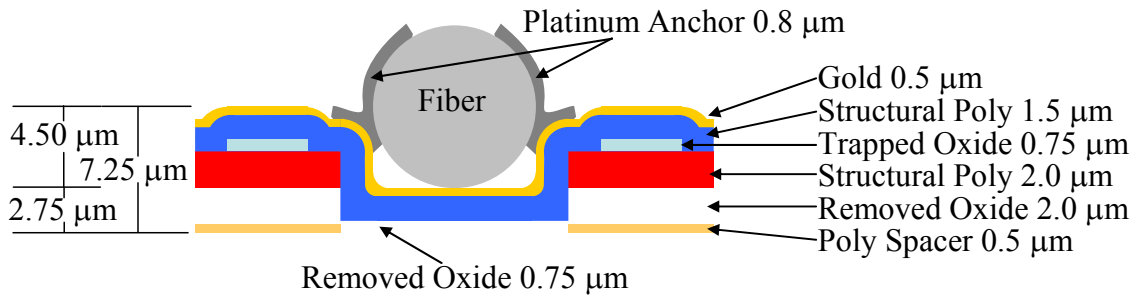
Figure 4-15: Cross-sectional view of a carbon fiber mounted in a PolyMUMPs® mechanical structure and attached with two 7x12 μm square, 0.8 μm thick platinum patches.

Although the deposited platinum contacts a smaller surface area of the fiber, it has several distinct advantages over lift-off metallization. The first of these advantages is that fewer processing steps are required. For metallization, the fibers need to be placed, with a temporary epoxy, in the locations where they need to be tested. Following this step, two layers of photoresist were applied and subsequently patterned using a Karl Süss MJB3 ultraviolet contact mask aligner. The patterning was accomplished in a non-contact

configuration due to the non-conformal nature of the die, and each die was subsequently developed to open "windows" where the gold pads lie. MicroChem corporation's SU-8 negative tone photoresist and LOR 3A sacrificial photoresist were utilized during photolithography, following the recipe contained in Appendix B. The bottom layer of photoresist must have a larger opening than the upper layer and be at least 0.5 μm thick to ensure the unnecessary gold will lift off. This air gap created by the larger opening and tall top photoresist layer prevent excess gold from remaining on the die and protects gold holding the fibers to the polysilicon structures from being removed with the photoresist. This step is followed by metallization, in which the photoresist covered chip is placed in a Denton electron beam deposition system, which covered the die with 100 Å of titanium as an adhesion layer, followed by 5000 Å of gold. Once removed from the chamber, the SU-8 and LOR3A photoresists used to mask the metallization areas were removed with MicroChem's 1165 stripper, heated to 90 °C, soaked for 90 minutes using fresh solution every 10 minutes to prevent redeposition of the dissolved photoresist and gold flakes. The solution was changed by holding amounts of 1165 stripper in a small Petri dish. Once the 10 minutes expired, the die was moved from one dish to the next, the used solution captured in a waste bottle, and new stripper replaced in the now empty dish from an at-temperature beaker of stripper. The final metallized fiber/pad combination is presented in Figure 4-16.
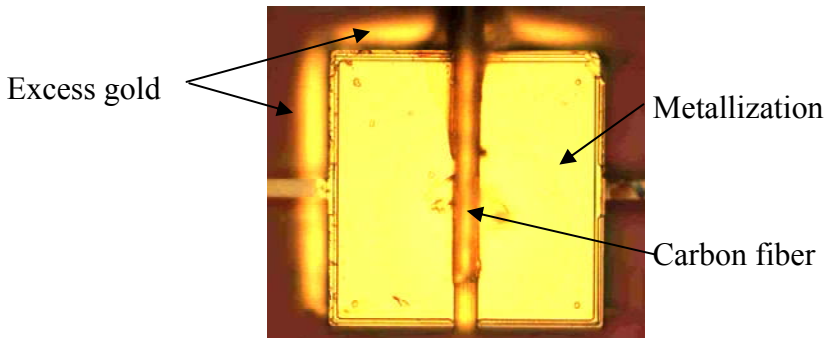
Figure 4-16: Metallized carbon fiber adhered to polysilicon floating bond pad.

Excess metal deposited in this procedure, due to a slight offset of the mask with the underlying PolyMUMPs® structure, remains on the silicon dioxide layer of the PolyMUMPs® structure. The oxide layer is removed and thus the excess metal does not interfere with the testing.

In contrast to the lift-off metallization process, the platinum deposition process requires no temporary adhesive. The fiber can be mounted in the channel using the frictional forces between the two surfaces. This method prevents any adhesive from wicking up the fiber length and possibly reducing the amount of fiber under intercalation during testing. The mounted fiber is then placed in the NOVA Nanolab 600 dual beam scanning electron microscope (presented in Figure 4-17) and aligned so that the ion beam is incident at 52° from the normal to the surface of the die. This allows a larger amount of metal to bridge and attach between the fiber and the trench, as indicated in Figure 4-15. The process takes a little over 5 minutes per patch, for a total of 20 minutes per fiber to put four 7 x 12 x 0.8 µm platinum patches on, two per end of the fiber. The final result is a cleanly mounted fiber with very little contaminants, and is presented in Figure 4-18.
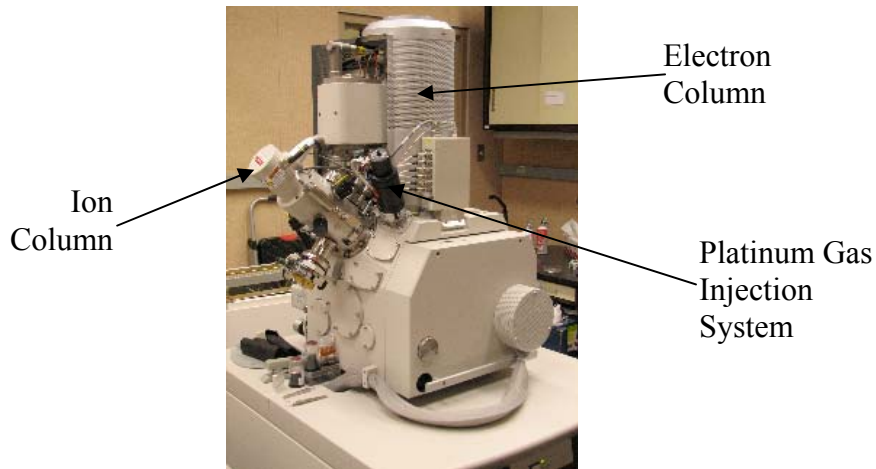
Figure 4-17: Nova Nanolab 600 dual beam scanning electron microscope with gallium focused ion beam and platinum deposition gas injection system.

4.1.5   Precision Enhancement

In an attempt to more accurately measure the strain experienced by a PECT carbon fiber, additional mechanical structures were designed for PolyMUMPs® runs 72, 74, and 77 that allow for the measurement of strain using a mechanical multiplier.   This mechanical multiplier is the simple application of geometric multiplication by the selective placement of a fulcrum. Accuracy of the final measurement using this fulcrum device is within 0.25 µm with no additional processing other than extending the displacement of the pointer to the measurement grid.   This can determine strain to within 0.0027% on the longest designs.   Five versions of this device were fabricated which could measure 0.02% to 1.78% strain. The devices were designed to measure strain in specific ranges by creating a different gap between the movable bond pad and the measurement device for each strain range.   Table 4-4 presents the strain range each of these five versions were designed to measure, given a nominal 8000 µm length fiber attached as a part of this micro-actuator system.
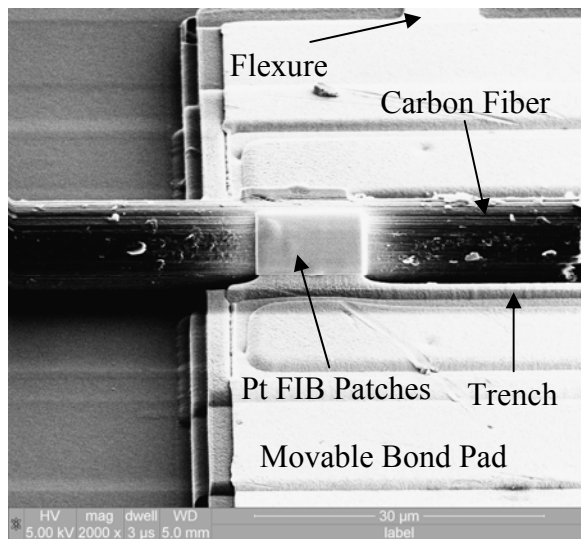
Figure 4-18: Carbon fiber attached to polysilicon floating bond pad with two 7 x 12 x 0.8 μm platinum patches.

Table 4-4: Force multiplication measurement device and associated measurement ranges.

	% Strain Measurement Range	
	Minimum	Maximum
Device 1	0.022185	0.144082
Device 2	0.332779	0.454676
Device 3	0.665557	0.787454
Device 4	1.220189	1.342086
Device 5	1.663894	1.785791

Figure 4-19 presents the general design of a mechanical multiplying measurement mechanism that is suitable for precise measurement of small changes in position. As the fiber contracts, it pulls the floating bond pad toward the measurement mechanism, which narrows the gap between the measurement pawl and the beam acting as the mechanical multiplier. The variable gap allows for a known distance that the pawl has to travel before reaching contact with the mechanical multiplier. Once the measurement pawl contacts the mechanical multiplier, it causes a multiplied displacement based upon the ratios of length on each side of the pawl which acts as a mechanical fulcrum. The

88

multiplication factor used in the design due to size constraints is 3.64. The displacement of the tip of the multiplier can then be measured and the distance from the contact point can be calculated and added to the initial design gap to determine total displacement. Displacement can then be divided by the length of the fiber to directly determine the strain that the fiber is inducing on the mechanical structure. An example measurement using an actuated device is presented in Figure 4-20.

This precision measurement device was fabricated, but with only a 20% yield due to offsets in the layers of the PolyMUMPs® process. Small offsets in some of these devices caused shears in points where a solid structure was designed. The structures were designed to the minimum acceptable tolerances of the stated process and did not receive adequate results. Solutions were iterated from these initial multiplication structures to include more robust structures and less aggressive pursuit of the fabrication tolerances in the design. The mechanical multiplication devices evolved into a radial design that would follow the movement of the pointer over a larger range of deflections. The final design was a 10x multiplier capable of 0.1 μm accuracy before any optical enhancement was used. Figure 4-21 presents the final design for precision enhancement. A second version with rigid flexures instead of pinned joints using the same geometry was later designed. The limitation of a pin hinge process is that the pins will inherently move 0.75 μm (the thickness of the released oxide layer) before coming into contact with the hinge surrounding it. Thus a 2-pin hinge device would ignore the first 1.5 μm of travel, and the fixed device adds unnecessary reaction force to the device.
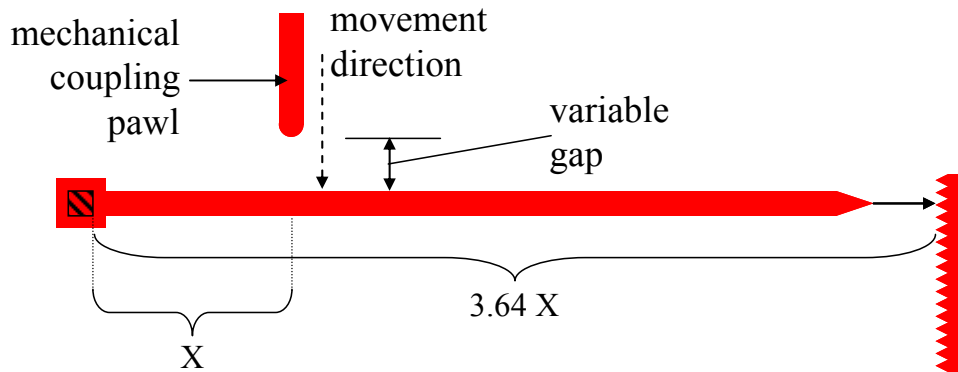
Figure 4-19: Mechanical force multiplication precision measurement mechanism.
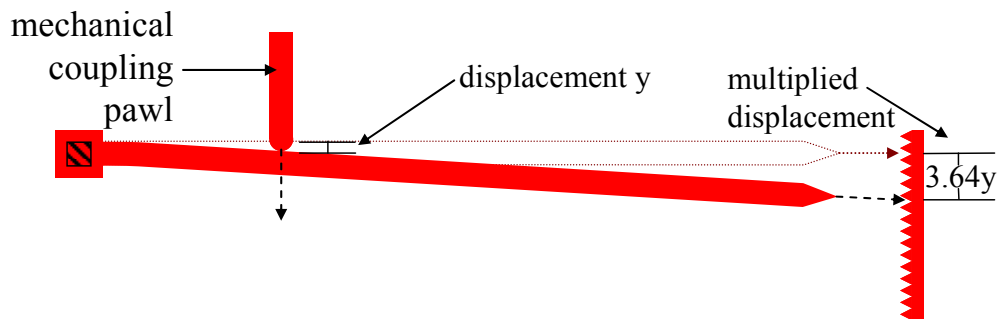
Figure 4-20: Measurement example utilizing mechanical force multiplication.
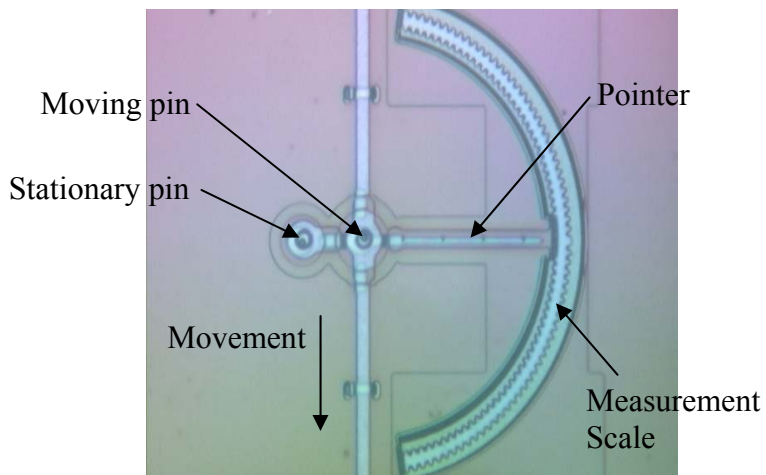
Figure 4-21: Final precision enhancement mechanism fabricated in PolyMUMPs[®] run 77.

Due to limitations in the polysilicon micromachining process, an optical solution that used pixel count at a 100 times magnification factor on a Micromanipulator probe station to obtain an accuracy of 4.4 pixels per μm was used. This method required no additional hardware and was thus the simplest solution that could be used to increase accuracy. Since the pixilation option yields a 0.22 μm resolution, less than the options for the mechanical devices, with no error in resolution due to fabrication, the optics option was chosen once testing began.

4.1.6 Test Sample Encapsulation

In order to test the carbon fibers in an aqueous sulfuric acid environment and still observe the reaction, a way to encapsulate the test die into an enclosed container with external electrical contacts to allow for testing was required. The ideal structure for this testing is a deep well 40 pin dual inline package ceramic integrated circuit carrier. This carrier had a deep well that could hold the test die and sulfuric acid, and had glass covers available to encapsulate the entire system while under test. The first attempt at encapsulation involved putting a small amount of non-volatile liquid in the well of the carrier and attempting to seal the glass cover with paraffin wax, similar to Dr. Vogel's initial research on the PECT effect. Unfortunately, the paraffin easily delaminated and could not produce a reliable contact to prevent the glass cover from detaching from the carrier.

The next logical step was to encapsulate the edges of the glass cover with Crystalbond™ 509 manufactured by Electron Microscopy Sciences. Crystalbond™ 509 is a high temperature wax used to mount a small sample on scanning electron microscope stubs and which was also use to mount a sample in the 40 pin chip carriers during wire

bonding. The melting point of crystal bond is approximately 110° C, a temperature at which sulfuric acid will begin to aggressively etch materials, so a low-temperature option was developed to encapsulate the die in the carrier using Crystalbond™. In order to seal the die prior to applying the acid, two small holes were drilled in the corner of the glass covers to make intake and exhaust holes. Once the test die was wire bonded to the 40 pin carrier, crystal bond was used around the edges to seal the majority of the slide. This was performed by heating the substrate and, using tweezers and a small piece of crystal bond, created the sealant bead and mounded crystal bond around the holes in the slide. This allowed the application of a few drops of sulfuric acid at room temperature through one of the holes, and allowed the air trapped inside of the carrier to exhaust through the second. Once this was complete, a short (< 2 second) application of a low temperature glue gun tip was used to enclose the mounded crystal bond over the two holes. Figure 4-22 presents the final sealing method using crystal bond. The resultant structure allowed us to image each individual actuator at a 100x resolution and use this to determine total strain for each fiber. Figure 4-23 presents an image of the final enclosed carrier prior to adding acid.
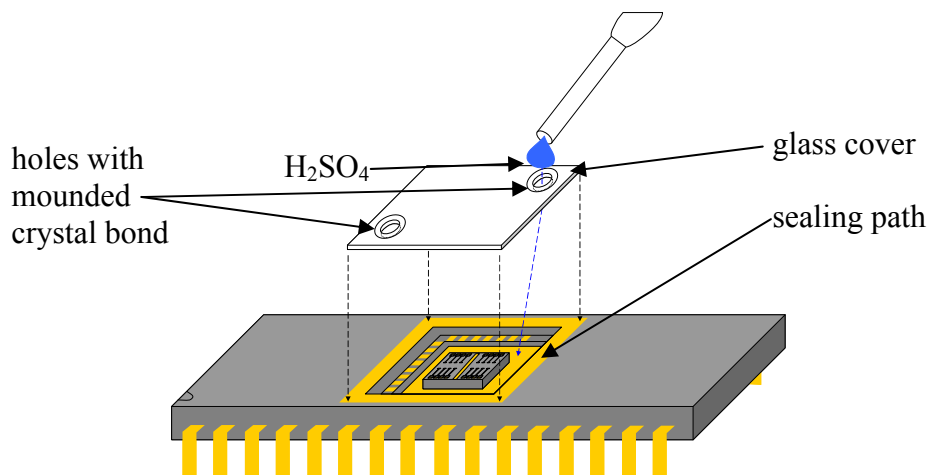
Figure 4-22: Encapsulation method to enclose test die and sulfuric acid in 40 pin dual inline package.
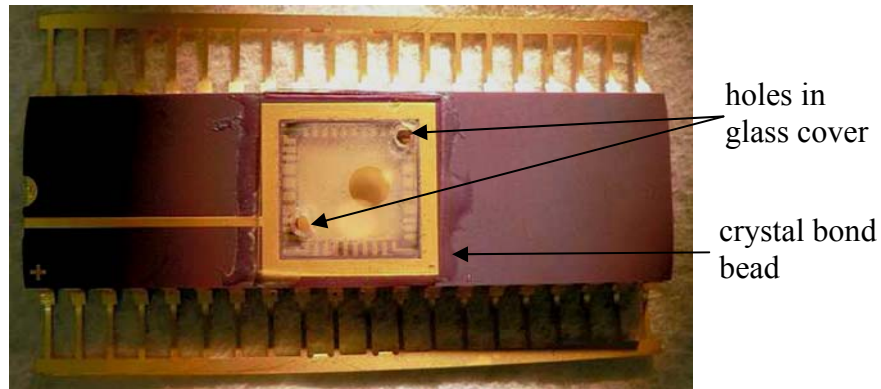
Figure 4-23: Encapsulated chip carrier using crystal bond high temperature mounting wax as sealant.

4.1.7   Mechanical Experiments

Mechanical experiments were conducted on carbon fibers mounted to test structures fabricated in PolyMUMPs® runs 67, 74 and 77. Run 67 structures were tested with both metallization and FIB patch fiber attachment options, and runs 74 and 77 with only FIB patch attachments. During the course of testing, it became evident that some of the fibers were bonded to the polysilicon poorly and thus delaminated from the underlying polysilicon during the course of testing. This delamination allowed the observation of the reaction for a fiber under no loading conditions. Stress data was compiled for twelve fibers which were under no load conditions. These fibers ranged in length from 500 to 1500 μm with the more reliable responses due to geometry occurring in the devices utilizing 500 μm fibers.

To determine the range of responses available in a single fiber, a 7 run analysis was also performed on a single 500 μm fiber to determine repeatability of the final device. Run data from 0 to 1.6 V in 0.05 V increments was collected, with voltages changing to the next step every 20 seconds using VEE software to control an Agilent

6624 DC power supply. Figure 4-24 presents an the 7-run series on this 500 μm unloaded fiber illustrating the range of values at each electrolysis voltage, including the minimum, maximum, and average strain between the 7 runs. Minimum and maximum strain in this figure is represented by the error bars deviating from the mean value for the series of tests on that fiber. The data is limited to display non-zero data points, from 1.0 to 1.6 V of intercalation voltage. The data presents values from 0 strain at 1.0 V to 0.0052 at 1.6 V of applied potential. As such, the predicted point at which oxygen bonding begins to occur predictably forms at 1.4 V of potential, with a strain of 0.0022 and an end result of this overpotential being 0.0032 strain contributed by carbon-oxygen bonding. This is approximately one oxygen bond per 392 carbon atoms, or $C_{392}O$.

The average strain produced by 11 fibers, which includes five 500 μm fibers, four 720 μm fibers, one 1420 μm fiber and one 1500 μm fiber is presented in Figure 4-25. Results can be directly compared to the 7 run series data previously presented. The average strain of the 11 fibers measured is merely a shift of the curve for the 7-fiber baseline testing performed. For this average data, the overpotential where oxygen bonding begins to occur is as low as 1.0 V of applied potential, 0.3 V lower than expected were a platinum electrode to have been used. However, the final 0.0093 strain induced in the average fiber has carbon-oxygen bond contributions at 1.6 V applied potential of 172 carbon atoms per oxygen bond or $C_{172}O$.

Strain vs. Voltage
Average of 11 Untethered Fibers
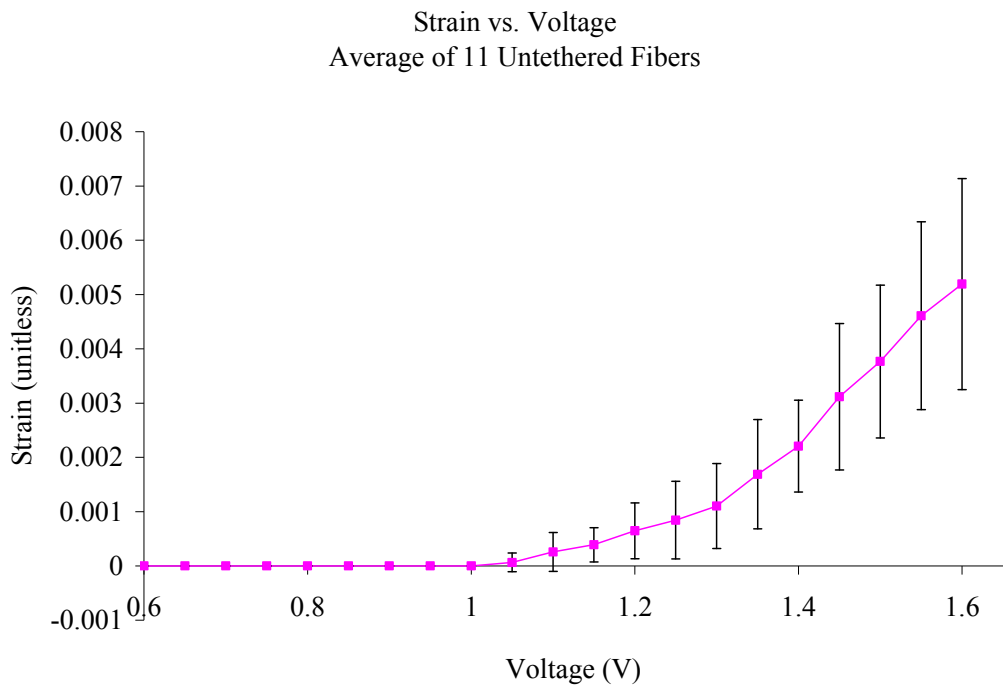
Figure 4-24: Unloaded 500 μm carbon fiber strain results for 7 run series from 0 to 1.6 V DC intercalation voltage, average strain with one σ deviation noted in error bars.

Strain vs. Voltage
Average of 11 Untethered Fibers
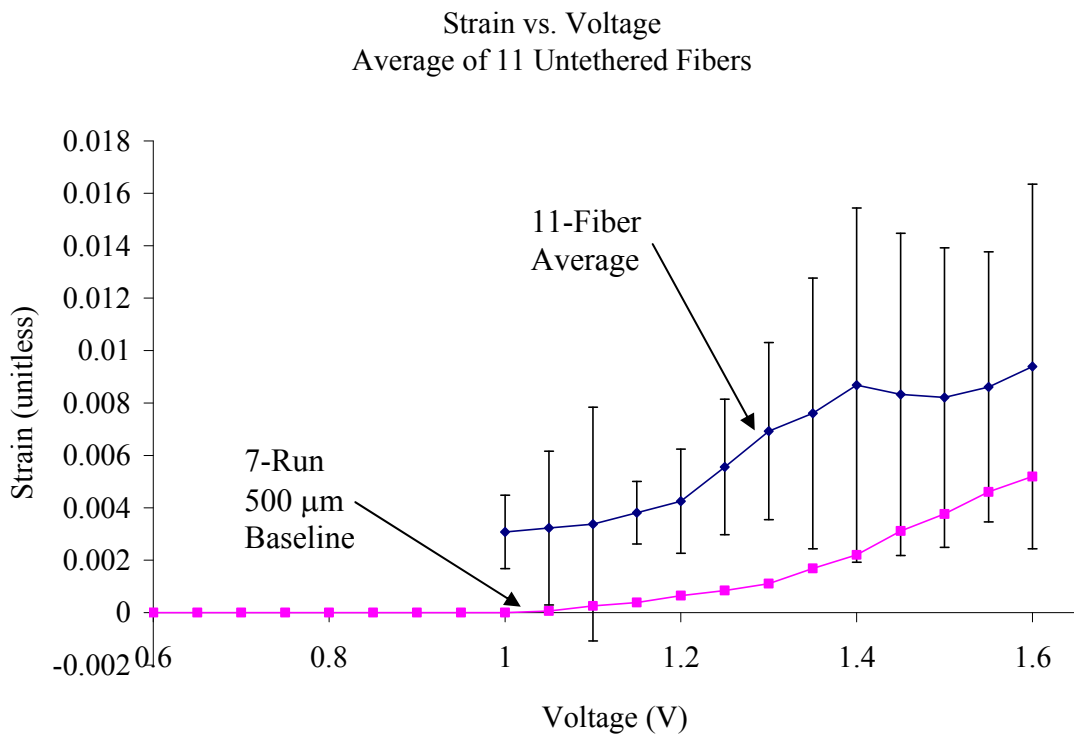
Figure 4-25: Average strain response of eleven unloaded 500 to 1500 μm length Thornell® P-100 carbon fibers with one σ deviation noted in error bars.

Differences in the data presented in Figure 4-25 are attributable to several different phenomena. The first is that none of the carbon fibers are completely straight. Each fiber, at scales under 2 mm, exhibit slight bends or concavity along the length of the fiber. These irregularities can cause a reduction in the observed strain, as the fiber will, in the case of a loaded fiber, straighten before it pulls the mechanical structure. In the case of an unloaded fiber, the bends can cause movement in three dimensions instead of a restricted one-dimensional pull. Additionally, since the fibers are graphitized but not perfect graphite, the fibers can have differing degrees of graphitization across their diameter. This causes intercalation to work more efficiently in one area of the fiber and cause differential stresses and curl rather than just shortening the fiber. The curling of the fiber can cause the end to move out of plane along both the x- and z-axis in addition to the desired y-axis contraction. These differences will cause a shift of the curve based on how efficiently the device is contracting as opposed to expending energy in the out of axis distortions.

The data for 11 unloaded fibers was then charted and compared to an ideal calculation for unloaded response of the polysilicon MEMS thermal actuatios and one of the best piezoelectric materials, PVDF at the same range of voltages. Figure 4-26 presents this comparison, and shows that the PECT effect achieves nearly a 2 order of magnitude increase in strain when compared to polysilicon thermal expansion and piezoelectric PVDF. Note that the scale on the y-axis of this chart is logarithmic to accommodate the large difference in strains between the different materials.
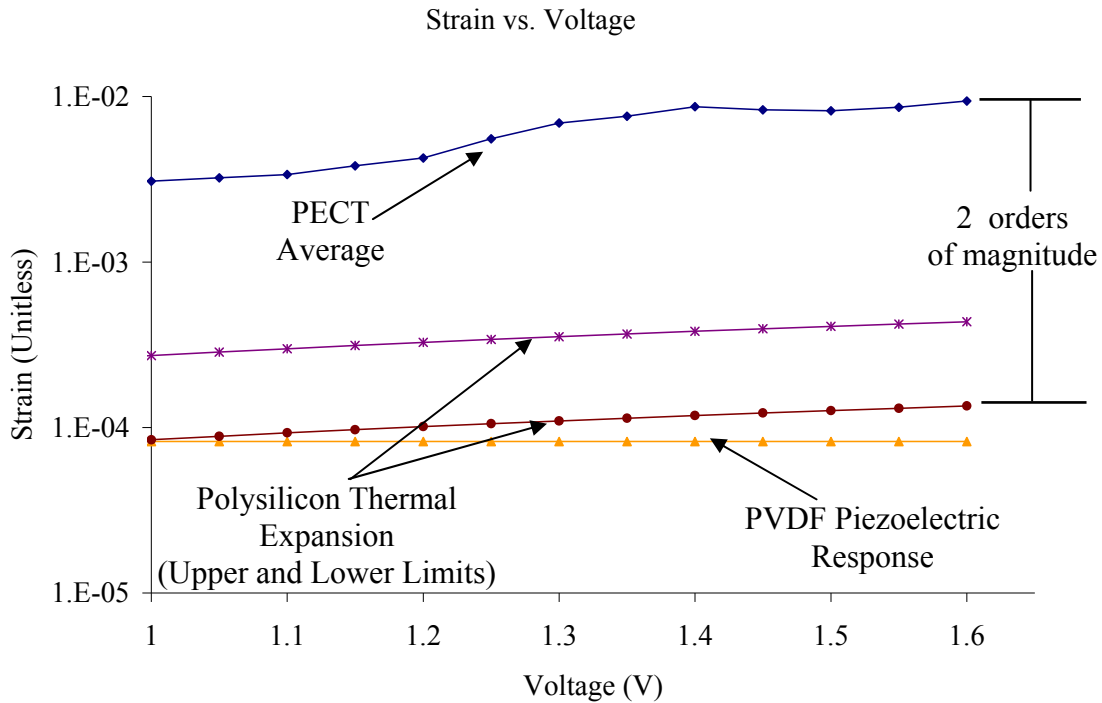
Figure 4-26: Comparison of unloaded strain: average PECT, polysilicon thermal expansion and piezoelectric PVDF. (note: strain is represented on a logarithmic scale to separate lower series from zero).

Following these tests, the response of fibers under load was measured, as designed and discussed in Section 4.1.2.1 previously. Seven different fibers ranging from 500 to 1000 μm long were measured under varying strain. Table 4-5 presents the combination of reaction mechanisms (polysilicon beams) and fiber lengths tested.

Table 4-5: Carbon fiber lengths and their corresponding polysilicon beam reaction mechanism dimensions.

Fiber Length	Flexure Dimensions
500 μm	3 μm x 250 μm fixed-fixed center load
500 μm	4 μm x 200 μm fixed-fixed center load
500 μm	5 μm x 200 μm fixed-fixed center load
720 μm	10 μm x 200 μm fixed-fixed center load
720 μm	5 μm x 200 μm fixed-fixed center load
985 μm	20 μm x 200 μm fixed-fixed center load
1000 μm	10 μm x 200 μm fixed end load

The least restrictive design, the 10 µm × 200 µm fixed, end loaded beam yielded the most easily observable results. This structure was originally a fixed-fixed center loaded structure, but in order to test this structure as well as the adjacent structure, it was necessary to shear one side of the structure and isolate it from it's neighbor. The structure was sheared using a probe tip on the Micromanipulator probe station to break the thin flexure prior to releasing the device. Figure 4-27 presents an illustration of the single fixed, "end loaded" device. The end reference point is the centerline of the carbon fiber in this drawing.

A still-frame image of the strain that a 1000 µm long P-100 carbon fiber can yield, while under small load from a polysilicon spring, is presented in Figure 4-28. Figure 4-28 (a) presents the device at rest, under 0 V of electrolysis voltage, while Figure 4-28(b) presents that same device actuated at 1.4 V. The change in length was measured from the centerline of the fiber to allow a direct calculation of the strain induced at each intercalation voltage.
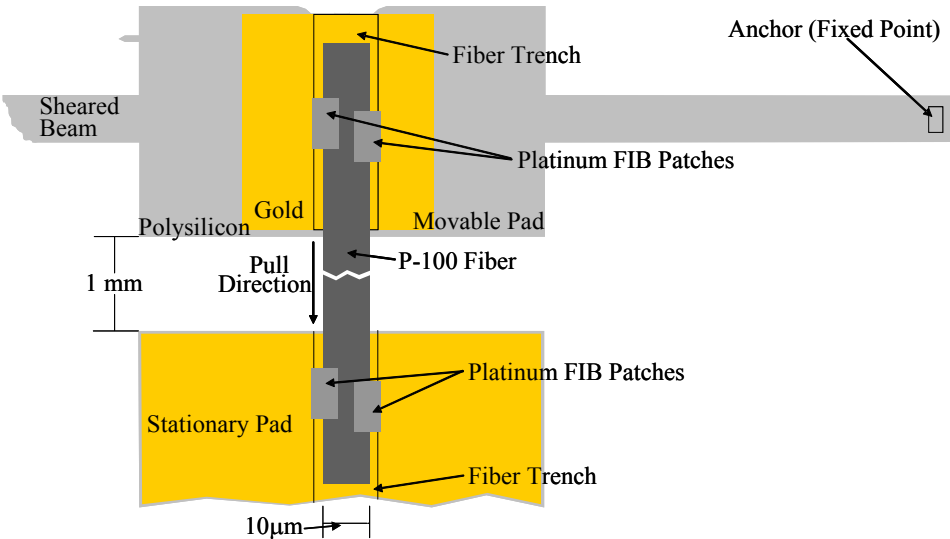
Figure 4-27: Illustration of reaction force mechanism for one test location of a 1000 µm long carbon fiber.
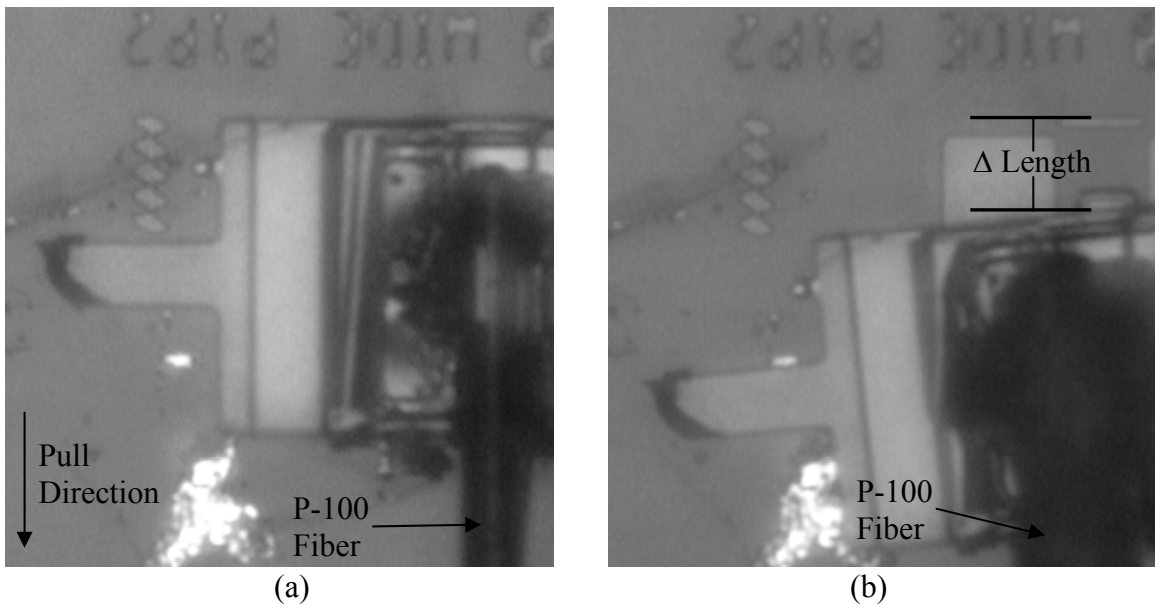
Figure 4-28: Site 11 reaction force mechanism for 1000 μm long carbon fiber (a) at 0 V DC electrolysis voltage and (b) 1.4 V DC electrolysis voltage, both imaged through slide cover and sulfuric acid.

In this case, the polysilicon beam on the right side of the device fractured at 1.5 V electrolysis voltage, tearing the structure away from the substrate. This fracture was produced by the travel of the polysilicon structure, moved by the contraction of the 1000 μm carbon fiber, causing the tensile stress to exceed the failure point in the polysilicon. This excessive tensile stress caused the polysilicon beam to fracture at the point of greatest tensile stress, which is at the tethered end of the right beam. At 1.4 V electrolysis voltage, the fiber caused 1.7% strain and induced 69.41 MPa of internal stress, pulling with 5.45 mN of force on the polysilicon structure. This corresponds to 39.66 MPa of stress for each percent of strain induced. In comparison, and due to the differing reaction force applied by the polysilicon structure, the other fibers produced strain dependent stresses as presented in Table 4-6.

In general the stress/strain ratio tends to be higher as the beam geometry increases. This is due to the fact that these beams are progressively stiffer and produce more reaction force, thus a small displacement and resultant strain will produce a larger stress, and the ratio of a larger stress to a smaller strain increases greatly. Also, when comparing to the strain measurement possible with these geometries for polysilicon beams as described in Section 4.1.2.1 , note that none of the flexures exceeded the

Table 4-6: Stress induced per site in relation to strain produced.

Fiber	Geometry (µm)	Stress/strain (MPa)	Fiber Length (µm)
1	3 x 250	26.47	500
2	5 x 200	176.47	500
3	4 x 200	250.98	500
4	5 x 200	490.20	720
5	10 x 200	1412.51	720
6	10 x 100	3966.46	1000
7	20 x 200	61804.07	985

fracture point as calculated. However, the end load case that was evaluated with fiber 6 fractured at the voltage just after it had achieved a change in length of 17.1 µm, while calculations predict fracture of a 1.51 GPa material of that geometry at 17.76 µm using the equation

$$y_{max} = \frac{2 \times 1.51 \times 10^9 \times L^2}{170 \times 10^9 \times h} \text{ (m)} \tag{3.17}$$

which is derived from Equations 3.4 and 3.11.

The strain produced in fibers that had reaction forces applied to them is presented in two figures. Figure 4-29 presents data for the three 500 µm long fibers, while Figure 4-30 presents the data for the remaining four fibers. Error in these measurements is calculated from the single pixel error in determining the line width of a feature in pixels

100

and equals 0.227 µm divided by the length of the fiber (to determine strain error from pixel count error), but was not plotted to reduce clutter. With the single exception of the 176.5 MPa/strain device in Figure 4-30, all loaded fibers consistently reach overpotential at the predicted 1.3 V of applied potential. Larger reactive stresses however, diminish the amount of contribution the carbon-oxygen bonds provide to device strain.
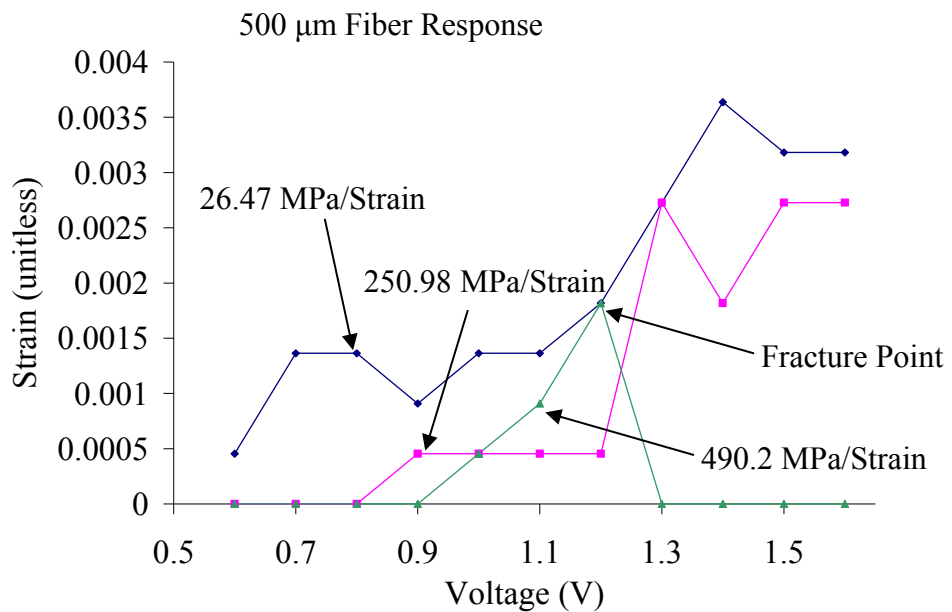
Figure 4-29: Strain induced on 500 µm fibers under 3 separate reaction force conditions.

In Figures 4-29 and 4-30, the increased reaction forces cause a shift in the strain curve to the right. It takes more voltage to successfully achieve actuation, as is logical under those circumstances. The amount of strain is also reduced in magnitude, as is evident in the green triangle series on Figure 4-30 when compared to the less loaded fibers. The stress in this fiber is massive compared to the size, and even a small bit of strain is a significant accomplishment for this actuator.

720, 985 and 1000 μm Response
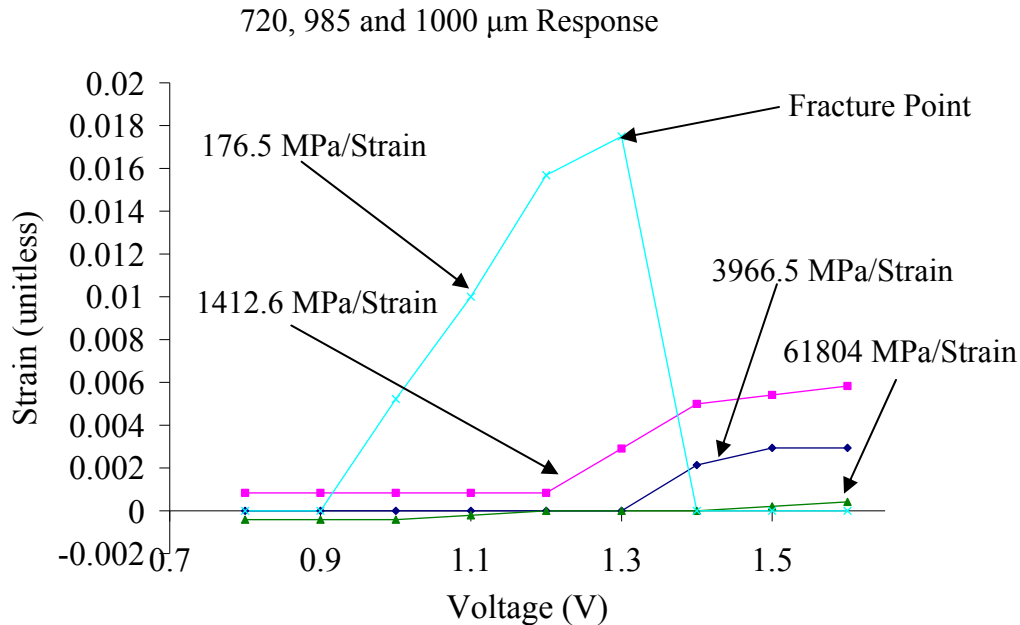
Figure 4-30: Strain induced on 720, 985 and 1000 μm fibers under four separate reaction force conditions.

4.1.8 PECT Current Profile

While testing the 500 μm fiber using a 7 run series for repeatability, LabView™ software was used to acquire precision current measurements. This software allowed the capture of 500 samples of current data from the Agilent Technologies 34401a 6½ digit digital mulitmeter per trigger, collecting an average of 160.5 current samples per second, over 127,000 current samples per test. Figure 4-31 presents the raw current data for all 7 runs of the repeatability test on a 500 μm long unloaded carbon fiber. Due to the imprecise nature of the start times between applications, it was necessary to slightly time shift the current to align points of voltage change with each other. The general trend of this data indicates that work is occurring upon each change in voltage, and that when the VEE program reset the voltage on the DC power supply, the momentary lack of output

voltage caused an inverse current spike, which indicates that deintercalation is occurring during that small period of time.
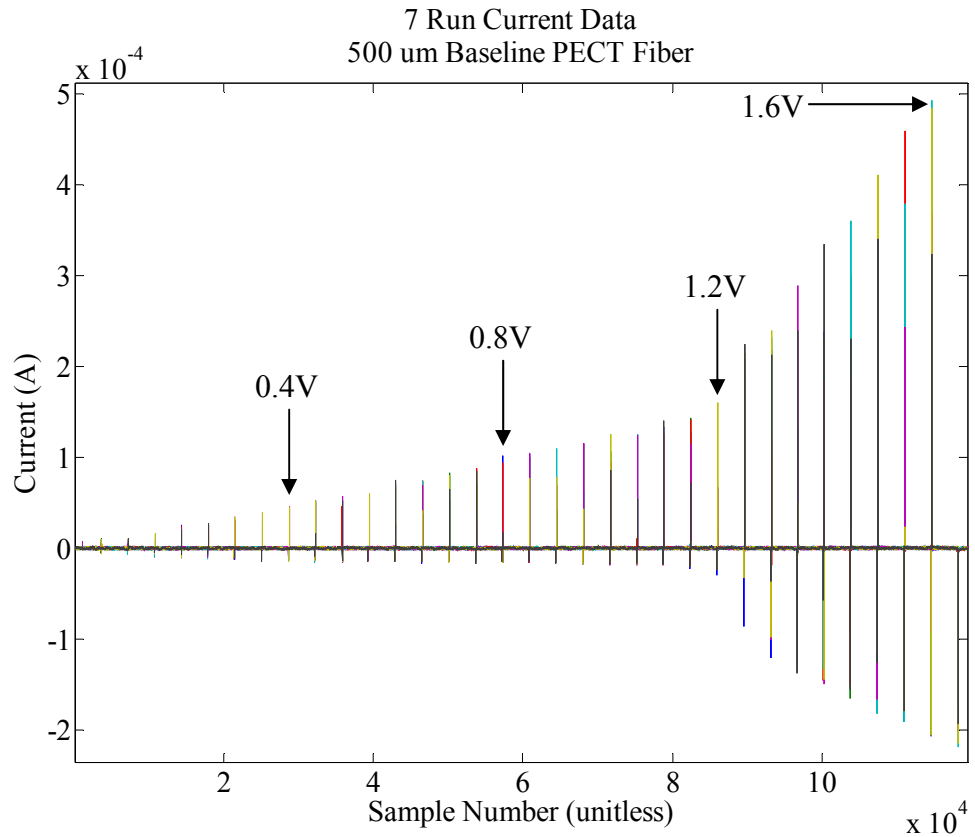
Figure 4-31: Current data for 7 run PECT repeatability series on single 500 μm carbon fiber. Each spike in current indicates a change in voltage by 0.05 V.

Figure 4-32 presents the average current data for the same 7 run series. In both cases, the general trend is an exponential increase in the current required to intercalate the carbon fiber at each voltage. The current data here also confirms that the PECT actuator is capable of a zero power holding condition, in which the stress in a fiber can be held with virtually no current flowing through the system.
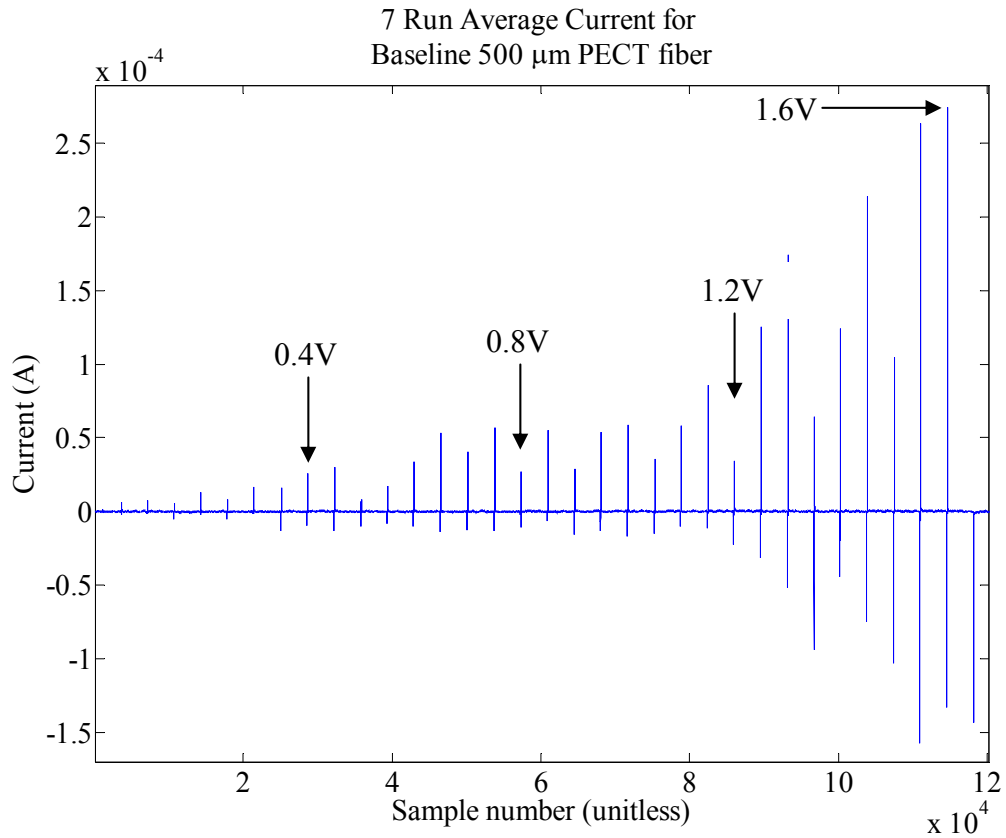
Figure 4-32: Average current for 7 run PECT repeatability series on single 500 μm carbon fiber. Each spike in current indicates a change in voltage by 0.05 V.

The average current 1.4 seconds after voltage each change stabilizes at 200 nA. Decay times, presented in Figure 4-33 show the 7 run average decay time from peak current of 174.5 μA at 1.3 V DC intercalation voltage. This decay falls to 16% of the peak value at 6.23 ms and 6.8% of the peak value at 12.46 ms after the input voltage changes. Figure 4-34 presents a 2 Hz 50% duty cycle square wave input to the same system with a lower voltage of -0.4 V and an upper voltage of 1.6 V. From this data, it is evident that the power consumption is significantly higher when this device is actuated with a signal generator, with an average holding current of 600 μA. The theoretical maximum operating frequency, to achieve 93% of the work (given by power consumption over time) at the 84% decay point is 80 Hz.

104
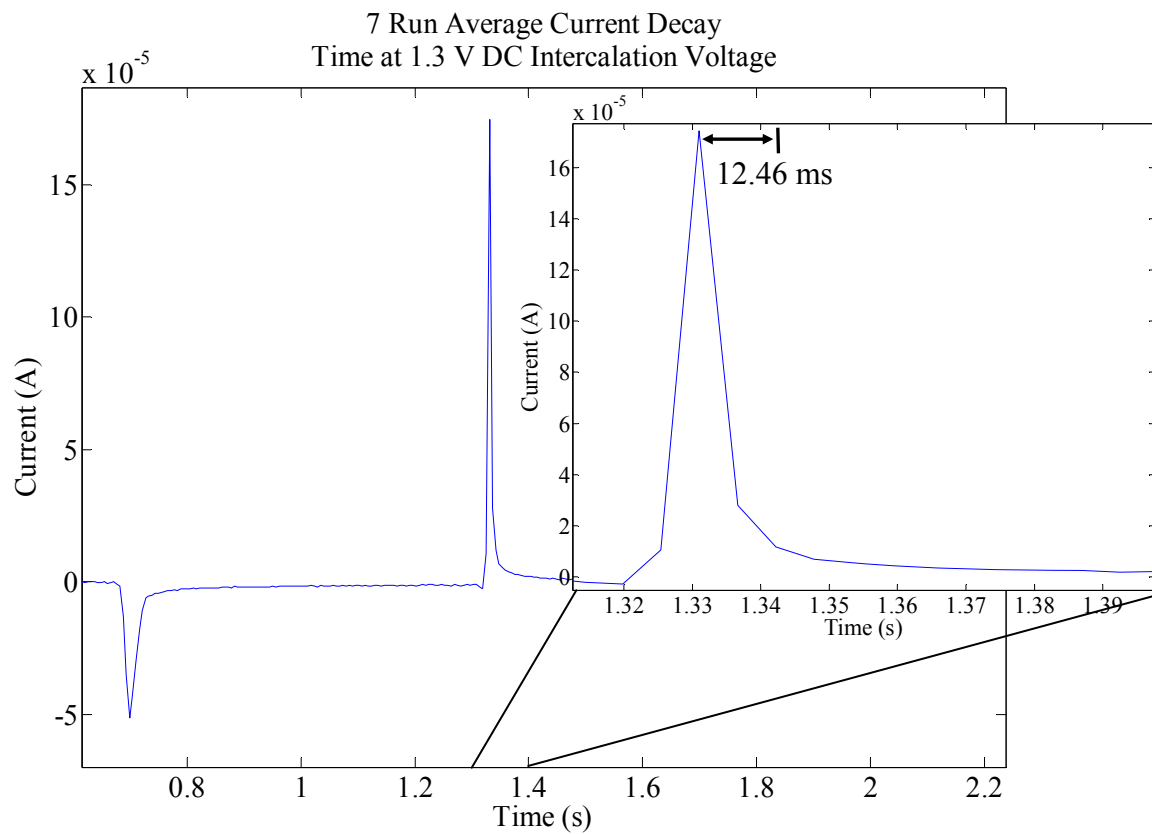
Figure 4-33: 7 run average current decay time for 1.3 volt intercalation voltage.
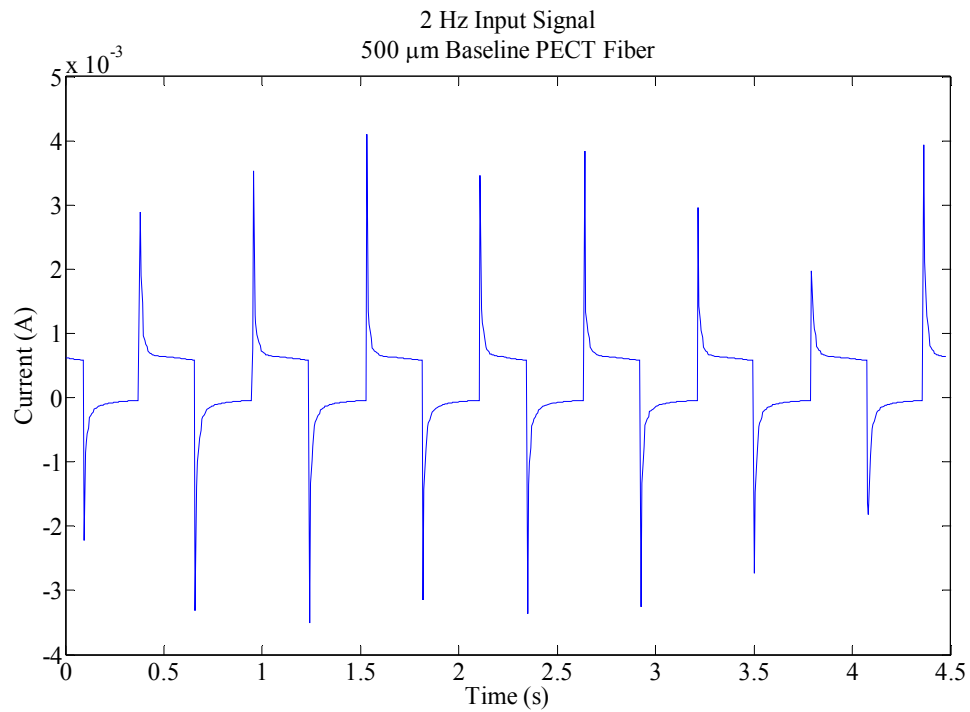
Figure 4-34: Current data for 500 μm unloaded carbon fiber tested at 2 Hz frequency.

105

4.1.9   Alternate Electrolyte

As an alternative to aqueous sulfuric acid, the Cytec Thornell® P-100 fibers were tested in a 1M aqueous solution of sodium chloride (NaCl). Ray Baughman *et al.* had success with 1M aqueous NaCl when using "buckypaper" as an actuation medium. Since Baughman's recorded strain was highest at 0.063 Hz, two measurements for each electrolysis voltage were taken [1]. In intercalation chemistry, the intercalant has the ability to intercalate from the edges of the structure at a specific rate, determined by the intercalant. Aqueous NaCl is composed of ~8 water molecules per Cl⁻ ion, and thus NaCl has a slower rate than that of H_2SO_4. Additionally, the hydrophobic graphite layers allow less ionic, more hydrophobic materials of the same size such as H_2SO_4 between the graphite layers than aqueous NaCl. Thus there is approximately a 100 fold decrease in the effective actuation time in a P-100 fiber when compared to results from H_2SO_4 experiments.

Due to the slow reaction of the NaCl solution presented by Baughman *et al.*, a measurement was taken at 10 seconds after the voltage was applied, and another at 60 seconds. Voltages were changed to the next voltage level once 60 results were recorded. Figure 4-35 presents the range at which changing strain was detected in the graphite-NaCl compound. Strain was only detected with 1, 1.2 and 1.4 V of potential applied in this experiment. Baughman presented data at 0.1 Hz showing a 0.0008 strain for the carbon nanotube paper actuator with an input square wave electrolysis voltage of ±0.5 V, whereas 1.4 V data in this research shows a response of 0.0009. While these strains are similar, the disparate voltages indicate that the carbon nanotube paper actuates slightly

better than a P-100 carbon fiber under similar conditions. The carbon fiber, however was

under load and produced 7.13 GPa of stress, which was not presented in Baughman's

research. When compared to a H_2SO_4 intercalated fiber as presented in Figure 4-36, the

performance of the NaCl intercalated P-100 fiber is an order of magnitude poorer than the

more reactive H_2SO_4.
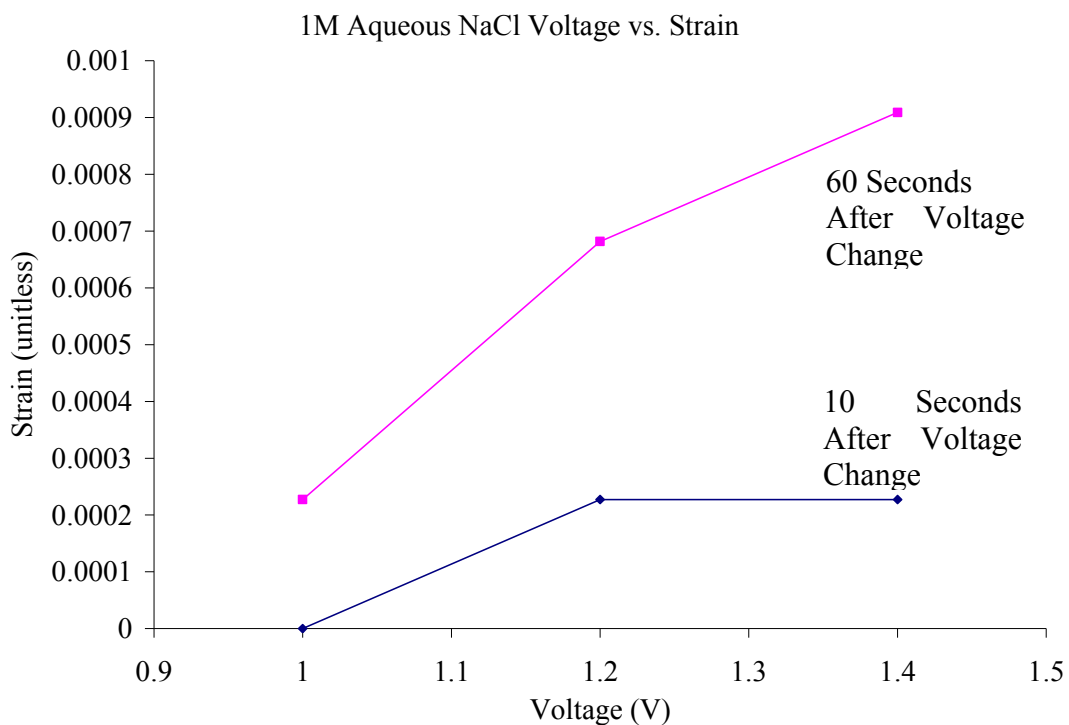
Figure 4-35: Cytec Thornell® P-100 carbon fiber actuated at 1.0 to 1.4 V electrolysis voltage in 1M aqueous NaCl.
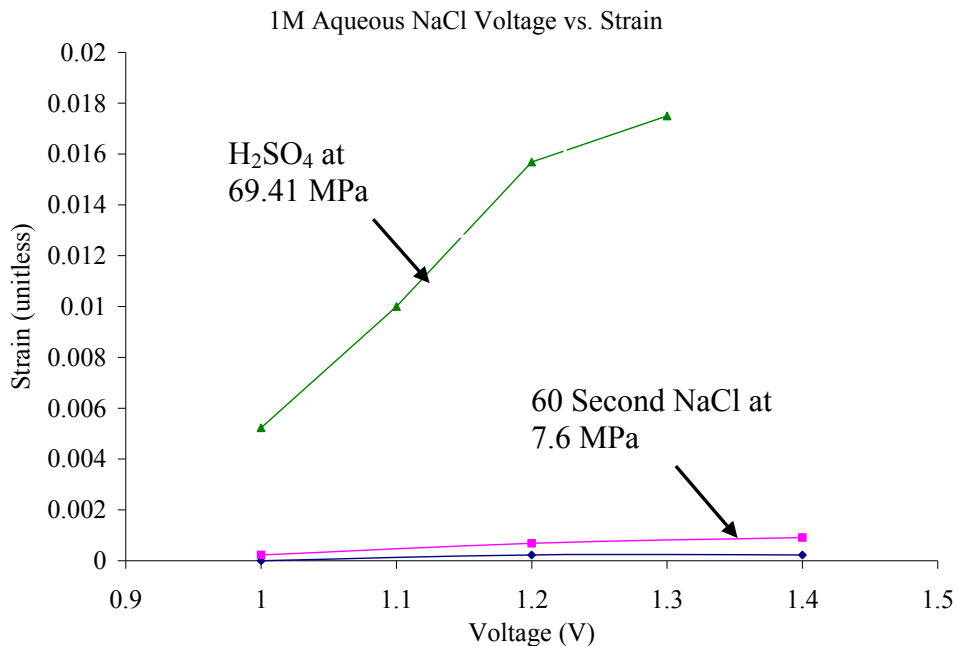
Figure 4-36: Comparison of loaded NaCl intercalated carbon fiber similarly loaded H_2SO_4 intercalated carbon fibers from 1.0 to 1.4 V DC.

4.2 Summary

This Chapter presented methods and data for an integrated actuator based on a PolyMUMPs® silicon micromachining process integrated with a Cytec Thornell® P-100 carbon fiber using aqueous H_2SO_4 and NaCl as intercalants. Experimental PECT P-100 carbon fiber actuators using H_2SO_4 as an intercalant show two orders of magnitude higher strain than piezoelectric PZT and polysilicon thermal expansion devices at the same voltages. The PECT P-100 actuators also consume as little as 440 µW during single actuation with a holding power of 320 nW, while during pulsed operation they average 5.6 mW during the first 6.3 ms of actuation and are held during the pulse at 960 µW of continuous power. In addition, these actuators exhibited up to 7.3 GPa of stress during this process. The PECT P-100 actuators using NaCl as the intercalant, under stress, produced less strain than similar tests performed by Baughman *et al*. on carbon

nanotube paper actuators in the same solution [47]. These PECT P-100 actuators also produced one order of magnitude less strain than those using H_2SO_4 as the intercalant.

Although the maximum frequency of this device is low compared to piezoelectrics and polysilicon thermal actuators, which can be actuated at a minimum of kHz frequencies, P-100 carbon fiber actuators have significant advantages over these two competitors. First, the low voltage of these devices is suitable for use in processes that integrate semiconductor electronics using the same CMOS supply voltages. Second, the high strain of PECT actuators at these low voltages shows a marked improvement of two orders of magnitude over both thermal expansion and piezoelectric actuation at a similar frequency. The PECT actuator combines the high strain and high force that would take hundreds of times the size in conventional micromachined actuators at a fraction of the total power, and given a suitable electrolyte, is a prime candidate for replacement as an actuation material in MEMS structures.

Chapter 5 will present the continuation of electrical experiments with P-100 carbon fibers. Like the devices in the current Chapter, Chapter 5 will test micro-scale devices which are fully immersed in intercalant, which will reduce measurement error that was induced during macro-scale experiments.

PIEZO-ELECTROCHEMICAL TRANSDUCER EFFECT (PECT)

INTERCALATED GRAPHITE MICRO-ELECTROMECHANICAL

ACTUATORS

5. PECT Micro-Electrical Research on Carbon Fibers

PECT carbon fibers, in addition to their changing mechanical characteristics, change their impedance characteristics with intercalation voltage. In order to more fully understand the characteristics of a fully immersed intercalated graphite fiber, some basic impedance testing on these fibers during intercalation was required. Determining the exact resistance characteristics of a fully immersed intercalated graphite fiber is critical to this understanding, as the frequency effects could limit the useful range of applications for intercalated carbon fibers as mechanical actuation mechanisms. Much of this work was performed in conjunction with an AFIT Master's student, Capt Bryan Winningham. Results from this joint work are also presented in his AFIT Masters thesis [53].

The ability of a PECT carbon fiber to transmit signals also needed to be investigated. In order to test this characteristic, the transmission line characteristics of an intercalated graphite fiber were investigated. If the results of this investigation were favorable, the intent was to develop an array implementation for use in antennas, in an addressable array that can act as a reconfigurable antenna, or addressing elements in memory applications.

5.1 PECT Impedance

In addition to the mechanical property testing, test structures to test electrical characteristics were designed and implemented. These test structures are simple adaptations of general electrical testing structures or accepted semiconductor testing

110

devices. The most accurate form of testing impedance is to develop a four terminal sensing implementation that allows a constant current to pass through two electrodes, with two more electrodes in between these current passing electrodes which sense voltage. Since this setup passes a constant current, the voltage drop on the inner electrodes can be used to calculate the impedance of the inner section of material by the resistance equation $V = IR$ where V is voltage in volts, I is current in amperes, and R is resistance in ohms.

5.1.1 Impedance Test Setup

Since the intent is to measure the impedance characteristics of a fully intercalated PECT carbon fiber as precisely as possible, Winningham initially designed a test structure in the PolyMUMPs® micromachining process that allows a fiber to be placed across two bond pads with two narrow sensing pads in between. This design, presented in Figure 5-1, incorporates four equally spaced polysilicon pads covered with gold to provide four conductive contacts for a four terminal sensing test device. The outer terminals were designed to provide good mechanical attachment to the carbon fiber and are 150 μm × 150 μm. The inner terminals were designed to minimum tolerances in the PolyMUMPs® process at a 5 μm width to reduce the length of the sensing area to more accurately predict the resistivity of the fiber.
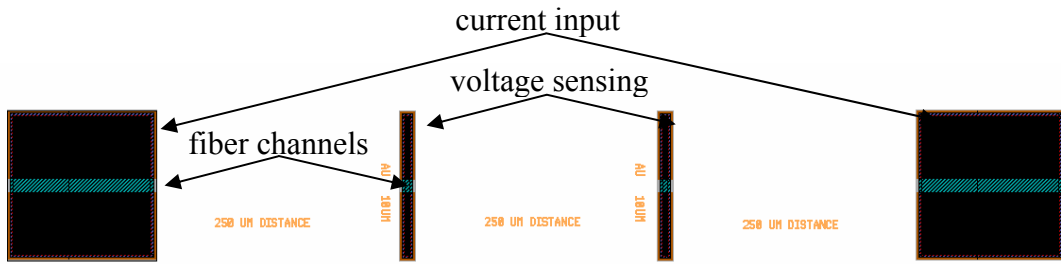
Figure 5-1: Four terminal measurement device designed by Winningham in PolyMUMPs® run 73 [53].

The Agilent model 4284a LCR (inductance, capacitance, resistance) meter uses an internal four terminal measurement to determine impedance. This impedance is based upon the model selected, either serial resistance-inductance or resistance-capacitance. The device was able to provide an impedance measurement with a signal phase output that is useful in determining crossover points between inductive and capacitive characteristics on the test material. It is also necessary, per the documentation for the 4284A, for the device to operate at least 30 minutes prior to testing for the device to provide the best results. Finally, to ensure that the LCR meter was properly calibrated prior to testing, correction routines for open and short situations were run.
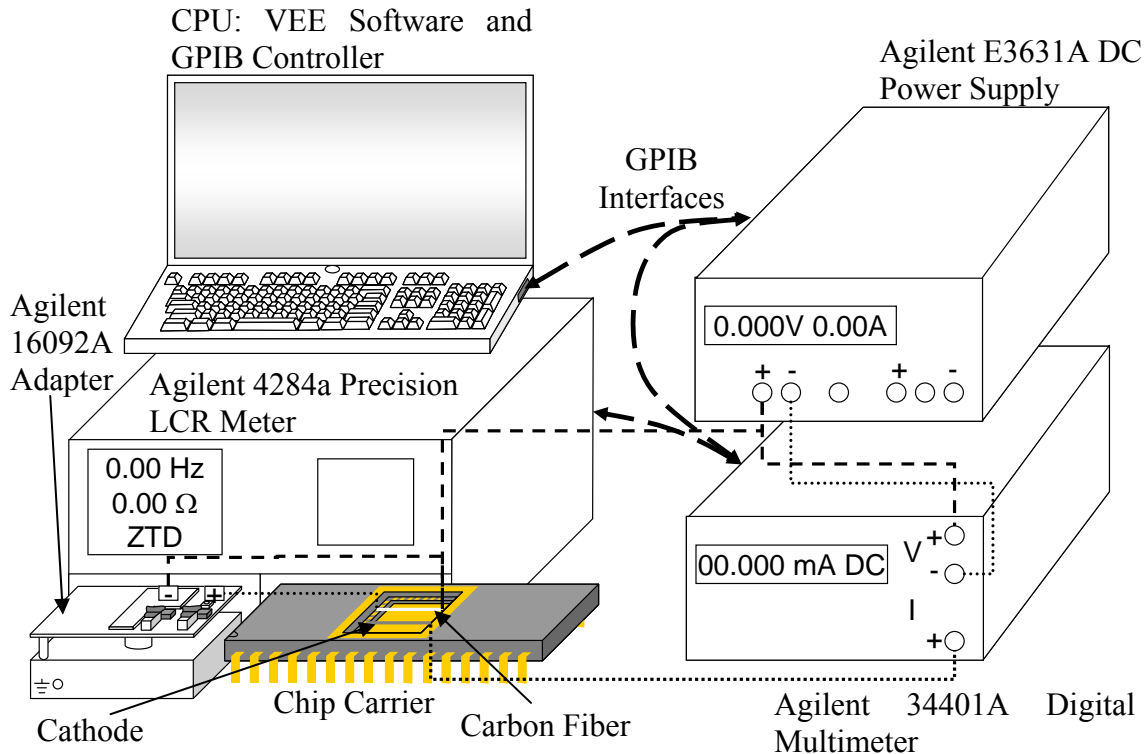
Figure 5-2: Small signal frequency response test setup to measure inductance, capacitance and resistance from Winningham [53].

The electrical test setup was modified from early experimental setups that included VEE® software programs noted in Section 3.1.1 and originally developed by AFIT interns during the course of this research. The modifications to the program allowed for Winningham to measure the impedance versus phase (ZTD), series capacitance versus series resistance (CSRS) and series inductance versus series resistance (LSRS). The program starts by applying a base intercalation voltage from the 3631A power supply and increases this voltage in steps defined by the user until the supply has reached the maximum desired intercalation voltage. At each voltage step, the 4284A LCR meter performed ZTD, CSRS and LSRS measurements from 20 Hz to 1 MHz. Winningham also modified the program to compile all data into a single file, an improvement over the previous implementation which wrote a separate file for each

measurement (ZTD, CSRS, LSRS) and for each voltage step. The modified VEE®
program allows the user to specify upper and lower voltage ranges, step sizes and allows
the user to specify the file name during operation. The setup and operation instructions
for this modified measurement setup are located in Appendix C.

5.1.2   Fiber Impedance

As a preliminary test, a single fiber was mounted across a glass slide with two
strips of 1000 Å of gold deposited using AFIT's Denton Explorer series electron beam
deposition system.   The fiber was placed on the slide and adhered between the two gold
pads with Epotek H-27D silver epoxy. The slide was then mounted on the 16092A
adapter on the Agilent 4284A precision LCR meter. This setup differs from the
experimental setup shown in Figure 5-2 in that there is no need for the voltage supply or
digital multimeter since the carbon fiber was not in an electrolytic solution. Figure 5-3
presents the setup used for this baseline dry fiber experiment.
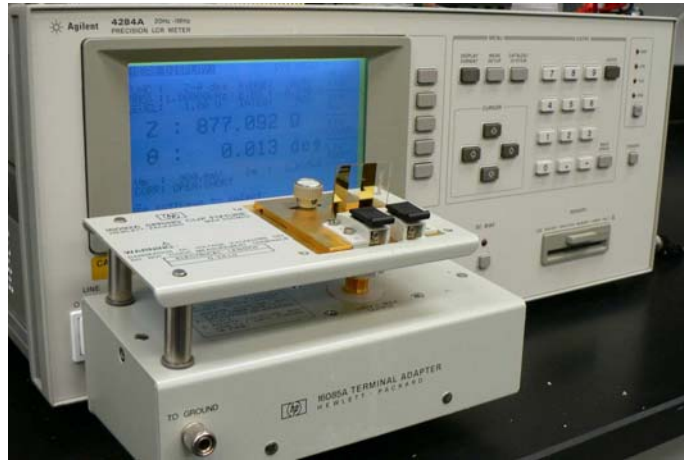
Figure 5-3: Dry-run measurement setup on Agilent 4284A precision LCR meter using
Thornell® P-100 fiber suspended between two gold metallized contacts on a glass slide.
Note that gold is facing LCR meter screen to make contact with metal electrodes on the
terminal adapter [53].

The Agilent 4284A precision LCR meter determines the values for capacitance, inductance, and resistance using the total impedance (Z) and phase (θ) measured at each frequency. These two values allow the LCR meter to derive the resistance (R), reactance (X), inductance (L) and capacitance (C). The values for inductance, resistance and capacitance are governed by:

$$|X| = \sqrt{R^2 + Z^2} \ (\Omega), \tag{5.1}$$

$$R = \frac{Z}{\sqrt{1 + \tan\theta^2}} \ (\Omega), \tag{5.2}$$

$$C = \frac{1}{2\pi X_C f} \ (\text{F}), \tag{5.3}$$

$$L = \frac{X_L}{2\pi f} \ (\text{H}). \tag{5.4}$$

The values X_C and X_L, the capacitive and inductive components of X, are determined by the sign of the phase angle. When the phase is positive, the capacitive component is greater than the inductive, and vice-versa when the phase is negative. Internal capacitances and inductances react with one another and affect the phase of the circuit. At resonance, these interactions cancel each other out, resulting in a phase crossing through zero. When this happens, the geometry of the circuit determines impedance. If the RLC circuit is parallel, impedance will be at a maximum at these phase crossing points, and if it is a series circuit, the impedance will be at a minimum at these points [53,54]. Following the dry run, several successfully mounted fibers were tested to determine the changes induced by intercalation in the carbon fibers.

5.1.2.1   *Dry Run Impedance Results*

Since the dry run results are effectively a baseline measurement for the fiber, it is useful to determine how close one can measure the characteristics of the dry fiber when compared to the manufacturer's specifications. In this case, Cytec states that the Thornell® P-100 fibers have a 2.5 $\mu\Omega$-m resistivity [55]. One can conclude from these measurements, taking into account the specified cross-sectional area of the fiber, that resistivity in the P-100 sample fiber is 2.74 $\mu\Omega$-m, which is very close to the fiber specifications [53]. Figure 5-4 presents data acquired for the dry run of this P-100 fiber. Since the fiber crosses the zero phase line at two points, between 20-50 Hz and 150-200 kHz, one can note that a parallel or series circuit would result in either minimum or maximum impedance at these points which is not evident in this resistivity data. Winningham cites two possible causes, first that the phase may be so small that capacitance and resistance play a negligible role in impedance and second, and possibly more likely, that the circuit is composed of an amalgam of parallel and series circuits that cause the final circuit to behave in an unidentifiable manner [53].
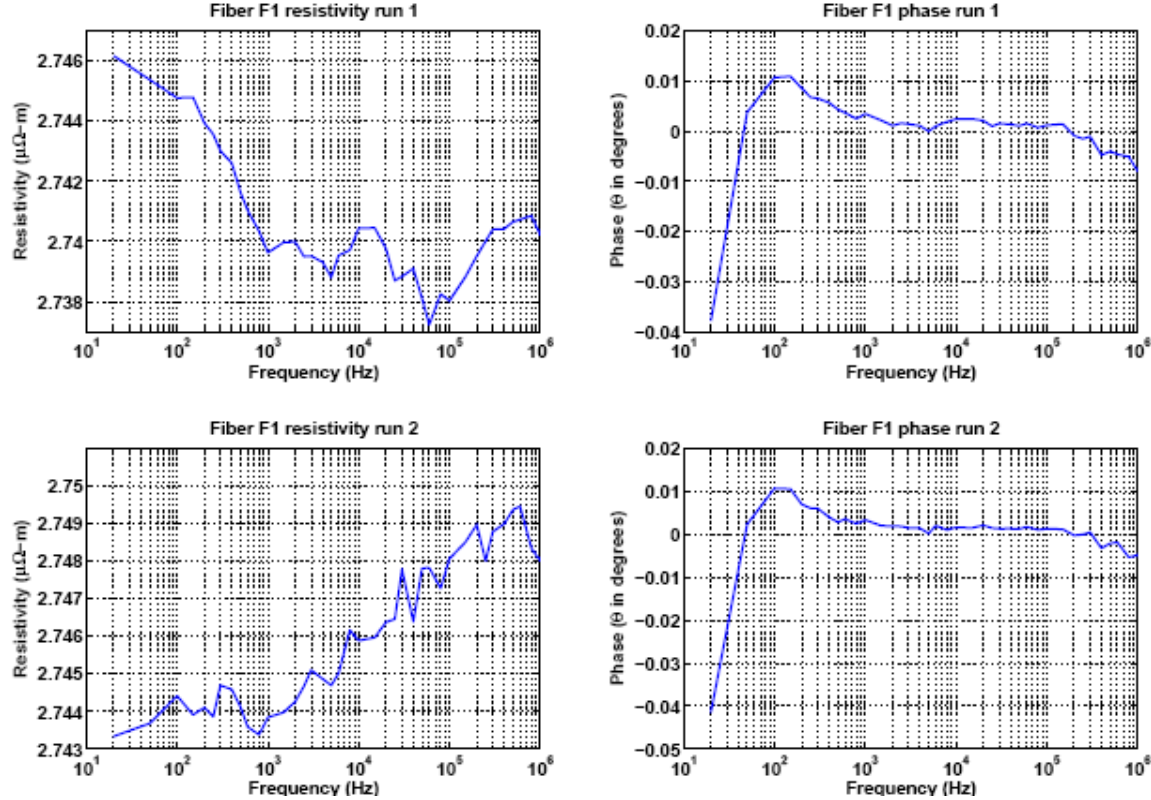
Figure 5-4: Results of dry-run LCR meter impedance measurements for P-100 fiber mounted on glass slide directly contacting 16092A test fixture [53].

To determine the resistivity, ρ, the standard resistance equation:

$$R = \frac{\rho L}{A} \ (\Omega) \tag{5.5}$$

can be used. R is the resistance of the fiber, length is L and A is the crossectional area of the fiber given by multiplying π by the squared fiber radius. Manipulating Equation 5.5 to solve for resistivity results in:

$$\rho = \frac{RA}{L} \ (\Omega\text{-m}). \tag{5.6}$$

5.1.2.2 *Intercalated Fiber Results*

Following the dry run results, a fiber was tested during intercalation in H_2SO_4. The phase over the range of frequencies from 20 Hz to 1 MHz and intercalation voltages

117

from 0 to 1.4 V was plotted. Note that the phase of the intercalated P-100 fiber no longer crosses through zero, indicating that there are no local minima or maxima and that a resonance frequency of the system is never reached during intercalation. Figure 5-5 presents the phase surface profile for the single P-100 fiber tested during intercalation.
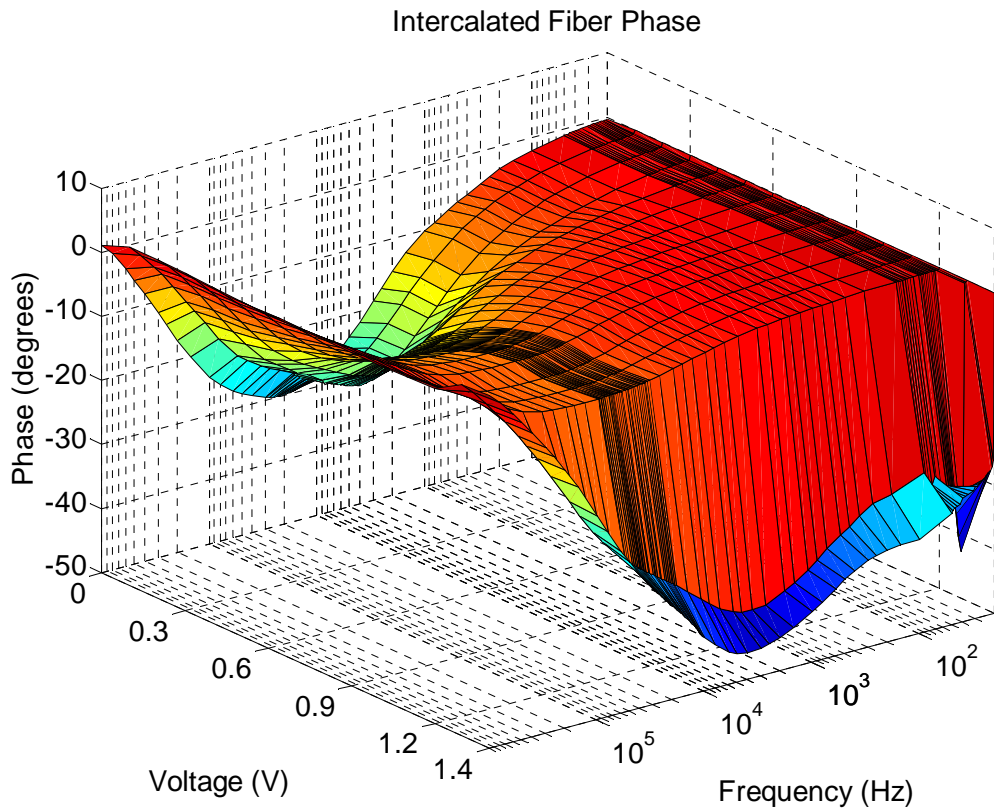
Figure 5-5: Phase profile of intercalated carbon fiber during LCR meter impedance testing from 20 Hz to 1 MHz and 0.0 to 1.4 V of intercalation voltage.

The resistivity changes were plotted during the intercalation process. At all frequencies, increased intercalation voltages from 0.0 to 1.2 V caused a reduction in resistivity. At 1.3 V intercalation voltage, the resistivity begins to increase again and dramatically rises at 1.4 V DC. Intercalated resistivity matches dry fiber resistivity,

however, only at the higher frequencies. Figure 5-6 presents the resistivity profile from 0.0 to 1.4 V intercalation voltage and 20 Hz to 1MHz in frequency.
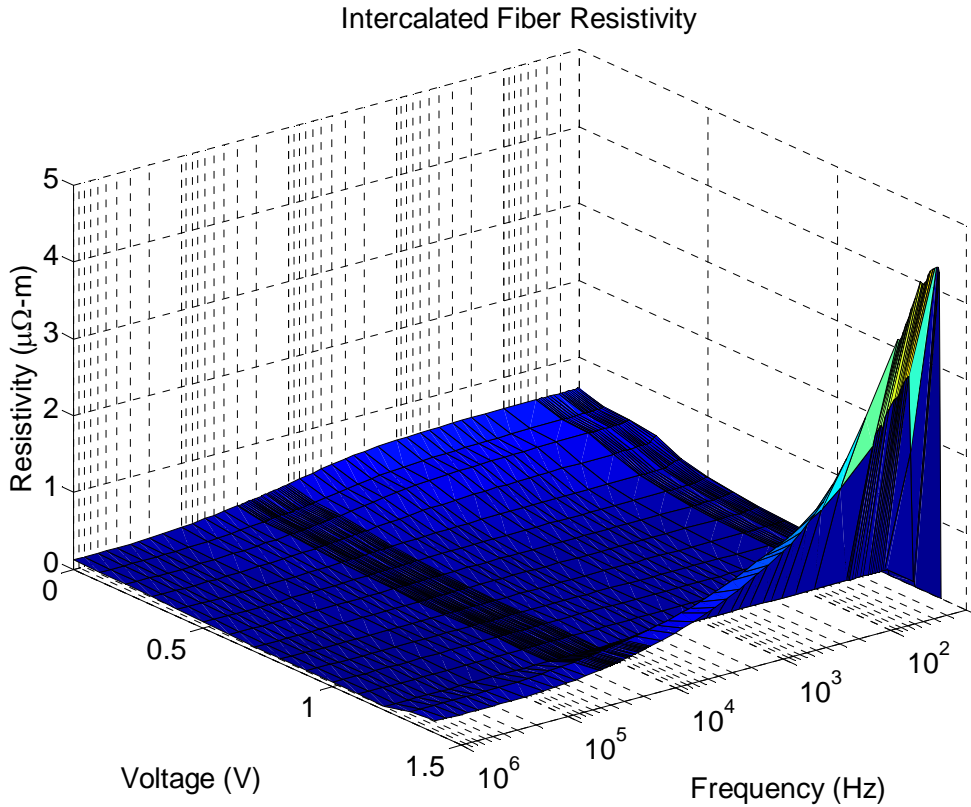
Figure 5-6: Resistivity of intercalated carbon fiber from 0.0 V to 1.4 V DC intercalation voltage and over a range of frequencies from 20 Hz to 1 MHz.

5.2 Coplanar Waveguide

In addition to general electrical characteristics of the P-100 fiber, the transmission line characteristics of an intercalated graphite fiber were investigated. Since much testing has been accomplished by the Air Force Research Laboratory on the transmission line characteristics in silicon and gallium arsenide, a structure that would accommodate comparison between those two materials and the PECT measurements for transmission line characteristics was fabricated. This measurement device is a coplanar waveguide

(CPW). Two strips of metal flank a single intercalated graphite fiber to measure the signal transmitted by the intercalated graphite transmission line. Design specifications were obtained from Mr. Tony Quach at the Air Force Research Laboratory Sensors Directorate and are presented in Figure 5-7. A test structure following this design was submitted for PolyMUMPs® runs 71 and 72 and is presented in Figure 5-8. Although the test structure was designed incorrectly due to a misinterpretation of the AFRL specifications, it was sufficient for the AFRL Sensors Directorate to test the transmission characteristics of the P-100 fiber. In this case, the ground conductor is the carbon fiber and the blue portion is the ground plane.
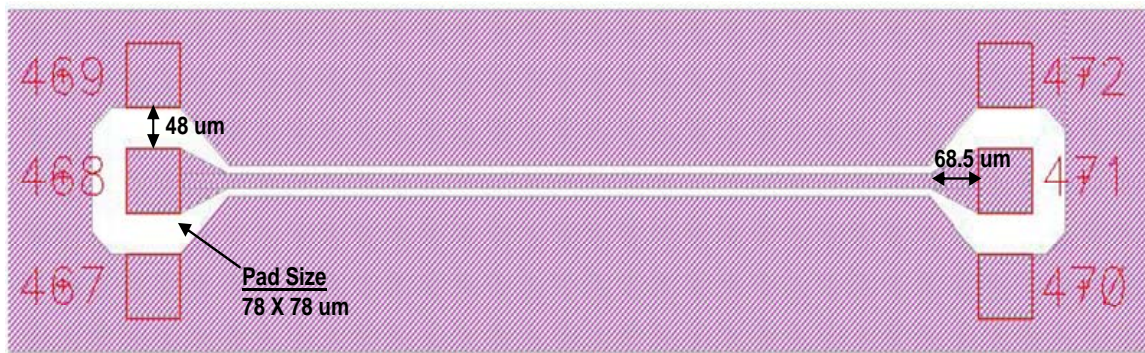
Figure 5-7 Air Force Research Laboratory CPW test structure specifications for use with a 10 μm diameter intercalated graphite fiber.
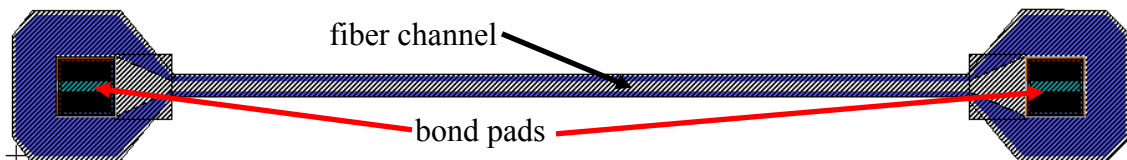
Figure 5-8: PolyMUMPs® runs 71 and 72 CPW design.

The typical waveguide structure is matched to a 50 Ω impedance value. This value is commonly used in coaxial cables and numerous antenna input applications. As

120

such, the coplanar waveguide testing stations typically use a 50 Ω input impedance to test devices. AFRL's Sensors Directorate tested the PECT fabricated CPW structure using a Cascade Microtech on-wafer probe station and an HP 8510B vector network analyzer to evaluate the carbon fiber CPW structure.

The 50 Ω transmission line tests produce what are referred to as *S*-Parameters. These parameters are S_{11} and S_{22}, which are the input and output reflection coefficients at 50 Ω, and S_{12} and S_{21}, which are the reverse and forward transmission coefficients, respectively. For a transmission line, $S_{11}=S_{22}$ and $S_{12}=S_{21}$ due to symmetry. A good transmission line would be matched to the typical input impedance of 50 Ω. There are other impedances; however, the real impedance will definitely require different circuitry to properly implement if it deviates from the 50 Ω standard values. The classical telegrapher's transmission line equation can determine the characteristic impedance (Z_0) from the *S*-parameter:

$$Z_0 = 50\sqrt{\frac{(1+S_{11})^2 - S_{21}^2}{(1-S_{11})^2 - S_{21}^2}} \ (\Omega) \ [56].$$

(5.7)

Figure 5-9 presents the real portion impedance values for a two-run test series at frequencies ranging from 100 MHz to 20 GHz. Compare this data to the impedance of an unmatched CPW structure presented in Figure 5-10 [57].
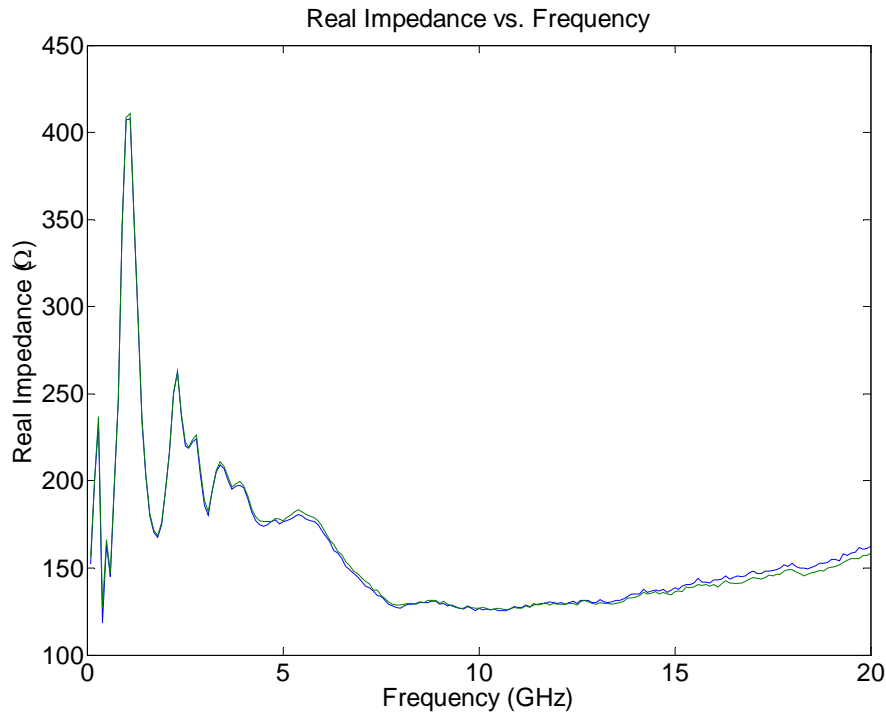
Figure 5-9: Real impedance for two-run test of carbon fiber CPW structure from 100 MHz to 20 GHz.
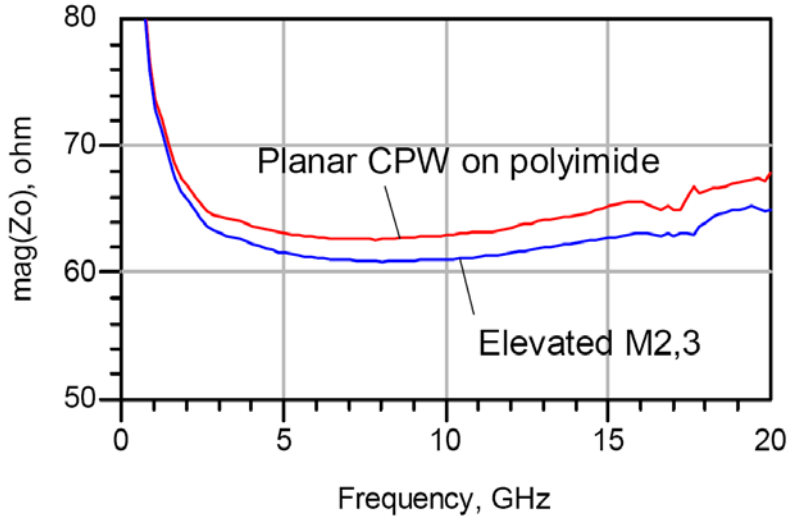
Figure 5-10: Measured impedance for 2 poorly matched CPW designs on a GaAs substrate [57].

When comparing these two graphs, note that the general shapes of the results are very similar, disregarding the larger variations and looking at the general trend in the

122

data. The large difference shows in the disparate y-axis scales. The CPW structure

designed with the carbon fiber more closely matches a 150 Ω structure than the standard

50 Ω structure. As such, in normal applications this CPW will not be useful. This

uselessness can be demonstrated by the loss that the structure exhibits due to standing

waves caused by a high reflectance coefficient, S_{11}, and the mismatch in impedance to the

test device as presented in Figure 5-11. This value is calculated by dividing a two-port

network reflected power from the input of $1-|S_{11}|^2$ and an approximation of the output

power of $|S_{21}|^2$. The approximated dissipation loss is then given by:

$$Loss = 10 \times \log\left(\frac{1-|S_{11}|^2}{|S_{11}|^2}\right) \text{ (dB)}. \tag{5.8}$$
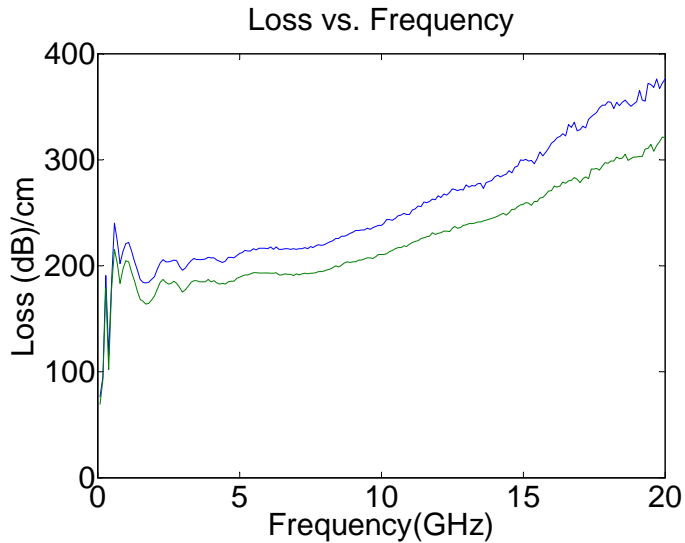
Figure 5-11: Loss per centimeter of CPW structure as a function of signal input frequency low and high values in two-run test.

Clearly this structure is unsuitable for a 50 Ω input device as a transmission line

material. As such, it would be unlikely to use this material to integrate radio frequency

components into microelectronics or MEMS applications. Additionally, this device was not tested while intercalated since the intercalation solutions used are aqueous and would cause the CPW transmission line parameters to be inconclusive. The results would be more a function of the solution than of the material itself.

5.3 8 × 8 Fiber Matrix

The final electrical test structure designed, using the PolyMUMPs® process in run 71 is an 8 × 8 matrix of graphite fibers. Individual biasing may be accomplished to intercalate each fiber, and potentially pass a signal from a row fiber to a column fiber and vice-versa. Extending this research would be the ability to coat this array with a thermally active material such as calcogenides that change state when temperature is applied. With individually addressable fibers, it would be possible to change a single location of this material through resistive heating at the junction. A simple 8 × 8 test structure was designed for PolyMUMPs® run 71 for initial testing of this theory. Figure 5-12 presents the design for this array. Horizontal channels were etched into the substrate to sink the horizontal fibers enough for the top of the fiber to be adjacent to the bottom of the vertical fibers. Additional post-fabrication etching was required to complete etching to a depth of 10 μm beneath the bottom of the vertical contact bond pads. A layer of nitride was then deposited in these channels to isolate the fibers from the substrate and the fibers were metallized with gold for contact to the external container for this device.

After reviewing the CPW results which characterized the performance of a carbon fiber transmission line, fabrication and testing on this structure were halted as a matrix implementation was rendered unsuitable by those results.
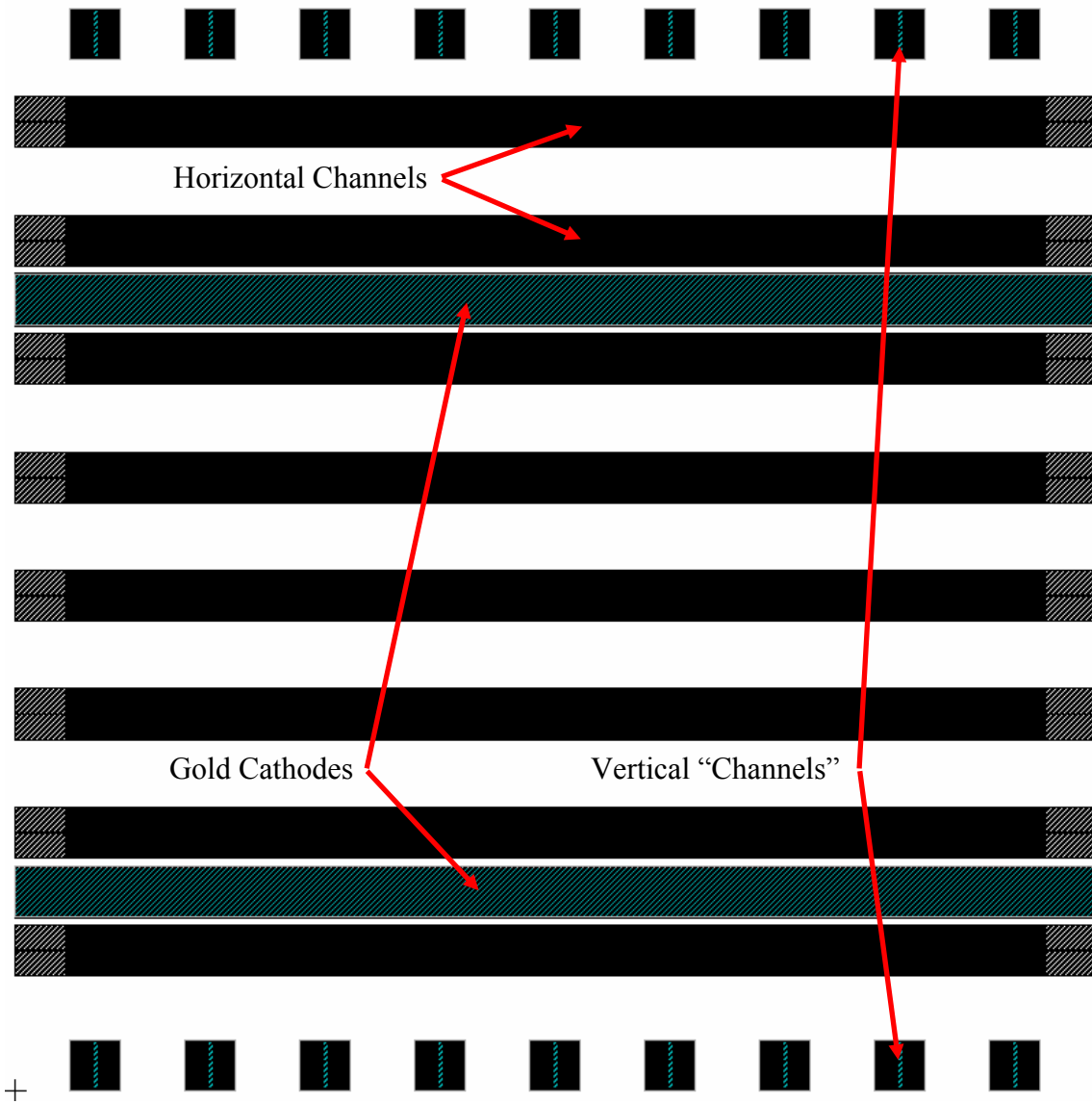
Figure 5-12: 8 by 8 fiber matrix design submitted for PolyMUMPs® run 71.

5.4 Summary

This Chapter investigated the electrical performance of PECT-based intercalated carbon fibers. These results included resistivity and phase associated with the measurement of impedance values for the fiber as well as the transmission line characteristics as evaluated in a CPW test structure. The results of this data confirm that

the intercalated carbon fibers act in the same general way as other forms of intercalated graphite presented in Section 1.3 of this dissertation. The transmission line characteristics, specifically high impedance, were unsuitable for normal 50 Ω applications and this pre-empted the concluding 8×8 matrix structure initially envisioned as a use for the electrical aspects of intercalated carbon fibers. Although the use of carbon fibers as a conducting medium is impractical, the data reviewed in this Chapter is critical to compare to thin-film graphite intercalation compounds for use in MEMS and microelectronics applications. Chapter 6 of this dissertation presents the fabrication and electrical and mechanical testing of highly oriented pyrolytic graphite thin-film structures.

PIEZO-ELECTROCHEMICAL TRANSDUCER EFFECT (PECT)

INTERCALATED GRAPHITE MICRO-ELECTROMECHANICAL

ACTUATORS

6.   Highly Oriented Pyrolytic Graphite Research

A practical mainstream application of carbon fiber actuators as the driving mechanism in next-generation MEMS devices is unlikely due to the complexity of integration into standard MEMS structural components. The intent of this research was to show the usefulness of the PECT effect in graphitic carbon as an actuation material for MEMS devices. Unfortunately, if devices are restricted to carbon fibers only, that usefulness is overcome by the difficulty in integrating the two disparate materials. Were carbon fibers the only alternative for PECT devices, only small-scale laboratory devices could be fabricated, as large-scale, whole-wafer integration would be too time-consuming to accomplish. Given enough time and resources, however, it would be possible to create a machine that could place several fibers onto a wafer in specific locations during the fabrication process.

Fortunately, there are alternative graphitic materials that can be investigated for use with the PECT effect. As previously stated, HOPG is a highly oriented form of polycrystalline graphite. The crystallites are large enough and oriented closely enough with one another that the HOPG can be used as a thin film, even though it is not deposited on the surface of the substrate material. The HOPG sample obtained from AFRL/ML is manufactured using chemical vapor deposition at elevated temperatures (up to 3000 °C). The resultant commercially provided sample of HOPG is approximately 1 cm square with a 5 mm thickness. This material is what can be used to simulate

deposited thin film graphite, and attached to a PolyMUMPs® mechanical base. This Chapter describes the processes used to create thin-film HOPG structures and presents the results of the electrical and mechanical tests conducted on those thin-film structures.

6.1 Integrating HOPG and PolyMUMPs® Die

In order to integrate HOPG with a PolyMUMPs® die, it was first necessary to develop a thin film process that was compatible with both materials. HOPG is very stiff along the a-plane of the structure and has relatively weak van der Waals forces holding these planes together. These attributes allow simulation of a thin film, and ultimately integration of this thin film with semiconductor manufacturing processes.

6.1.1 Creating Thin-film Graphite From HOPG

Leveraging the material aspects of the graphite allows the development of a method for thin film simulation using the HOPG samples. The weak inter-planar forces in the graphite allow, as stated in Section 1.2.3 , a subset of the block of HOPG to be cleaved from the bulk of the block using common household tape as presented in Figure 6-1. The thickness of these layers is inconsistent between successive cleaving using the same block of HOPG, but it is possible to continue cleaving until the resultant sample is below a maximum thickness threshold. It is also important to note that the crystallites also fracture in the plane somewhat, causing discontinuities in the surface planar structure and thus a slightly irregular surface topology as presented in Figure 6-2. The height difference, given even 100 planes difference, is only in the tens of nm and is at least an order of magnitude lower than the thicknesses of the structures created during this effort and thus inconsequential.
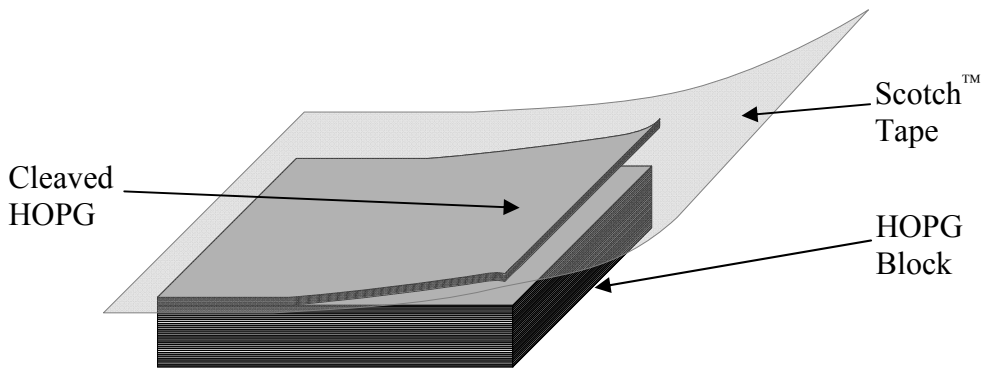
Figure 6-1: Graphical example of cleaving thin sheets of HOPG from original block of HOPG.

Using household tape to cleave the surface of the HOPG did leave one major outstanding question: How can the HOPG be removed from the tape and placed onto the PolyMUMPs® die? There is a simple solution to this problem which involves spinning a thin layer of MicroChem Shipley 1818 photoresist onto a piece of silicon wafer, but not curing the surface. At this point, the surface of the photoresist has roughly the same tackiness as the surface of the tape. Pressing the HOPG sample that has been cleaved from the block of HOPG, it is possible to cleave a portion of that first cleaving onto the photoresist as presented in Figure 6-2. At this point, the photoresist is cured at 110 °C for 75 seconds on a hotplate to harden the resist and make it less likely for the resist to peel off during successive cleavings. Once cured, the height between the HOPG and the top of the photoresist was measured to obtain an approximate thickness of the HOPG layer. The process was repeated until the thickness of the HOPG was under 1 μm.
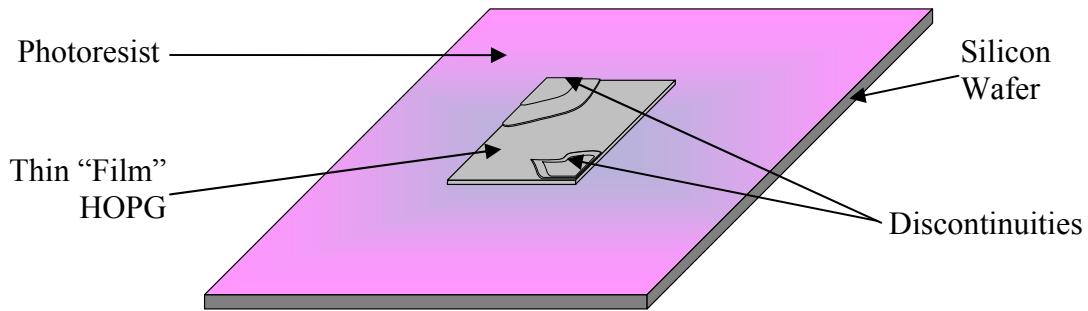
Figure 6-2: Cleaved HOPG sample after thinning to desired thickness on photoresist covered silicon wafer section.

At this point, the wafer was rinsed in acetone to remove any uncovered photoresist, and then immersed the die in acetone for 60 minutes to gradually remove the layer of 1818 photoresist between the silicon wafer and the HOPG. The very long soak in acetone was to ensure that the photoresist was removed under the entire 1 cm square piece of HOPG. Later, the speed of the delamination process was increased with the application of a low flow stream of acetone from a spray bottle. Once the photoresist was completely dissolved, the silicon wafer section was removed and irregularly shaped portions of the cleaved HOPG sample remained suspended in acetone. The pieces of HOPG were so thin, that they floated well in the acetone, but any attempt to remove them from the solution caused the surface tension of the solution to fold them in upon themselves.

In order to place the suspended HOPG flakes onto the PolyMUMPs® die, the die was placed in the acetone solution with the flakes. The flakes were gently maneuvered over the surface of the PolyMUMPs® die and the die was slowly raised of the solution to keep the HOPG in place. Once the die was out of the solution, a few drops of isopropyl alcohol were deposited onto the surface to drive out the acetone and clean the surface. The isopropyl alcohol was then left to dry and partially conformal thin film graphite

remained on top of the polysilicon structures. Figure 6-3 presents a PolyMUMPs® die with an irregular HOPG sample adhered to the surface using surface tension as an adhesion mechanism.
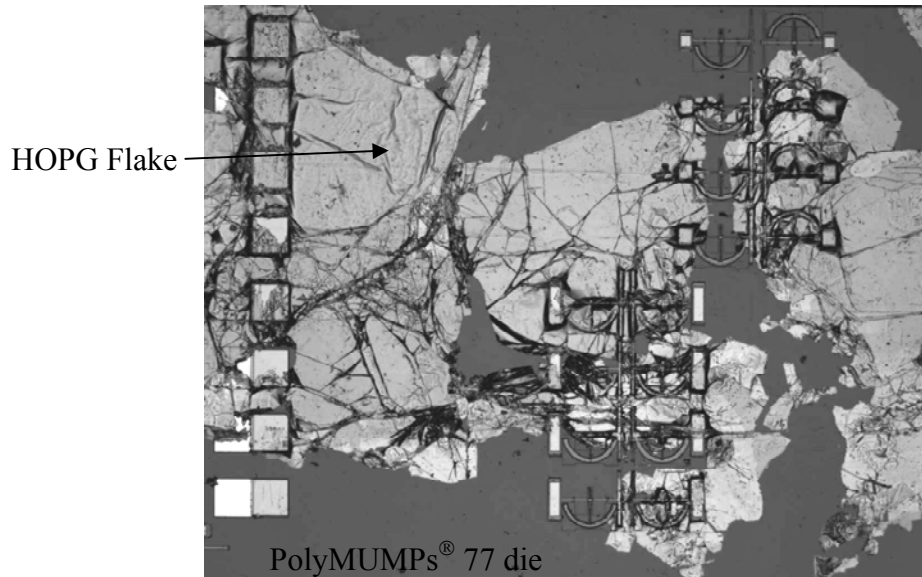
Figure 6-3: HOPG thin film flake adhered to the top of a PolyMUMPs® 77 die using surface tension.

6.1.1.1 HOPG Patterning

A mask was fabricated to be able to create a photolithography pattern on the surface of the HOPG. MicroChem's 3350 positive photoresist, which yielded a 4.5 μm thick layer of photoresist on the surface after spinning at 4000 RPM for 30 seconds, was used. The photoresist was soft baked for 75 seconds at 110 °C, and exposed for 20 seconds at 275 W output power on a Karl Süss MA-6 mask aligner as shown in Figure 6-4. After exposure, the samples were removed from the mask aligner and the photoresist was developed for 1 minute in 300 MIF deveoper, rinsed in deionized water for one minute, and dried with nitrogen gas. The patterns left by this photolithography

131

were adequate for subsequent processing steps, even though proximity exposure was used to prevent the graphite/photoresist combination from delaminating from the PolyMUMPs® die onto the mask. Figure 6-5 presents a developed photoresist pattern on a PolyMUMPs® die.

Figure 6-4: Karl Süss MA-6 mask aligner used to pattern 3350 photoresist on PolyMUMPs® die.

6.1.1.2 *HOPG Actuator Formation*

In order to form any useful structures, it was necessary to etch away the unwanted HOPG from the areas around the intended actuators. HOPG can easily be etched in oxygen plasma, thus two options were evaluated for etching: an oxygen plasma asher, and an oxygen plasma reactive ion etching (RIE) machine. The first attempt at etching the graphite used the less complicated oxygen plasma asher, which produced poor results. The surface of the graphite was pitted and irregular, and the rate of etch was insufficient to provide a good mechanical device. Figure 6-6 presents the results of a 10 minute etch

in an LFE Plasma Systems series 100 Barrel Plasma Asher at 500 sccm of O_2 gas, chamber pressure of 10 mTorr and with a 200 V forward and 2 V reflected bias.
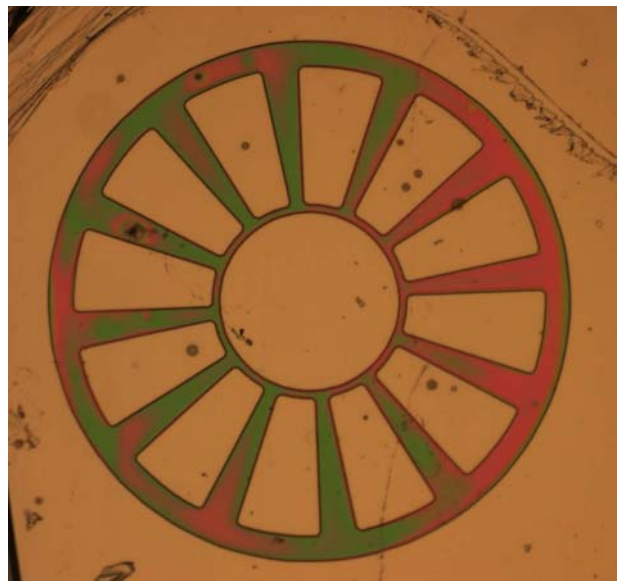
Figure 6-5: Photoresist pattern on HOPG thin film application to PolyMUMPs® die.

Figure 6-6: Oxygen plasma ashed HOPG sample after 10 minute etch.

Oxygen plasma ashing was not sufficient to produce a usable device. As such, the second option, a Unaxis Plasma-Therm 790 series RIE machine, was used. Much like the oxygen plasma asher, the RIE machine produces a plasma in a low pressure environment using electrical power to charge the oxygen gas into a plasma and accelerate O^+ ions toward the sample with a DC voltage bias. The Unaxis Plasma-Therm 790 system presented in Figure 6-7 etched approximately 15 nm/min of HOPG with an O_2 gas flow rate of 100 standard cubic centimeters per minute, 20 mTorr chamber pressure, 200 W applied power and 526 V DC bias between the plasma and the sample. The first sample that was etched required 35, the second 10, and the third 30 minutes of etching time, due to the varying thicknesses of the HOPG layers of each sample.

Sample Chamber
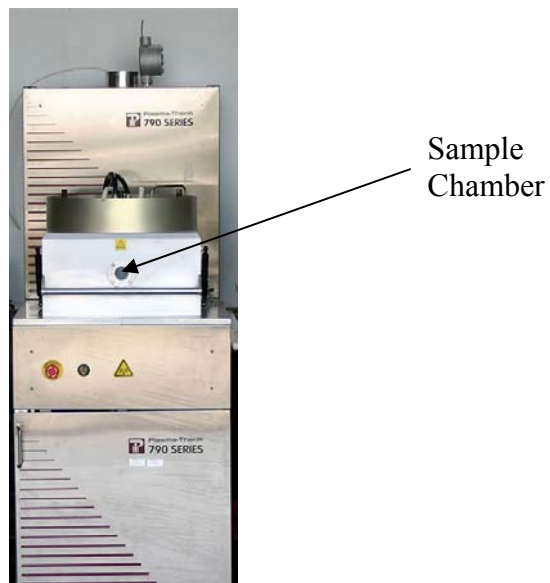
Figure 6-7: Unaxis Plasma-Therm 790 RIE unit used to etch HOPG samples in O_2 plasma.

The result of this O_2 plasma RIE was a well defined structure that was very thin ~150 nm stretched across the underlying polysilicon structures. The final patterned device is presented in Figure 6-8. Once the HOPG strip was formed, a 0.8 μm thick 7

μm × 12 μm patch of Pt using the Nova Nanolab 600 system previously presented in Figure 4-17, was used to attach each end of the HOPG strip to the polysilicon structure under it. An image of the final HOPG strip with the FIB deposited platinum patch, at a higher magnification, is presented in Figure 6-9. In the case of the HOPG, the platform was tilted to 52° of inclination to provide a normal incident angle for platinum deposition over the HOPG.
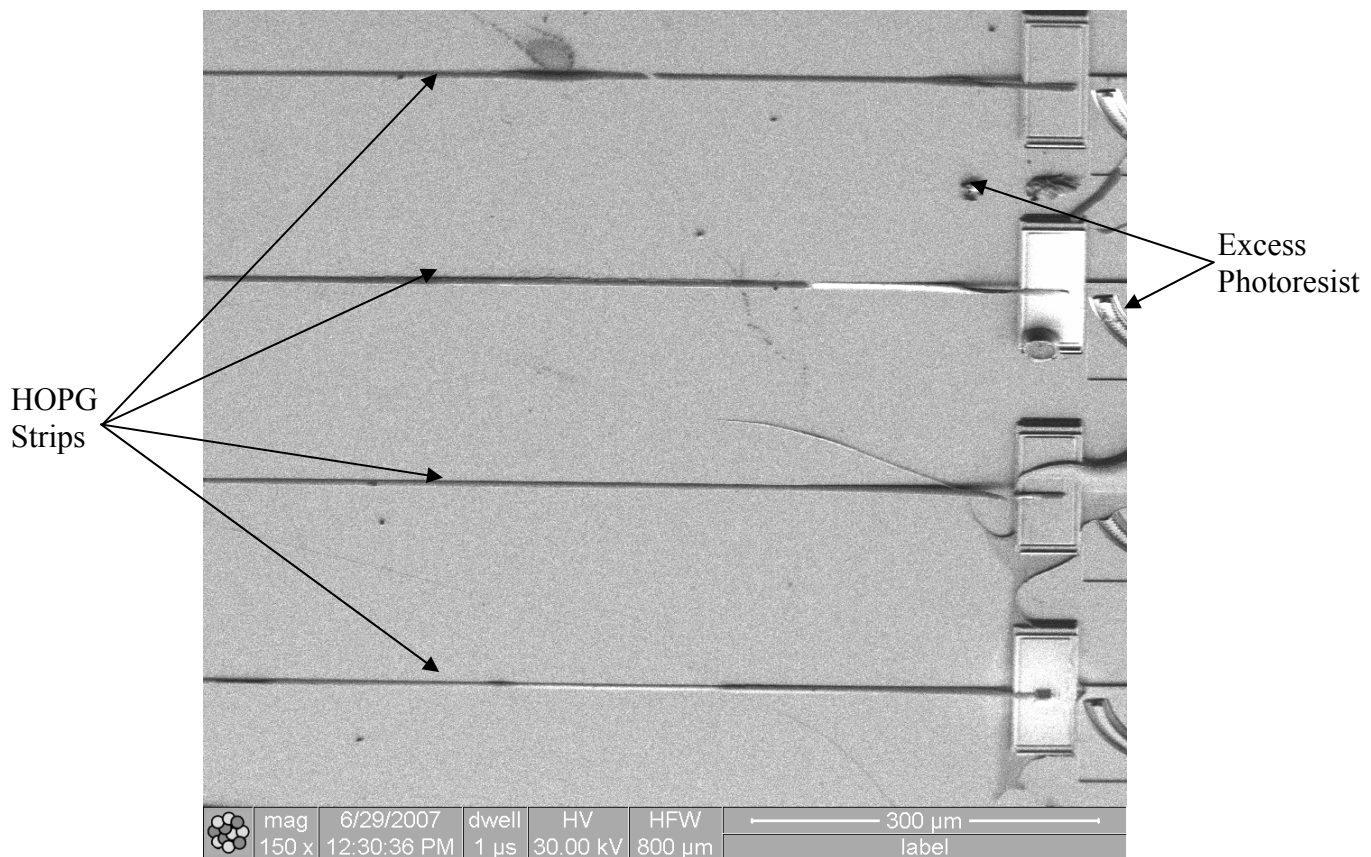
Figure 6-8: Patterned 10 μm HOPG strips after RIE in Unaxis Plasma-Therm 790 RIE unit.
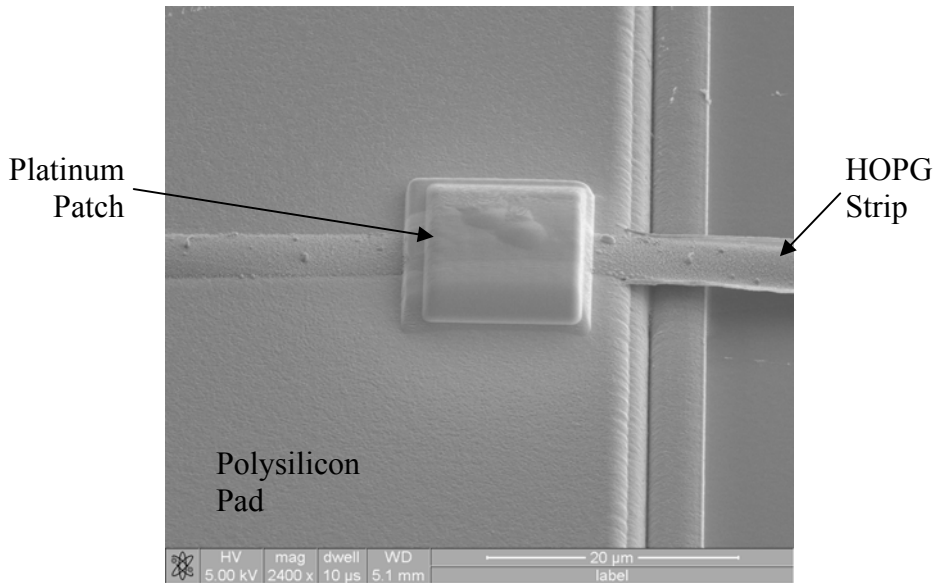
Figure 6-9: Platinum patch connecting thin HOPG actuator strip to polysilicon pad beneath the HOPG strip.

It was necessary to attach the HOPG to the polysilicon structure prior to removing excess photoresist to prevent any of the patterned HOPG from washing off of the die. Following the platinum deposition, the die was soaked in acetone for 60 minutes, which was more than the time necessary to remove the thickness of photoresist used during patterning, to remove any remaining photoresist. The device was then released by submersion in 96% HF for 5 minutes followed by 10 minutes in deionized water, 10 minutes in isopropyl alcohol and a 15 minute bake at 110 °C on a hotplate to prevent surface stiction due to the surface tension of drying liquids. The final released sample was then mounted in a 40-pin dual-inline package chip carrier, wire-bonded and encapsulated using the same method previously described in section 4.1.6 .

6.1.1.3   *Forming HOPG Impedance Test Structures*

Testing the electrical characteristics of intercalated HOPG in comparison to the same characteristics in the intercalated carbon fibers proved to be slightly more difficult

than expected. The photolithography mask did not include a section to test electrical conductivity so another method was devised. Although the surface of HOPG is very stiff in the a-plane, it is easy to fracture when pressure is asserted in the direction normal to that plane. Knowing this, HOPG was placed across a die to achieve the longest run possible of HOPG and then used a Micromanipulator probe station to score and eventually tear wear grooves into the HOPG on the surface of the die, forming strips of HOPG, as presented in Figure 6-10.
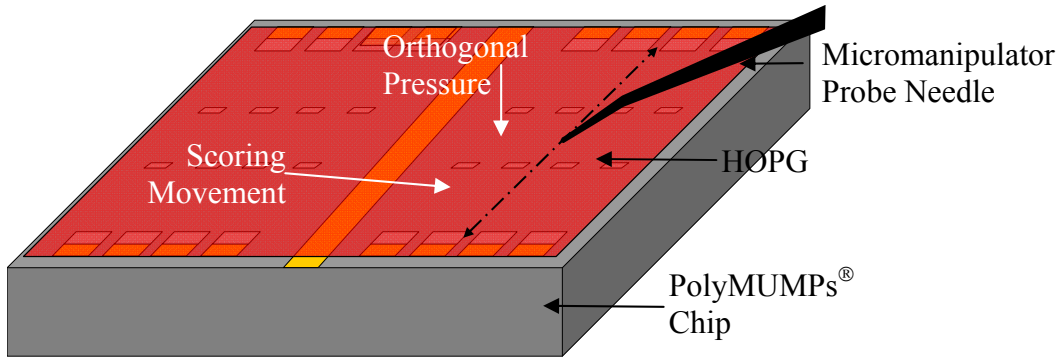
Figure 6-10: Example showing the mechanical formation of HOPG strips used to test intercalated HOPG electrical characteristics.

The structure that resulted from scoring and tearing the HOPG as described yielded two strips of HOPG, approximately 3 mm in length and 450 μm wide with a nominal thickness of 0.25 μm. A way was then required to attach the HOPG to the bond pads. Since the area to bond was large, the FIB platinum deposition would have taken several hours per location. Thus the second best method, metal evaporation, was used to attach the HOPG to the polysilicon bond pads. In this case, since it was unnecessary to release the structures using hydrofluoric acid, it was possible to place 250 Å of titanium and 2000 Å of gold onto the structures. Since the height of the HOPG was 0.25 μm and the height of the metals 0.225 μm, the adhesion between the pad and the HOPG were

very good. There was no mask for this step, but since the size of the strips was so large in comparison to carbon fiber work, mask was fabricated using aluminum foil, and metals were deposited as presented in Figure 6-11. The chip was adhered to a glass slide using Kapton™ tape, and then small sections of aluminum foil were placed in a criss-crossing pattern to leave windows where gold was desired. The final dimensions of the contacted ends of the HOPG strips were 1750 μm long × 500 μm wide and 0.25 μm thick, with a gold covered area of 500 μm × 50 μm on each end of the HOPG strips
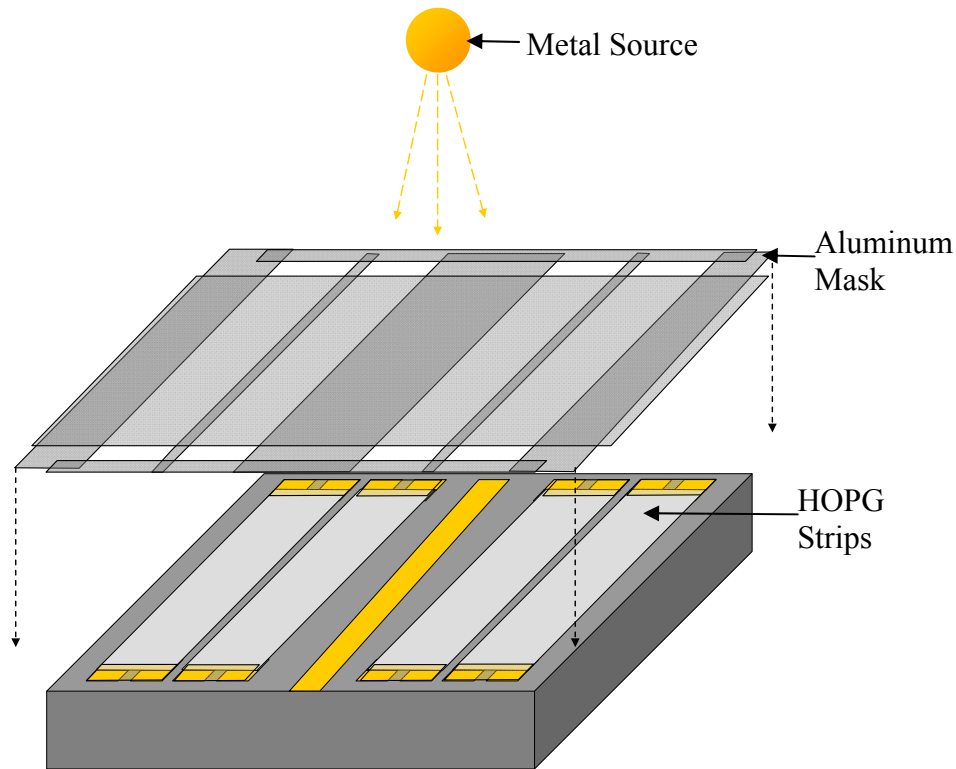
Figure 6-11: Aluminum foil mask used to pattern micromanipulator trenched HOPG strips for electron beam metal deposition.

6.2 Testing HOPG Structures

In order to compare the thin-film HOPG performance with results from carbon fiber tests, testing was performed identically to that accomplished for carbon fibers. This testing measured the mechanical response of the PECT effect in HOPG thin films. The photolithography process produced a single HOPG actuator, while two HOPG strips were created for electrical testing.

6.2.1   HOPG Mechanical Testing

Using the same test setup as was used for carbon fibers, the HOPG sample chip was wire bonded and encapsulated inside a 40-pin dual-inline package chip carrier and tested using the same test setup as presented in Section 4.1.7 . Figure 6-12 (a) presents the at rest position of the HOPG actuator system prior to applying intercalation voltage and (b) the same actuator under 1.6 V of electrolysis voltage. Note that the area in the center separates in a semicircular pattern around the fiber. This area is a thin layer of photoresist that was not removed, or redeposited during the acetone rinse of the completed die. The bottom of the pad also had some residual photoresist, and a gap can be seen appearing during actuation.

Since the photoresist formed a barrier between the HOPG strip and the polysilicon pad beneath, the platinum FIB patches adhered to that photoresist instead of the polysilicon underneath. As such, this device produced a reaction force due to the contacted photoresist, but the force was lower than that of the polysilicon beams connecting the polysilicon pad to the substrate. In this case, the force is low enough that it is represented as an unloaded actuator and compare the results of this actuator with the series developed for carbon fibers.

139
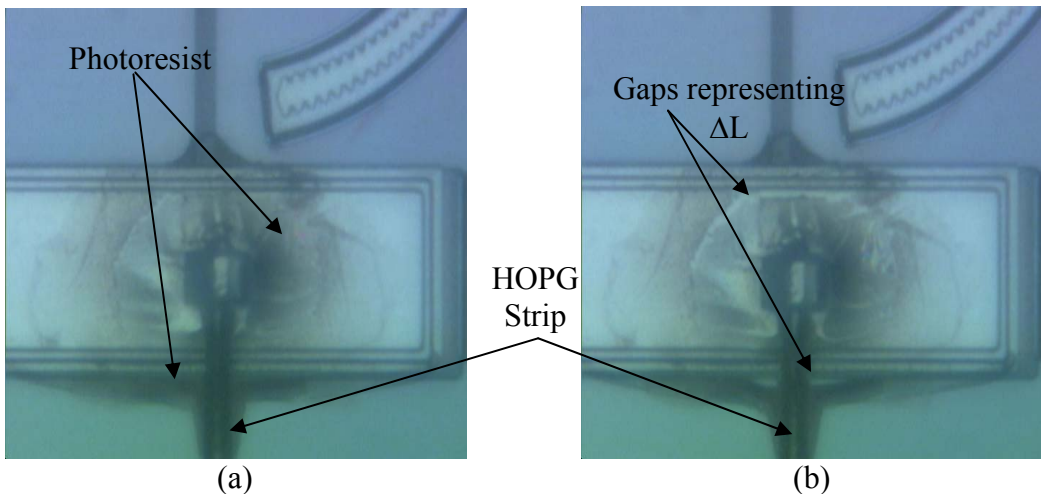
Figure 6-12: Still photos at 100x magnification presenting (a) HOPG actuator at rest and (b) the same actuator at 1.6 V bias. Images were taken through a glass cover and H_2SO_4.

Results from this test are more linear at actuation voltages with the exception of 1.1 to 1.2 V where the thin film of photoresist finally reaches fracture and releases some of the reaction force applied to the fiber. At this point, the device shifts to a different stress/strain curve and continues actuation until 1.6 V of electrolysis voltage is reached. The end point of the second curve, which is more indicative of zero reaction force than the first portion of the curve, fits into the minimum and maximum range of operation for the 7 run average for a 500 μm P-100 fiber in the same intercalant. It was possible to reliably drive the HOPG device at 1 and 10 Hz, and observe actuation at those frequencies, however the maximum frequency could not be predicted since continuous current data was not collected for this test. Figure 6-13 presents the strain produced by the demonstration of a 1000 μm long HOPG actuator, with a comparison to the minimum and maximum results for the 7 run carbon fiber baseline test. In this case, overpotential begins to occur at 1.2 V of applied potential, and assumes a total of one oxygen atom bonded per 1062 carbon atoms at 1.6 V of applied potential or $C_{1062}O$.
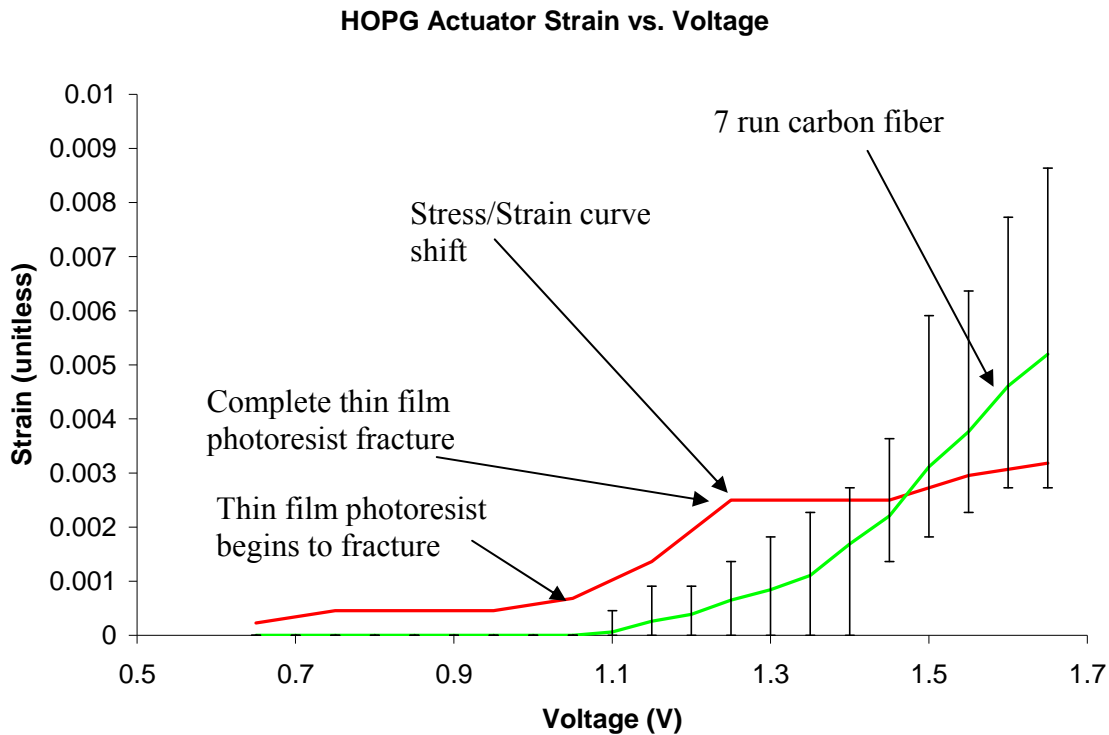
Figure 6-13: HOPG actuator strain plotted against electrolysis voltage and compared to 7 run minimum and maximum data for baseline carbon fiber.

6.2.1.1   Carbon Fiber Mechanical Comparisons

Since the mechanical testing of the HOPG patterned actuator was a demonstration, and contained only one run of test data, it becomes necessary to draw comparisons to the testing performed on the carbon fibers. The large demand on equipment and personnel at AFRL prevented the fabrication of more than the first test device in HOPG. As such, these comparisons merge data from Sections 4.1.7 and 6.2.1 to describe the overall effectiveness of possible thin-film PECT actuators. The first factor to consider is the nature of the PECT HOPG strip's connection to the substrate. It is obvious that the response produced by the HOPG is tethered, e.g. there is some reaction force being applied to the HOPG strip by the mechanical structure underneath,

and by the photoresist that continues to hold the strip to the polysilicon structure underneath.

The second consideration is the cross-sectional area of the HOPG strip in comparison to the P-100 carbon fiber. In the nominal case for the carbon fiber, the cross-sectional area is 78.5 μm^2. For the particular 0.25 μm thick piece of HOPG, the area is only 2.5 μm^2 for the same actuator width of 10 μm. Even with a minimal reaction force, the internal stress produced by the HOPG strip becomes significant.

Since it was not possible to achieve an accurate measurement of the physical properties constraining the HOPG actuator, the strain data of this actuator was compared with the 7-run series for the baseline unloaded carbon fiber, as presented in Figure 6-13. During intercalation, the fiber began to buckle a thin film of photoresist as noted in Figure 6-12. When the photoresist finally fractured, an increase in strain was observed that caused a discontinuity when compared to the rest of the response. This indicates that the unloaded response is somewhat higher than the section of data collected prior to this fracture and has a smoother transition than the chart suggests.

The total strain in the HOPG is clearly in the range observed for the baseline carbon fiber from 1.4 to 1.6V DC. Prior to this point, a more stable change in strain than observed in baseline fiber testing occurs. The difference in these two actuator designs lies primarily in the fabrication methods themselves. As discussed in Chapter 4, the carbon fibers were not perfectly straight, and many had curves that caused some of the actuation potential to be used to straighten the fiber prior to actually seeing axial contraction at the end of the fiber. Within the HOPG strip, there little non-planarity,

which promotes quicker response in the actuator itself. The results from this initial HOPG demonstration show promise for future work.

6.2.2   HOPG Electrical Testing

Using the same test setup as was used for carbon fibers, the HOPG sample chip was wire bonded and encapsulated inside a 40-pin dual-inline package chip carrier and tested using the same test setup as presented in Section 4.1.7 . This structure was used to carry out electrical experiments on two separate 500 μm by 1750 μm sections of HOPG. The first tests conducted were baseline tests to determine the dry resistivity of the HOPG strips. Two runs were performed during this baseline test to ensure the results were repeatable. Figure 6-14 presents the phase data for both runs. Unlike the carbon fiber data, the HOPG changes phase at 7 points, indicating again that there may be a minima or maxima in the capacitance or inductance values at those points, which should cause a peak or valley in the impedance values, which does not occur. Figure 6-15 presents the resistance data corresponding to the phase information presented in Figure 6-14.

Following dry-run resistivity testing, the chip carrier was filled with sulfuric acid and sealed the carrier using the standard sealing methods in this research. A baseline resistivity test in the ambient solution was then accomplished to determine any phase or resistivity changes caused by immersion in the intercalant. Figure 6-16 presents the phase data for this test while Figure 6-17 presents the resistivity data under the same conditions at 0 V intercalation voltage in aqueous sulfuric acid.
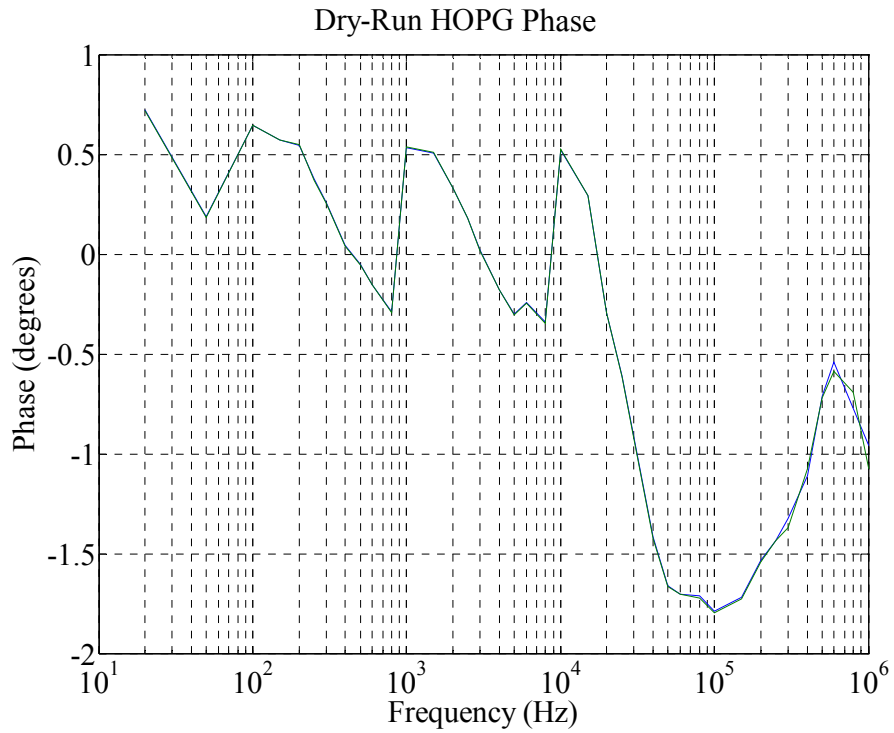
Figure 6-14: HOPG dry-run phase results for 500 μm × 1750 μm strip of HOPG over two successive frequency sweeps.
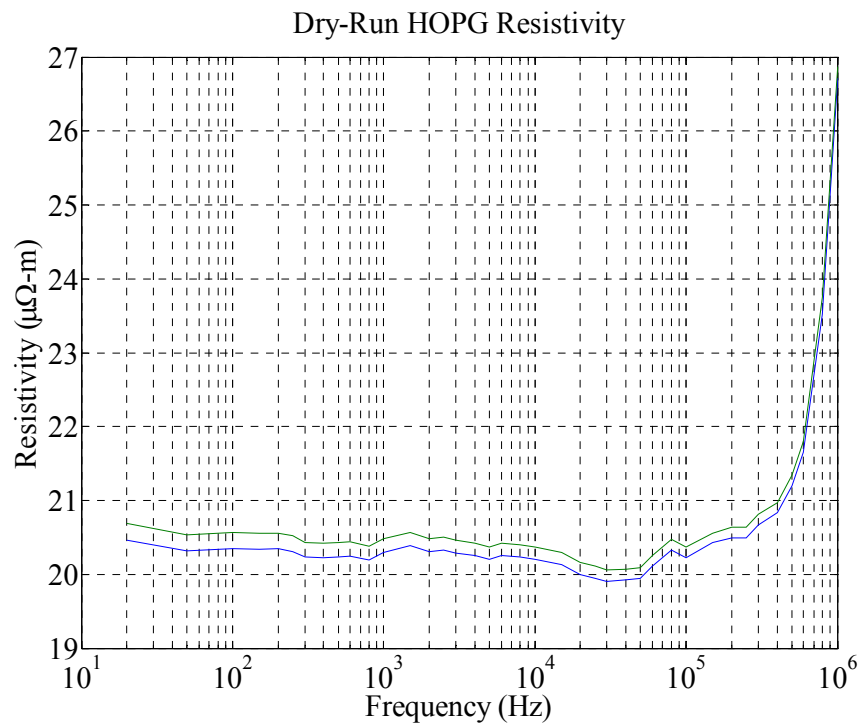
Figure 6-15: HOPG dry-run resistivity results for 500 μm × 1750 μm strip of HOPG over two successive frequency sweeps.
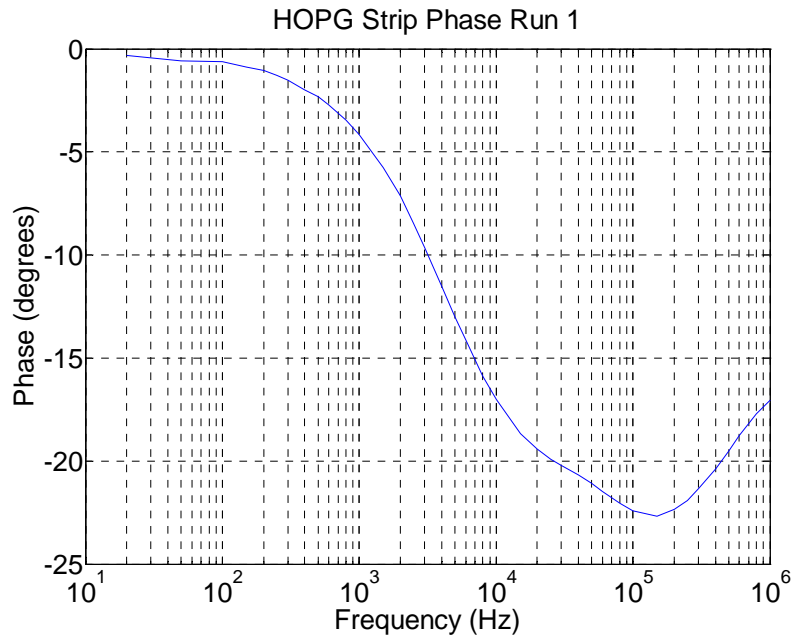
Figure 6-16: HOPG wet-run phase results for 500 μm × 1750 μm strip of HOPG over two successive frequency sweeps with no intercalation voltage.
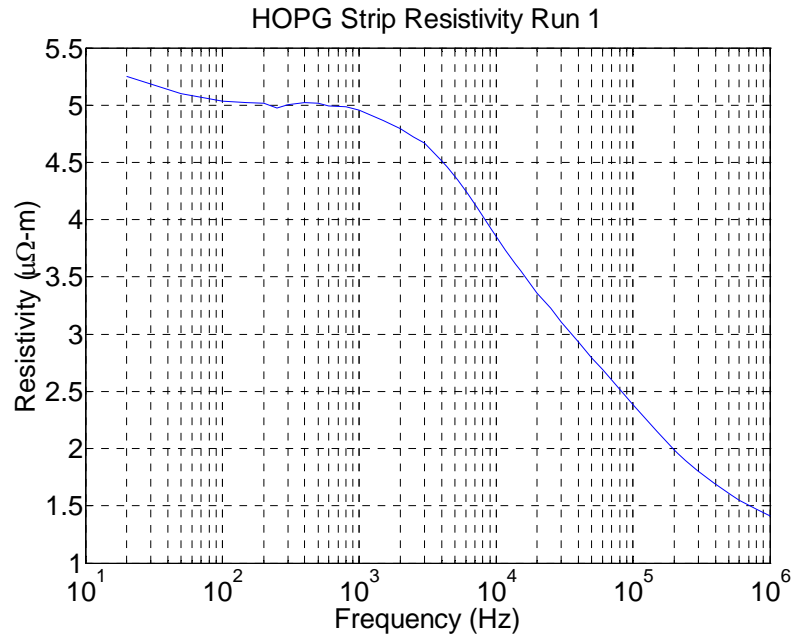
Figure 6-17: HOPG wet-run resistivity results for 500 μm × 1750 μm strip of HOPG over two successive frequency sweeps with no intercalation voltage.

Once wet run baseline testing was completed, the VEE Onelab program was started to cycle through intercalation voltages and sweep frequencies at each voltage. Results for both HOPG samples were collected at frequencies from 20 Hz to 10 MHz and intercalation voltages from 0.0 to 1.6 V of intercalation voltage. Figure 6-18 and Figure 6-19 present the phase results for the HOPG samples.
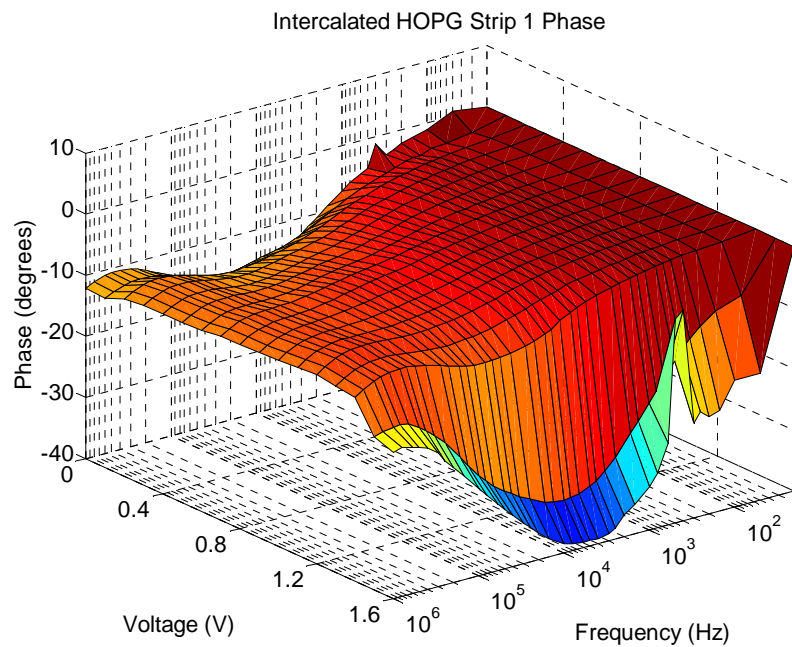
Figure 6-18: HOPG wet-run phase results for first 500 μm × 1750 μm strip of HOPG over two successive frequency sweeps intercalating from 0.0 to 1.6 V of intercalation voltage.

The two phase diagrams show nearly identical phase structures of the HOPG strips under test. The majority of the phase stays negative with a single frequency/voltage grid in each crossing the zero point where a minima or maxima in impedance could occur. However, the behavior of the HOPG strip, much like that of the carbon fiber, does not exhibit a minima or maxima in impedance at this point. Thus, again as Winningham cites, the phase may be so small that capacitance and resistance

play a negligible role in impedance and second, and possibly more likely, that the circuit is composed of an amalgam of parallel and series circuits that cause the final circuit to behave in an unidentifiable manner. When comparing the characteristics of the phase in Figure 6-18 and Figure 6-19 with the previous results for a carbon fiber under the same conditions as presented in Figure 5-5, the phase is consistent in shape. This indicates that the carbon fiber and HOPG have similar characteristics upon intercalation, and exhibit the same impedance characteristics at any given frequency. The difference in the magnitude of the phase value between the HOPG samples and the carbon fiber are likely due to the lower amount of order in the graphite planes within the carbon fiber as compared to the HOPG strip.
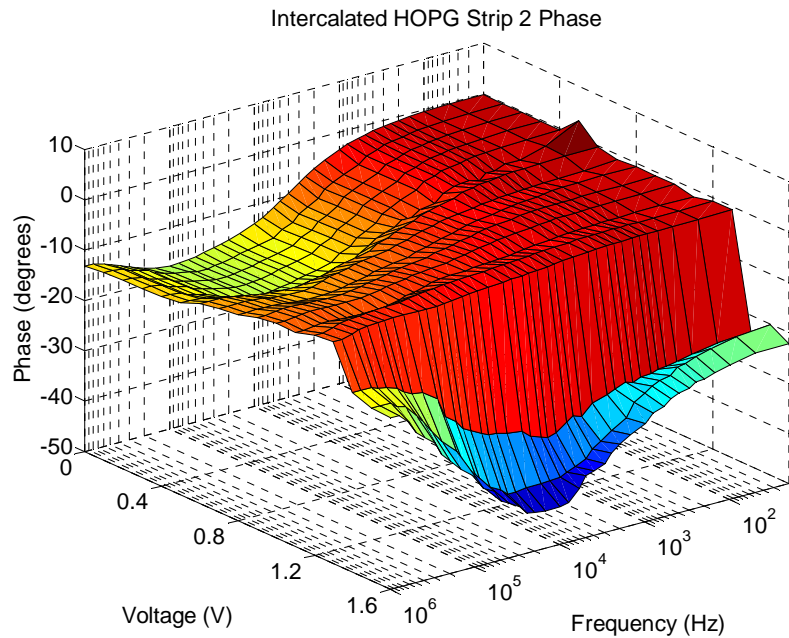
Figure 6-19: HOPG wet-run phase results for second 500 μm × 1750 μm strip of HOPG over two successive frequency sweeps intercalating from 0.0 to 1.6 V of intercalation voltage.

147

Figure 6-20 and Figure 6-21 present the resistivity of the HOPG strips over the tested frequency and intercalation voltage ranges. In both cases, note that there is a slight decrease in resistivity over all frequencies from 1.1 to 1.4 V DC intercalation voltage, and that after this point, the resistivity dramatically decreases, and is more pronounced at lower frequencies.
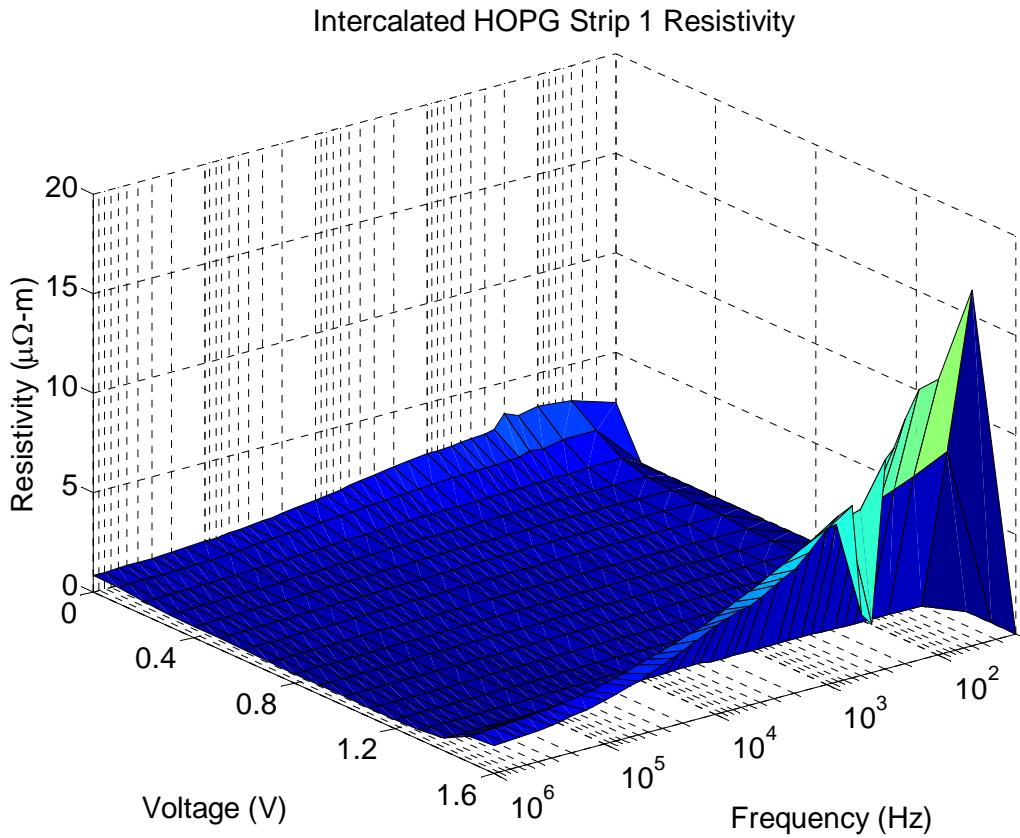
Figure 6-20: HOPG wet-run resistivity results for first 500 μm × 1750 μm strip of HOPG over two successive frequency sweeps intercalating from 0.0 to 1.6 V of intercalation voltage.

Compare these data points to the same test performed on a carbon fiber as presented in Figure 5-6. It is necessary to note the difference in maximum voltage in the two figures, the HOPG is taken from 0.0 to 1.6 V of intercalation voltage while the fiber

was only taken to 1.4 V DC. The results indicate that the resistivity of the carbon fiber

and HOPG strips follow the same trends given intercalation and voltage. It also indicates

that the carbon fiber resistivity breaks down slightly more at higher voltages than the

HOPG strips.
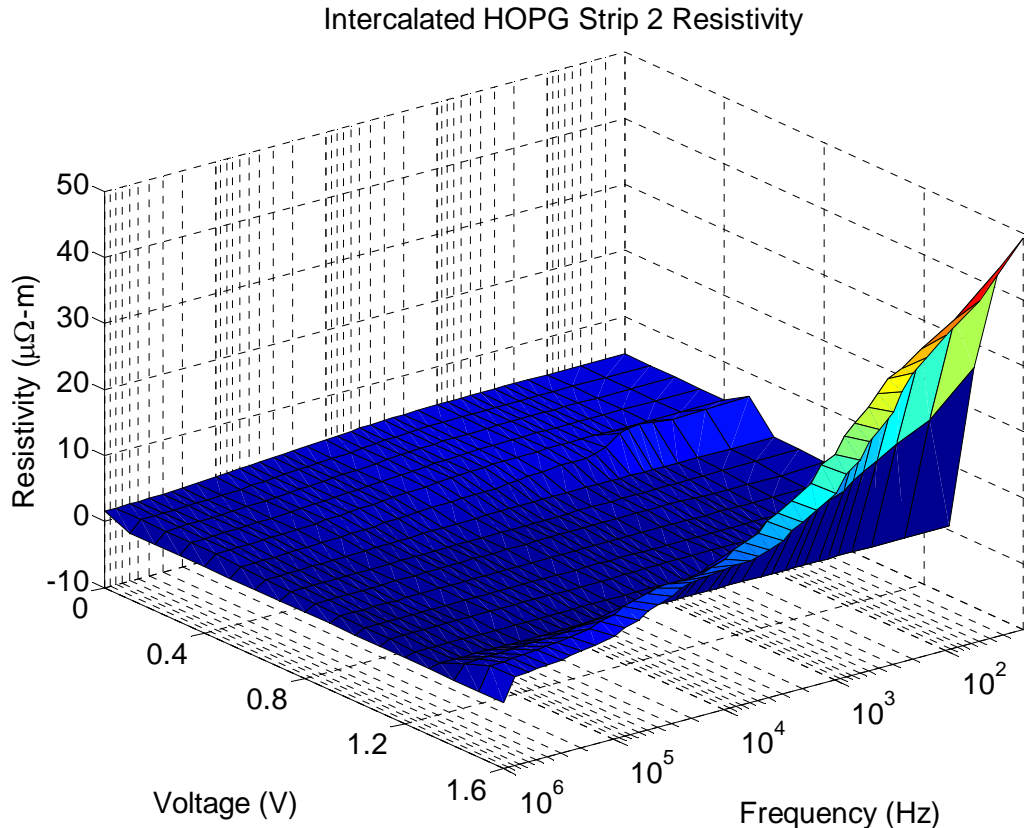
Figure 6-21: HOPG wet-run resistivity results for second 500 μm × 1750 μm strip of HOPG over two successive frequency sweeps intercalating from 0.0 to 1.6 V of intercalation voltage.

The resistivity of the HOPG strips decreases with increased intercalation voltage

as it did in the carbon fiber, decreasing until the intercalation voltage reaches 1.3 V DC,

and then increasing gradually until 1.5 V DC where it begins climbing drastically at

lower frequencies, but stays relatively stable at higher frequencies again indicating an

increase in the inductive nature of the impedance in the HOPG strip, similar to that of the carbon fiber.

6.3 Conclusions

In this Chapter, the formation of thin-films of HOPG onto the surface of traditional MEMS structures were discussed, using commercial block HOPG and formed through successive applications of tape liftoff. Methods for placing the resultant thin film of HOPG onto the surface of the PolyMUMPs® die were presented. Successfully patterned thin-film HOPG structures suitable for use in MEMS were also demonstrated. It is also evident that, electrically, the HOPG strips behave similarly to carbon fibers under the same conditions, and that HOPG strips actuate within a range of motion and change resistivity in a very similar manner as intercalated carbon fibers.

Chapter 7 will present the overall conclusions derived from this research into the PECT effect in graphitic carbon. It will also make a recommendation for the use of the PECT effect as an actuation material, and finally make recommendations for future work in the area of PECT intercalated graphite as an actuation material.

PIEZO-ELECTROCHEMICAL TRANSDUCER EFFECT (PECT)

INTERCALATED GRAPHITE MICRO-ELECTROMECHANICAL

ACTUATORS

7. Conclusions, Recommendations and Future Research

Research in the PECT effect began in September 1981 when Dr. F. Lincoln Vogel first discovered that intercalation voltages could be used to provide an in-plane actuation force in graphitized carbon fibers. This research expanded on this original research and defined the first hybrid MEMS devices using first, lengths of fully immersed carbon fibers and second, patterned HOPG as the actuation material for these actuators in an aqueous sulfuric acid environment. Although other research has been accomplished in carbon nanotube actuators [47,58] and orthogonal actuation of HOPG [33,34,51], this research is the first to utilize the strong in-plane forces that affect the crystalline structure of the graphene planes within graphitized carbon structures.

7.1 Conclusions of Current Research

Analysis of the data obtained for experimental structures in this research concluded that the electrical characteristics of Cytec Thornell® P-100 carbon fibers decrease in resistivity until overoxidation when they begin to drastically increase their resistivity. Inductance, capacitance and impedance measurements were conducted on these fibers to determine how they responded at different frequencies. The response was complex and a model was impractical. The same analysis was performed on thin strips of HOPG and these strips behave similarly to P-100 carbon fibers under the same

conditions, thus it can be reasonably concluded that thin film graphite acts the same as carbon fibers, studied extensively in the literature.

In addition to electrical verification, this research breaks new ground in the area of strong, lightweight, small area, high force actuators. The in-plane reactions that induce axial strain in both P-100 carbon fibers and thin film actuators patterned from a thin layer of highly oriented pyrolytic graphites. These actuators produced results that produce nearly two orders of magnitude higher strain than traditional polysilicon thermal actuators used in MEMS applications today. In addition to high strain, the PECT effect in graphite (either fibers or thin-film) produces significant internal stress which equates to pulling power. Methods were developed to accurately measure strain and integrate these materials into mainstream MEMS structures, but were limited to the aqueous electrolytes of sulfuric acid and 1 M NaCl. This research also showed that the PECT effect could be actuated at 80 Hz, and can be held in an actuated position once actuated with virtually no power at under 1.6 V of DC actuation potential. Unfortunately, this research solely used aqueous compounds as an intercalant and this will always limit the usefulness of the PECT effect in mainstream microelectronics and MEMS actuation. Fortunately, there have been other actuators using conducting polymers fabricated with electrolyte-impregnated polymers as the electrolytic reservoir for the system [59] and another less ionic intercalant.

7.2 Recommendations for Future Research

In order to integrate the very novel and promising PECT effect as an actuation material in mainstream MEMS devices, a few hurdles must first be overcome. The first of these is the experimental nature of the actuators. Integrating carbon fibers onto

specific locations as actuation devices is impractical at anything more than an experimental scale. Thin film HOPG using the method in this research also falls into that category. A thin-film of HOPG was successfully patterned and intergrated with a commercially micromachined die and tested the resultant structure, demonstrating actuation visually at up to 10 Hz. This actuator behaves similarly to P-100 fiber actuators, that more robust testing was performed upon. However, the application of HOPG is time consuming and inappropriate for any commercial process. HOPG itself is grown at high temperatures (1800 to 3000° C) using chemical vapor deposition. Given the right substrate, it is entirely possible to produce this polycrystalline graphite as a thin-film layer integrated as the actuator in a new MEMS process. Thus, the first recommendation for future research is to investigate the possibility of integrating thin-film CVD graphite with a commercial stubstrate, such as silicon carbide to create and pattern next-generation MEMS devices

The second hurdle is the nature of the electrolytes utilized as intercalants. A larger set of aqueous intercalants must be researched and characterized prior to commercialization. This is the best option given that most active intercalants such as sulfuric acid are incompatible with most MEMS applications, even those applications that require a high-force high-strain application. It follows that the second suggestion for future research is to integrate electrolyte-impregnated polymer with true thin-film HOPG.

If these two challenges are successfully met, this technology will push the envelope of MEMS device applications, enable lighter, more efficient actuators and mechanisms such as robotic arms that were previously unable to be created due to lack of

power. PECT graphite can become the hydraulics of the micro-world pushing this very promising actuation material to the forefront of MEMS actuation technologies.

7.3 Additional Recommendations

Some suggestions for thin-film, and even composite actuators that may be able to use this material will be made. First, the MEMS scale actuation, as it is the most applicable to this research area will be discussed. Linear actuation is only one of many applications that in-plane strain can be utilized for. One of the easiest applications of this in-plane strain is in the form of a micro-iris. If a thin-film of graphite is created in a torus, and the outer edges are constrained, intercalation will cause the inner, exposed part of the torus to expand and contract. This will change the diameter of the iris hole and thus change the aperature that this hole creates. If a deformable lens material is integrated into this structure, a way of changing focal length of a light-emitting diode or semiconductor laser on die is then created.

The second additional suggestion is back in the macro realm. Carbon fibers are regularly used as reinforcement to polymer compounds to make lightweight, strong structures. They are woven into fabrics and formed with this polymer to create many structures from bicycle frames to aircraft surfaces. If an electrolyte impregnated polymer is used instead of an aqueous electrolyte, reinforced with carbon fibers and the carbon fiber was biased in different sections of an aircraft wing against a counter electrode also contacting the polymer, the wing shape to could change, thus creating a rigid, deformable airfoil that can act as a complete control surface with no mechanical parts involved.

7.4 Summary

In this section, conclusions were drawn that can be achieved with additional effort in this research area, and recommendations were given for the next logical steps for future research in this area. Specific additional recommendations were given which may be useful to researchers that follow this work, and this summary finally concludes this dissertation.

VITA

Major Glen A. Kading was born in Omaha, NE. He attended school in the small rural town of Bennington, where he enjoyed Kindergarten through 12th grade in the same building complex. He discovered the U. S. Air Force Academy during his junior year and decided to attempt to receive an appointment, after enjoying their Summer Scientific Seminar program that summer. He was appointed in 1989 and began his Air Force career. Four years later, he graduated, married his sweetheart in June of 1993, and was commissioned an officer in the U. S. Air Force. He became the expert in acquisition programs during his time as an acquisition program manager for EF-111A and B-1 programs, and applied to the Master's degree program at the Air Force Institute of Technology. He successfully completed the degree program with the thesis "Micro-electromechanical Switches for Micro-Satellite Power Transfer", and was awarded his degree Master of Science in December 1997. He was then sent to San Antonio to work on distributed mission training and followed on to Edwards AFB, CA to spend four years in electronic warfare flight test. He was lucky enough to be accepted back to the Air Force Institute of Technology where he researched this Dissertation. Glen is the proud parent of four wonderful children, and he and his wife are enjoying every minute of life with their family.

References

[1] Burns, D. M., "Microelectromechanical optical beam steering systems," Thesis (Ph. D.)--Air Force Institute of Technology, 1998.

[2] Vogel, F. L., "Quest for Technology: Electrical Actuator," Memorandum, 8 September 1981.

[3] Leshin, V. S., Sorokina, N. E. and Avdeev, V. V., "Electrochemical Synthesis and Thermal Properties of Graphite Bisulfate", *Inorganic Materials*, vol. 40, no. 6, pp. 744-750, 2004.

[4] Heiserman, D. L., *Exploring Chemical Elements and their Compounds,* Blue Ridge Summit, PA: Tab Books, 1992.

[5] Austerman, S. B., *Chemistry and Physics of Carbon*, vol. 4, New York: Marcel Decker, 1969.

[6] Pauling, L., *The Nature of the Chemical Bond.* Ithaca, New York: Cornell University Press, 1948.

[7] Ramakrishna, B. L. "Carbon Bonding", in *Interactive Nano-Visualization in Science & Engineering Education: The allotropes of Carbon*, http://invsee.asu.edu/nmodules/Carbonmod/bonding.html, viewed 2 October 2007.

[8] Yudasaka, M., Kikuchi, R., Matsui, T., Kamo, H., Ohki, Y., Yoshimura, S. and Ota, E., "Graphite thin film formation by chemical vapor deposition of o-methyl-diaryl ketones," *Appl. Phys. Lett.,* vol. 64, pp. 842, 1994.

[9] Bacon, R. and Singer, L. S. (Feb 2003). *Isotropics: American Chemical Society Cleveland Section* pp. 3.

[10] Tzeng, S. S. and Nien, M. H., Distribution of intercalant in copper chloride and iron chloride graphite intercalation compounds. *J Mater Res* **14** 1 (1999), pp. 302–307.

[11] Vogel, F. L., "The Electrical Conductivity of Graphite Intercalated with Superacid Fluorides: Experiments with Antimony Pentaflouride", *Journal of Materials Science,* vol. 12, no. 5, pp. 982-986, 1777.

[12] Fischer, J. E., Metrot, A., Flanders, P. J, Salaneck, W. R. and Brucker, C. F., "Lattice sability and limits to charge transfer in intercalated graphite", *Physical Review B,* vol. 23, no. 10, pp 5576-5580, 1981.

[13] Ebert, L. B. and Appelman, E. H., "Comment on graphite intercalated with H_2SO_4", *Physical Review B,* vol. 28, no. 3, pp. 1637-1638, 1983.

[14] Leshin, V. S., Sorokina, N. E. and Avdeev, V. V., "Graphite Intercalation in H_2SO_4-CH_3COOH Electrolytes", *Inorganic Materials,* vol. 39, no. 8, pp. 826-832, 2003.

[15] Shioyama, H. and Fujii, R, "Electrochemical Reacitons of Stage 1 Sulfuric Acid – Graphite Intercalation Compound", *Carbon*, vol. 25, no. 6, pp. 771-774, 1987.

[16] Aronson, S., Lemont, S. and Weiner, J., "Determination fo the H2SO4:HSO4- and HClO4:ClO4- Ratios in Graphite Lamellar Compounds", *Inorganic Chemistry,* vol. 10, no. 6, pp. 1296-1298, 1971.

[17] Aronson, S., Frishberg, C. and Frankl, G., "Thermodynamic Properties of the Graphite-Bisulfate Lamellar Compounds", *Carbon*, vol. 9, pp. 715-523, 1971.

[18] Metrot, A. and Fuzellier, H., "The Graphite-Sulfate Lamellar Compounds-I: Thermodynamic Properties, New Data", *Carbon*, vol. 22, no. 2, pp. 131-133, 1984.

[19] Zhang, J. M., Hoffman, D. M. and Ecklund, P. C., "Optical study of the K-point π-band dispersion in graphite-H_2SO_4", *Physical Review B,* vol. 34, no. 6, 1986.

[20] Metrot, A. and Fischer, J. E., "Charge Transfer Reactions During Anodic Oxidation of Graphite in H_2SO_4," *Synth Met,* vol. 3, pp. 201-207, 1980.

[21] Zabel, H., Solin, S. A. and Hwang, D. M., *Graphite Intercalation Compounds I : Structure and Dynamics.* Berlin; New York: Springer-Verlag, 1990, pp. 356.

[22] Massey, C., McKnight, G., Liu, P., & Barvosa-Carter, W., "Graphite intercalation compounds as actuation materials," *in Proceedings of the ASME Aerospace division – 2004: Adaptive Materials and Systems, Aerospace Materials and Systems*, 13-20 November 2004, pp. 117-122.

[23] Massey, C., McKnight, G., Barvosa-Carter, W., & Liu, P, "Reversible work by electrochemical intercalation of graphitic materials", in *Smart Structures and Materials 2005: Smart Sensor Technology and Measurement Systems. Edited by Udd, Eric; Inaudi, Daniele. Proceedings of the SPIE, Volume 5759, Pp. 322-330 (2005).* 2005, pp. 322-330.

[24] Dresselhaus, M. S., Dresselhaus, G. and Eklund, P. C., *Science of Fullerenes and Carbon Nanotubes.* San Diego: Academic Press, 1996.

[25] Neamen, D. A., *Semiconductor Physics and Devices: Basic Principles.* ,3rd ed.Boston: McGraw-Hill, 2003, pp. 746.

[26] Nixon, D. E. and Parry, G. S., "The expansion of the carbon-carbon bond length in potassium graphites," *J. Phys. C: Solid State Phys.,* vol. 2, pp. 1732-1741, 1969.

[27] Pacault, A., *Les Carbones. ,* vol. Tome II, Paris: 1965.

[28] Maeda,Y., Okemoto, Y. and Inagaki, M., "Electrochemical Formation of Graphite-Sulfuric Acid Intercalation Compounds on Carbon Fibers," *J. Electrochem. Soc.,* vol. 132, pp. 2369-2372, 1985.

[29] Pietronero, L., Strässler, S., "Bond-Length Change as a Tool to Determine charge Transfer and Electron-Phonon Coupling in Graphite Intercalation Compounds", *Physical Review Letters* vol. 47, no. 8, pp. 593-596, 1981.

[30] Chan, C. T., Kamitakahara, W. A., Ho, K. M., Eklund, P. C., "Charge-Transfer Effects in Graphite Intercalates: *Ab Inito* Calculations and Neutron-Diffraction Experiment", *Physical Review Letters*, vol. 35, no. 15 (13 Apr 1987) 1528-1531 .

[31] Flandrois, S., Hauw, C., Mathur, H. B., "Charge Transfer in Acceptor Graphite Intercalation Compounds", *Synthetic Metals* 34 (1989) 399-404.

[32] Metrot, A., Fischer, J. E., "Charge Transfer Reactions During Anodic Oxidation of Graphite in H_2SO_4", *Synthetic Metals* **3** (1981) 201-207.

[33] Chung, D. D. L., Wong, L. W., "Electrochemical Behavior of Graphite Intercalated with Bromine," *Carbon*, vol. 24, pp. 639-647, 1986.

[34] Chung, D. D. L., "Intercalated graphite as a smart material for high-stress, high-strain, low-electric-field electromechanical switching," *Smart Mater Struct*, vol. 1, pp. 233, 1992.

[35] Rogers, B., Adams, J. and Pennathur, S., *Nanotechnology: understanding small systems,* Boca Raton, Taylor & Francis, 1997.

[36] Feynman, R. P., "There's Plenty of Room at the Bottom", *Journal of Micro-electromechanical Systems* **1** (1992) 60-66

[37] Peterson, K. E., "Silicon as a Mechanical Material", *Proceedings of the IEEE* vol. 70 no. 5 (May 1982).

[38] Feynman, R. P., "Infinitesimal Machinery", *Journal of Microelectromechanical Systems* 2 (1993) 4-14.

[39] Szabo, F. R., "Demonstrating optothermal actuators for an autonomous MEMS microrobot," Thesis (M.S.)--Air Force Institute of Technology, 2004.

[40] Denninghoff, D. D., "Power-Scavenging MEMS Robots," Thesis (M.S.)--Air Force Institute of Technology, 2006

[41] Burns, D. M., "Microelectromechanical optical beam steering systems," Thesis (Ph. D.)--Air Force Institute of Technology, 1998.

[42] Yan, D., Khajepour, A., Mansour, R., "Design and modeling of a MEMS bidirectional vertical thermal actuator," *J Micromech Microengineering,* vol. 14, pp. 841-850, 2004.

[43] Koester, D., Cowen, A., Mahadevan, R. and Hardy, B., *PolyMUMPs Design Handbook: A MUMPs® process* (Revision 10.0), MEMSCAP®. www.memscap.com/memsrus/ docs/PolyMUMPs.dr.v10.pdf, 2003.

[44] *Electronic and Photonic Applications of Polymers,* ed. Bowden, M. J., Turner, R. S., American Chemical Society, Washington DC, 1988.

[45] Saunders, H. E. and Schoch Jr., K. F., "Conducting Polymers", *Proceedings of the 20th EEIC/ICWA Exposition, Electrical Electronics Insulation Conference,* IEEE Press, Boston, 1991.

[46] *Electroactive Polymer (EAP) Actuators as Artifical Muscles,* ed. Bowden, M. J. and Turner, R. S., American Chemical Society, Washington DC, 1988.

[47] Baughman, R. H., Changxing, C., Zakhidov, A. A., Iqbal, Z., Barisci, J. N., Spinks, G. M., et al., "Carbon Nanotube Actuators", *Science* 1999; 284:1340.

[48] Gartstein, Y. N., Zakhidov, A. A., Baughman, R. H., "Charge-induced anisotropic distortions of semiconducting and metallic carbon nanotubes", *Physical Review Letters* vol. 89, no. 4 (22 July 2002).

[49] Frayse, J., Minett, A. I., Jaschinski, O., Duesberg, G.S., Roth, S. "Carbon nanotubes acting like actuators", *Carbon* vol. 40, pp. 1735-1739, 2002.

[50] Chung, D. D. L., "Exfoliation of graphite," *J. Mater. Sci.,* vol. 22, pp. 4190-4198, 1987.

[51] Salib, M. S., Petrou, A., Chung, D. D. L., "Optomechanical actuation using intercalated graphite," *Carbon,* vol. 35, pp. 709-711, 1997.

[52] Sharpe, W. N., Jr., "Tensile Testing at the Micrometer Scale (Opportunities in Experimental Mechanics)". *Experimental Mechanics*. 43 (2003):228-237.

[53] Winningham, B. W. "Characterization of Intercalated Graphite Fibers for Microelectromechanical Systems (MEMS)", Thesis, Air Force Institute of Technology School of Engineering and Management, 2007.

[54] Agilent Technologies, Agilent 4284A Precision LCR Meter: Operation Manual, Including Option 001, 002, 006, 201, 202, 301, eighth edition, January 2001.

[55] Cytec Engineered Materials, "Typical properties of Thornel P-100s continuous pitch-based fiber", http://www.cytec.com/business/EngineeredMaterials/CFInternet/ cfThornelP-100Spitch.shtm, February 2007.

[56] Gupta, K. C., Grag, R., and Chada, R., *Computer Aided Design of Microwave Circuits*. Dedham, MA: Artech House, 1981, pp. 25-43.

[57] Vo, V. T., Krishnamurthy, Q. S. Rezazedeh, A. A. and Sloan, R. "3-D Low-loss Coplanar Waveguide Transmission Line Structures with Wide Range of Characteristic Impedance for MMICs", *Microwave Conference, 2005 European* , vol.2, no., pp. 4 pp.-, 4-6 Oct. 2005

[58] Fraysse J, Minett AI, Jaschinski O, Duesberg G S and Roth S 2002 Carbon nanotubes acting like actuators. *Carbon* **8 40** 1735-1739

[59] Koyama Y, Chin T E, Rhyner U, Holman R K, Hall S R and Chiang Y-M 2006 Harnessing the actuation potential of solid-state intercalation compounds. *Advanced Functional Materials* **16** 492-498

APPENDIX A: FIBER ATTACHMENT METHODS

A.1   Fiber Attachment

During the course of this dissertation research, we researched many methods of attaching carbon fibers to a polysilicon structure to create a hybrid MEMS actuator system. Our goal is to provide an electrical contact between the fiber and the underlying structure that is also mechanical sound. The first part of this procedure was very easy, while the second proved to be more problematic. We investigated a range of solutions, including several different silver epoxies, solder powder, metallization, and finally focused ion beam platinum deposition. The latter two produced acceptable results and were published in the body of the dissertation. The former were unusable, as they either dissolved into a brown liquid upon the addition of intercalant, or were unusable immediately after application. Since some dissolved into the intercalant, we also tried to cover those substances in paraffin to protect them from the acid we used in our research. This appendix presents the faild methods and offers a brief description of why they failed to work for our research.

A.2   Conductive Epoxy

Our first experiment used colloidal silver covered with a Teflon™ fingernail polish to attach the fibers between the load cell and electrode, and suspend it across the acid bath. In order to immerse the device completely, we determined that we needed some forms of epoxy that was conductive and hopefully resistant to acid. We started with a sample of PolySolder LT silver epoxy. We tested in both HF and H_2SO_4, to ensure that it would withstand a MEMS release process and the subsequent use in H_2SO_4 intercalant.

Figure A-1 (a) presents a picture of a PolySolder LT sample before and (b) that same sample after immersion in H_2SO_4 for 10 minutes.

(a)   (b)
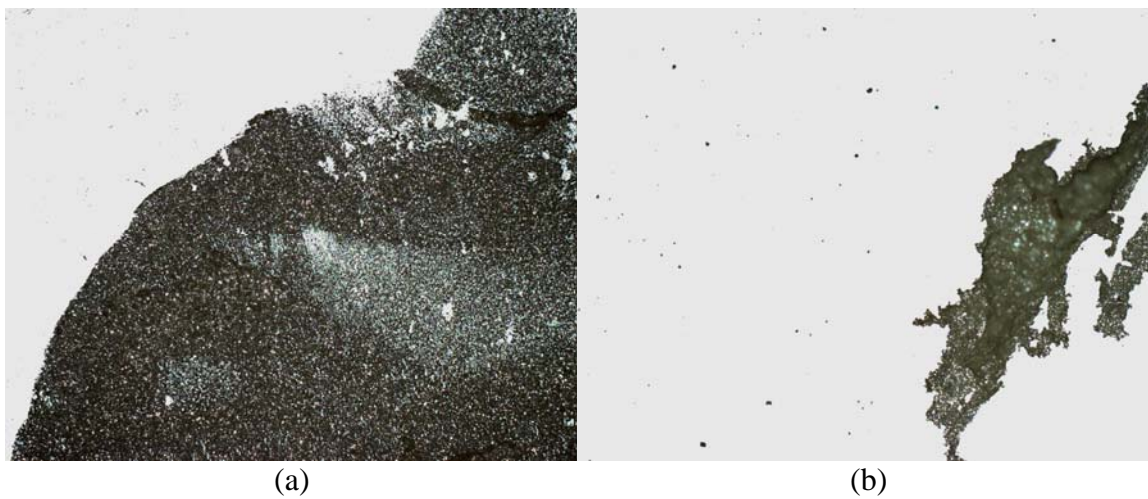
Figure A-1: PolySolder LT (a) as deposited and cured and (b) the same location after 10 min immersion in H_2SO_4.

Immediately we discovered that this was not going to work, thus we contacted AFRL/ML and they suggested using a sample of Epotek H-22 silver epoxy that they had success in mounting applications. Unfortunatley, neither the company or AFRL knew if it would stand up to H_2SO_4. We mounted using H-22, confident that this would be a better solution. When we added the H_2SO_4, we immediately noticed the acid turning brown, and within 10 minutes, the H-22 was completely dissolved. We then called Epotek and ordered their most resistant silver epoxy, H-27d. We tested this epoxy the same way as we had for PolySolder LT and achieved the results presented in Figure A-2. this epoxy withstood the 10 minute H_2SO_4 bath better than the other two epoxies, but did not resist completely, as is required to mechanically and electrically bond fibers in our research. The volumes tested were about 100 times the thickness and thousands of times the area that would be present on a die connecting P-100 fibers to PolyMUMPs[®] structures.

<center>(a)   (b)</center>
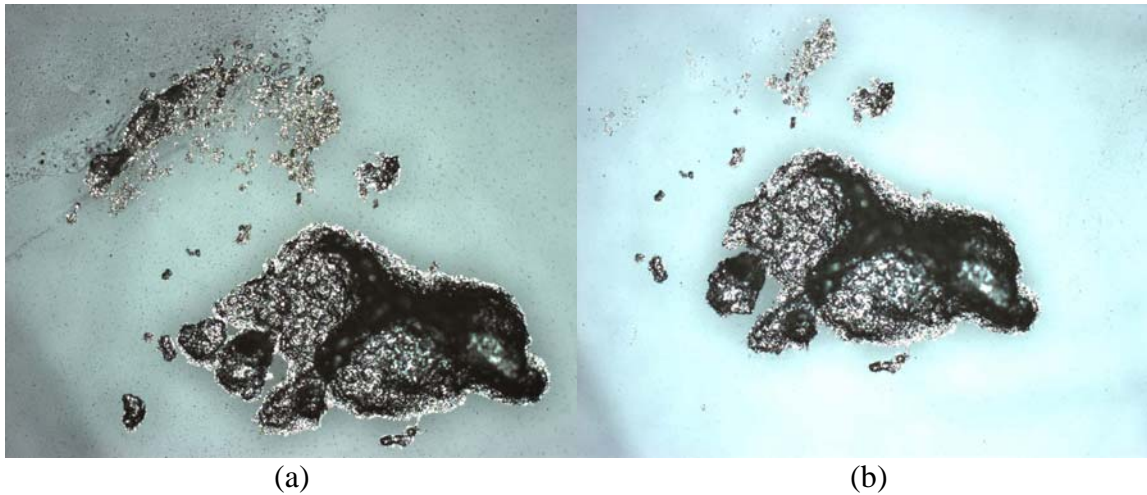
Figure A-2: Epotek H-27D silver epoxy (a) as deposited and cured and (b) the same location after 10 min immersion in H_2SO_4.

A.3   Paraffin Sealing

Once we discovered that the epoxy was unsuitable, we decided to see if we could cover the epoxy with paraffin, as Vogel had used to cover his colloidal silver in his early experiments. We determined the temperature at which paraffin melted freely was 57° C and it was solid at 50° C when it was not in contact with liquid paraffin. We mounted several carbon fibers onto a PolyMUMPs® die with H-27D silver epoxy. We then placed the die onto a heated stage, set to 53.9° C. We used a 3 μm diameter probe tip to transfer small droplets of wax from a liquid reservoir to the bonded fiber ends. We applied the paraffin to the bond pads to cover the epoxy. We then performed our normal HF release process, but only heated to 45° C for 60 minutes to prevent any reflow of paraffin. Unfortunately, even at this low temperature, at the interface of the paraffin and the MEMS die some of the paraffin liquefied, causing a poorer contact and allowing liquids still on the die to get under the edges of the paraffin. At this point, the addition of any liquids caused the paraffin to peel off and the graphite, silver epoxy, and fibers were no longer bonded together. Additionally, when used on carbon fibers mounted on the

<center>A-3</center>

MEMS die, the paraffin appeared to "wick" up the length of the fiber approximately 200 μm from the bond pad. This could have detrimental effects on the performance of the fiber during intercalation. This demonstrated a failure of our ability to protect the silver epoxy from the H_2SO_4 bath and the method was subsequently discarded.

A.4   Solder Powder

Since the silver epoxy was reacting with our intercalant, we decided to find a metallic solder that would react minimally with H_2SO_4. Tin etches in H_2SO_4, so we decided to find a small diameter solder sphere/powder that had the lowest content of tin. After further research, we found a solder powder that was composed of spheres from 15 μm to 25 μm in diameter. Amtech Incorporated produces several lines of solders in this size, including a 10% Sn/88% Pb/2% Ag compound that fit our requirements most closely. The solder had a liquidus temperature of 290° C and a solidus temperature of 268° C. We decided to test the usefulness of this material by applying it to a PolyMUMPs® die at temperatures from 265° C to 340° C on our Micromanipulator probe station's thermal chuck presented in Figure A-3, both using flux paste and without the flux.

Figure A-3: Thermal chuck for Micromanipulator probe station

Since the euctectic temperature of polysilicon/gold is 290° C, we tried to keep well below this temperature, but above the liquidus temperature of the solder and settled on 270° C. The surface tension of the solder was problematic in all of our attempts. We had to individually burst the spheres or smear them onto the PolyMUMPs® die to break them and allow them to adhere to the devices underneath. At times, we could get the solder powder to flow across the MEMS location on the PolyMUMPs® die, but within a few minutes, it would congeal and cause discoloration and damage, and not allow the addition of any more solder to the location. A still series of this phenomenon is presented in Figure A-4.

| (a) | (b) | (c) | (d) |
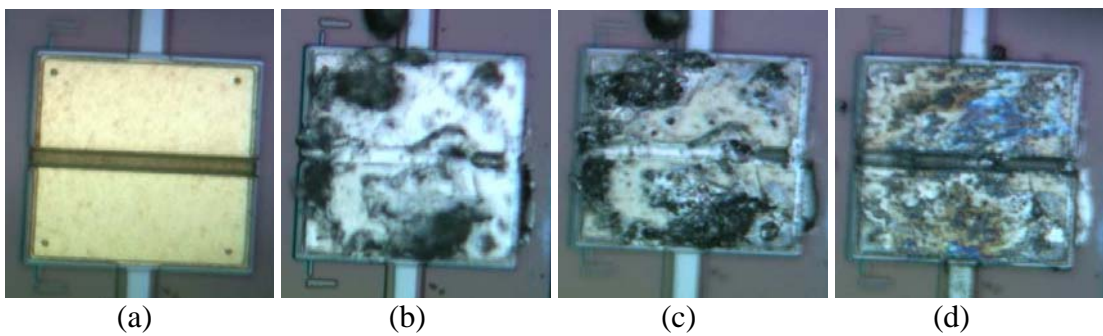
Figure A-4: 270° C solder powder test: (a) contact pad prior to addition to solder, (b) initial application of solder wicking to pad, (c) same pad 5 minutes after application pulling away from edges leaving gold exposed and (d) attempt to reapply solder resulting in removing previous solder and no new solder adhering to contact pad.

The results of this testing with solder powder in our applications caused us to discard the idea of using solder as an attachment mechanism, before even being able to test the solder with our intercalants.

APPENDIX B: APPENDIX B: SU-8 METAL LIFT-OFF PROCESS

B.1 SU-8/LOR-3A Liftoff Process

Step	Process	Time
Epoxy Bake	Bake on hotplate at 150 ºC	1 hour
Substrate Prep	Rinse with DIW, dry with N_2	
HF Etch	Remove PSG with 49% HF etch - note, only removing minimal amount to reach SiN, not fully releasing structure	10 seconds
Rinse and dry	Rinse with DIW, dry with N_2, Bake on hotplate at 150 ºC	5 minutes
LOR-3A		
Apply LOR-3A	Apply droplet of LOR-3A	
Spin Coat LOR-3A	Spin at 3,000 RPM for 45 seconds, 10,000 RPM Ramp	
Post Bake LOR-3A	Bake on hotplate at 150 ºC	5 minutes
SU8-5		
Apply SU8-5	Apply droplet(s) of SU8-5	
Spin Coat SU8-5	Spin at 3000 RPM – Ramp to 500 RPM @ 100 RPM/sec (5 sec) to spread. Accelerate at 300 RPM/sec to 3000 RPM, hold at final speed	30 seconds at final spin speed
Pre-Bake SU8-5	Two stage baking process. First stage: 65 ºC Second stage: 95 ºC (same hotplate) Turn back on 65 ºC Cool to room temperature	 1 minute 2 minutes Until plate 65º 10 minutes
Expose SU8-5	Expose 220 mJ/cm^2 NUV radiation @ 365 nm	25 seconds
Post Exposure Bake SU8-5	Two stage baking process. First stage: 65 ºC Second stage: 95 ºC (same hotplate) Turn back on 65 ºC Cool to room temperature	 1 minute 2 minutes Until plate 65º 10 minutes
Develop SU8-5	Immerse in SU8 developer	2 minutes
Rinse	Rinse in Isopropyl Alcohol and N_2 dry	
LOR-3A		
Etch	Place in LDD-26W developer	90 seconds
Metallization		
Ti	Place in e-beam evaporator	
	Follow procedure for evacuating chamber and preparation for metal deposition	

	Deposit 250 Å Ti	Per deposition system
Au	Deposit 250 Å Au	Per deposition system
	Remove sample from chamber once conditions set in deposition procedure are complete	
Metal Liftoff	20 min in 1165 stripper at 90° C	20 minutes
	Place metallized side of device onto the sticky side of Scotch™ tape and peel tape to remove metal remaining over photoresist	
Resist removal	Immerse in Acetone/spray with Acetone bottle until resist is completely removed	Varies
Rinse	Rinse with DIW and N_2 dry	

APPENDIX C: LCR METER SETUP AND OPERATING PROCEDURES

C.1   LCR Meter Setup

Figure C-1 shows the proper mounting of the glass slides used for the impedance test.
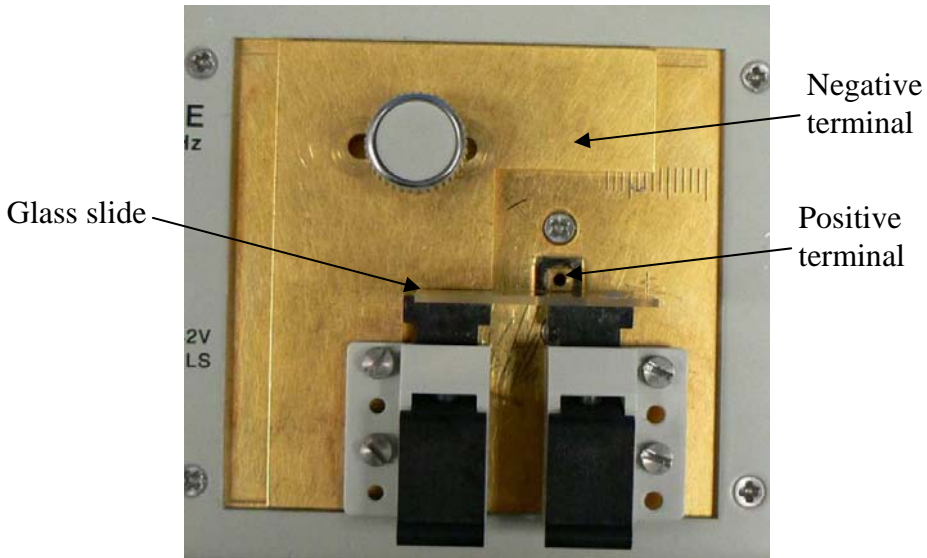
Figure C-1: Image of 16092A testing adapter with e-Beam evaporated gold slide with fiber attached. The gold on the glass slide faces the top of the picture when mounted correctly [53].
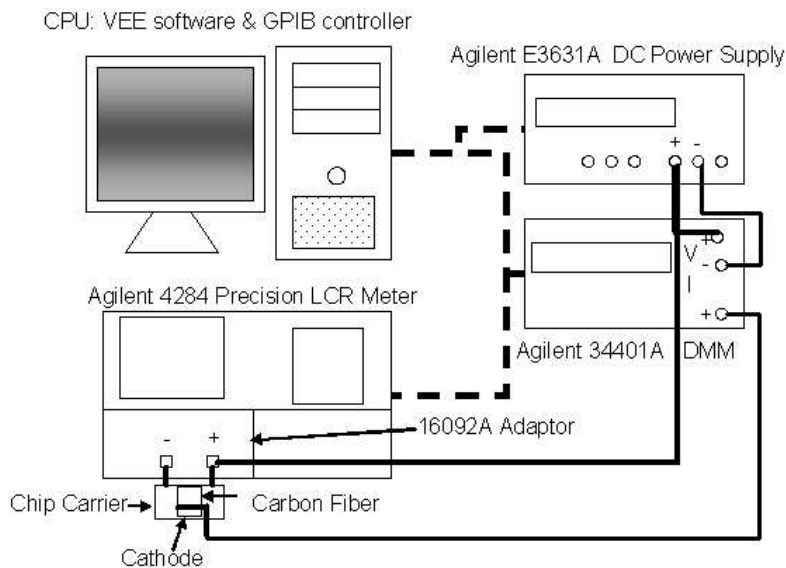
Figure C-2: Small signal frequency response test setup to measure inductance, capacitance, and resistance [53].
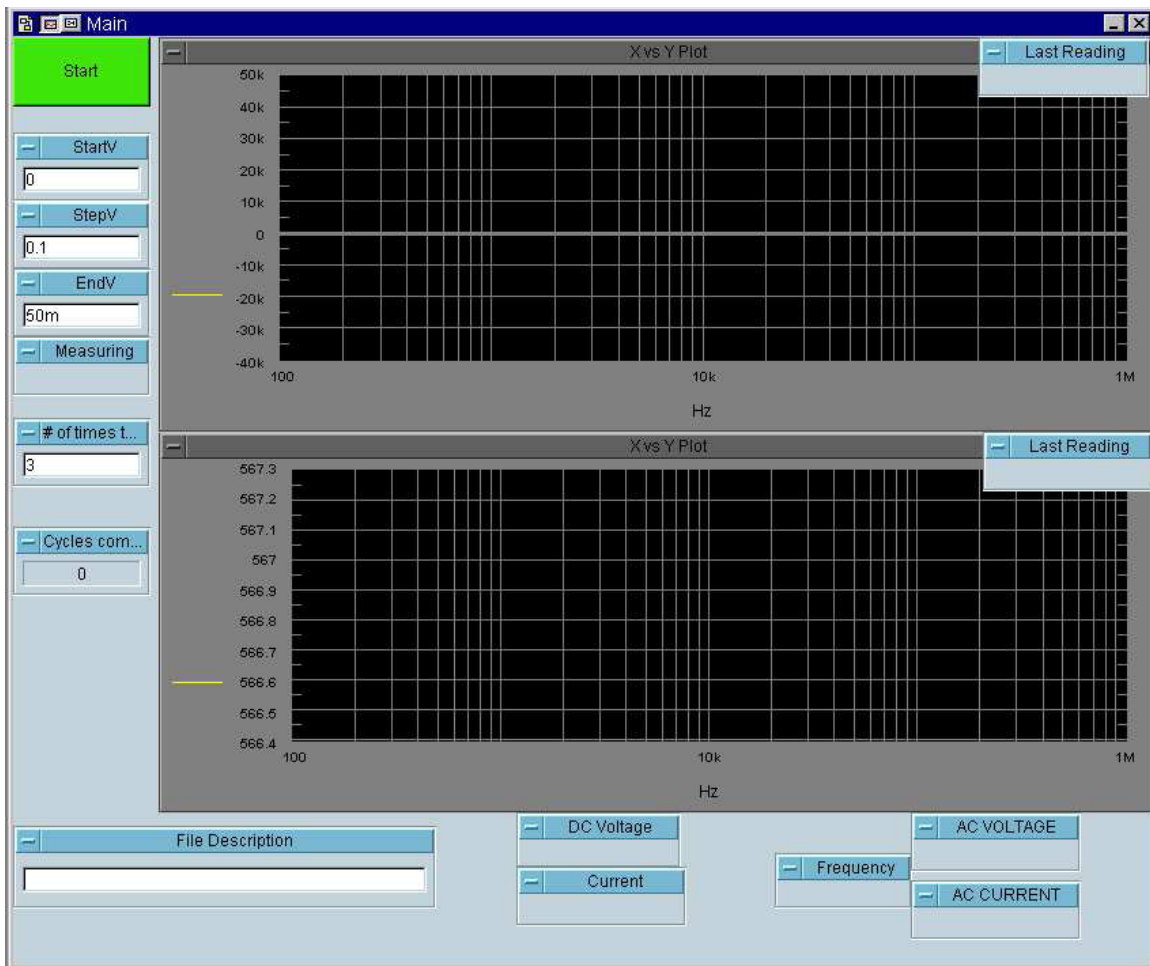
Figure C-3: User interface for VEE program to test small signal inductance, capacitance and resistance [53].

Table C-1: Frequencies used tested using FIBER_FREQ_Measurement.vee [53].

Frequency	
20 Hz	10 kHz
50 Hz	20 kHz
100 Hz	25 kHz
150 Hz	30 kHz
200 Hz	40 kHz
250 Hz	50 kHz
300 Hz	60 kHz
400 Hz	80 kHz
500 Hz	100 kHz
600 Hz	150 kHz
800 Hz	200 kHz
1 kHz	250 kHz
1.5 kHz	300 kHz

2 kHz	400 kHz
2.5 kHz	500 kHz
3 kHz	600 kHz
4 kHz	800 kHz
5 kHz	1 MHz
6 kHz	
8 kHz	

Table C-2: Operating procedures to perform small signal response testing during intercalation of carbon fibers using FIBER_FREQ_Measurement.vee [53].

Step	Procedure
1	Turn on Agilent 4284 Precision LCR Meter 30 minutes prior to use
2	Connect IEEE-488 cables to system as shown in Figure C-2 as a dashed line
3	Adjust position of 16092A adapter spring clips to hold sample
4	4 Perform OPEN, and SHORT correction procedures in the 4284 manual [54] note: OPEN and SHORT correction procedures need to be reaccomplished if the position of spring clips are changed
5	Connect sample to 4284 and complete electrical connections as shown in Figure C-1
6	Start Fiber Freq Measurement.vee
7	Enter the following components Intercalation starting voltage (StartV) Intercalation step voltage (StepV) Intercalation ending voltage (EndV) Number of times to run, usually 1 File description, becomes suggested file name (EndV)
8	Press Start
9	Confirm or change file name cycles completed will update after it completes a run
10	When complete replace sample and proceed from step 7

C.2   FIBER_FREQ_Measurement.vee data collected

The data collected by the FIBER_FREQ_Measurement.vee program collects ten pieces of information per frequency pass. "Cycles" identifies the number of times the program has run and counts from 0 to the number of cycles chosen prior to running the program. The measurement mode descriptor, "MSRMT," is next and can be ZTD, CSRS, CPRP, LSRS, and LPRP which stand for impedance and phase, series capacitance and

resistance, parallel capacitance and resistance, series inductance and resistance, and parallel inductance and resistance, respectively. The next two pieces of data relate to the intercalation voltage and current "DCVOL" and is the programmed intercalation voltage and "DC CURRENT" is the intercalation current as measured by the digital multimeter. "FREQUENCY" is the small signal frequency at which this data was collected. While "VAC" and "IAC" are the small signal voltage and current applied by the 4284 LCR meter for this frequency. "VARIABLE 1" and "VARIABLE 2" have different meanings depending on the measurement mode and are broken down in Table C-3. A sample table of collected data is located in table C-4 [53].

Table C-3: Variable description for data collected using
FIBER_FREQ_Measurement.vee [53]

MSRMT	VARIABLE 1	VARIABLE 2
ZTD	impedance (Ω)	phase (°)
CSRS	series capacitance (F)	series resistance (Ω)
LSRS	series inductance (H)	series resistance (Ω)
CPRP	parallel capacitance (F)	parallel resistance (Ω)
LPRP	parallel inductance (H)	parallel resistance (Ω)

Table C-4: Data collected when running FIBER_FREQ_Measurement.vee [53].

Cycles	MSRMT	DCVOL	DC CURRENT	FREQUENCY	VAC	IAC	VARIABLE1	VARIABLE2
1	ZTD	0	9.85E-009	20	0.887812	0.00113944	778.868	-0.013545
1	ZTD	0	-9.89E-009	50	0.886114	0.00113815	778.551	-0.015908
1	ZTD	0	9.89E-009	100	0.88959	0.00114166	778.551	0.00031674
1	ZTD	0	-3.21E-008	150	0.889653	0.0011427	777.087	0.008698
1	ZTD	0	2.96E-008	200	0.88653	0.00113995	778.769	-0.003377
1	ZTD	0	4.9E-009	250	0.887514	0.00113983	779.206	0.006675
1	ZTD	0	-3.45E-008	300	0.89013	0.00114276	779.064	-0.003901
1	ZTD	0	-1.48E-008	400	0.889037	0.0011412	779.939	-0.001191
1	ZTD	0	7.4E-009	500	0.887415	0.00113833	779.269	0.003917

REPORT DOCUMENTATION PAGE	*Form Approved* *OMB No. 074-0188*

The public reporting burden for this collection of information is estimated to average 1 hour per response, including the time for reviewing instructions, searching existing data sources, gathering and maintaining the data needed, and completing and reviewing the collection of information. Send comments regarding this burden estimate or any other aspect of the collection of information, including suggestions for reducing this burden to Department of Defense, Washington Headquarters Services, Directorate for Information Operations and Reports (0704-0188), 1215 Jefferson Davis Highway, Suite 1204, Arlington, VA 22202-4302. Respondents should be aware that notwithstanding any other provision of law, no person shall be subject to an penalty for failing to comply with a collection of information if it does not display a currently valid OMB control number.
PLEASE DO NOT RETURN YOUR FORM TO THE ABOVE ADDRESS.

1. REPORT DATE *(DD-MM-YYYY)* 12-2007	2. REPORT TYPE **Doctoral Dissertation**	3. DATES COVERED *(From – To)* Aug 2004 – Dec 2007

4. TITLE AND SUBTITLE	5a. CONTRACT NUMBER
Piezo-Electrochemical Transducer Effect (PECT)	5b. GRANT NUMBER
Intercalated Graphite Micro-Electromechanical Actuators	5c. PROGRAM ELEMENT NUMBER

6. AUTHOR(S)	5d. PROJECT NUMBER
Kading, Glen A., Major, USAF	5e. TASK NUMBER
	5f. WORK UNIT NUMBER

7. PERFORMING ORGANIZATION NAMES(S) AND ADDRESS(S) Air Force Institute of Technology Graduate School of Engineering and Management (AFIT/EN) 2950 Hobson Way WPAFB OH 45433-7765	8. PERFORMING ORGANIZATION REPORT NUMBER AFIT/DEE/ENG/08-03
9. SPONSORING/MONITORING AGENCY NAME(S) AND ADDRESS(ES) N/A	10. SPONSOR/MONITOR'S ACRONYM(S)
	11. SPONSOR/MONITOR'S REPORT NUMBER(S)

12. DISTRIBUTION/AVAILABILITY STATEMENT
APPROVED FOR PUBLIC RELEASE; DISTRIBUTION UNLIMITED.

13. SUPPLEMENTARY NOTES

14. ABSTRACT

The purpose of this research is to investigate the Piezo-Electrochemical Transducer (PECT) effect in intercalated graphite as a possible mechanism of actuation for micro-electromechanical systems (MEMS). This dissertation presents the results of research into the PECT effect in H_2SO_4-intercalated graphitized carbon fibers, including both electrical and mechanical characteristics of this effect.

PECT fibers achieve up to 1.7% strain at 1.4 V of applied potential. In contrast, the piezoelectric material polyvinylidene difluoride (PVDF) generates only 0.01% strain and polysilicon thermal expansion between 0.02 and 0.06% strain depending on the thermal conductivity of the particular polysilicon that the actuators are fabricated in. This work concludes that PECT carbon fiber actuators achieve two orders of magnitude better strain than PVDF piezoelectric actuators and polysilicon thermal expansion in the same voltage range of operation. In addition to this highly improved strain, the devices, after an initial peak power consumption of 227 µW, a PECT device uses only 260 nW to hold actuation. Although slow operation and unpractical intercalants are serious drawbacks to PECT actuators, the characteristics of strain and power consumption presented in this dissertation prove that PECT actuators, given some minor modifications, prove to be a competitive alternative to current MEMS actuators.

15. SUBJECT TERMS
Pyrolytic Graphite, Graphite Intercalation Compounds, Sulfuric Acid, Strain (Mechanics), Chemical Reactions

16. SECURITY CLASSIFICATION OF:			17. LIMITATION OF ABSTRACT	18. NUMBER OF PAGES	19a. NAME OF RESPONSIBLE PERSON LaVern A. Starman, Major, USAF (ENG)
REPORT U	**ABSTRACT** U	**c. THIS PAGE** U	UU	194	19b. TELEPHONE NUMBER *(Include area code)* (937) 255-6565, ext 4618; e-mail: Lavern.Starman@afit.edu

Standard Form 298 (Rev: 8-98)
Prescribed by ANSI Std. Z39-18